JYU DISSERTATIONS 198

Joshua Ben Hilton

Decays of New Nuclides ^{169}Au, ^{170}Hg, ^{165}Pt and the Ground State of ^{165}Ir Discovered Using MARA

UNIVERSITY OF JYVÄSKYLÄ
FACULTY OF MATHEMATICS
AND SCIENCE

JYU DISSERTATIONS 198

Joshua Ben Hilton

Decays of New Nuclides ^{169}Au, ^{170}Hg, ^{165}Pt and the Ground State of ^{165}Ir Discovered Using MARA

Esitetään Jyväskylän yliopiston matemaattis-luonnontieteellisen tiedekunnan suostumuksella julkisesti tarkastettavaksi yliopiston Ylistönrinteen salissa FYS1 maaliskuun 13. päivänä 2020 kello 12.

Academic dissertation to be publicly discussed, by permission of the Faculty of Mathematics and Science of the University of Jyväskylä, in Ylistönrinne, auditorium FYS1, on March 13, 2020 at 12 o'clock noon.

JYVÄSKYLÄN YLIOPISTO
UNIVERSITY OF JYVÄSKYLÄ

JYVÄSKYLÄ 2020

Editors
Timo Sajavaara
Department of Physics, University of Jyväskylä
Timo Hautala
Open Science Centre, University of Jyväskylä

Permanent link to this publication: http://urn.fi/URN:ISBN:978-951-39-8095-5

ISBN 978-951-39-8095-5 (PDF)
URN:ISBN:978-951-39-8095-5
ISSN 2489-9003

Decays of new nuclides ^{169}Au, ^{170}Hg, ^{165}Pt and the ground state of ^{165}Ir discovered using MARA

Thesis submitted in accordance with the requirements of the University of Jyväskylä for the degree of Doctor in Philosophy by

Joshua Ben Hilton

February 2020

Abstract

New nuclides ^{169}Au, ^{165}Pt and ^{170}Hg and new ground state ^{165}Ir^{g} were produced using reactions of ^{96}Ru(^{78}Kr,XpXn) at bombarding energies of 390 MeV and 418 MeV and ^{92}Mo(^{78}Kr,XpYn) at a bombarding energy of 418 MeV. The MARA vacuum mode recoil mass separator was used to separate the new nuclei and implant them into a DSSD instrumented with digital readout electronics to measure their decay properties. The proton-emitting nuclei were identified using digitised preamplifier output 'traces', and the method used is discussed in depth.

Fifteen proton-decay chains of ^{169}Au^{m} were measured with proton-emission energy $E_p = 2182(28)$ keV and half-life $T_{1/2} = 1.27^{+0.61}_{-0.57}$ µs. One α-decay chain of ^{169}Au^{m} was also identified with α-particle energy $E_\alpha = 7333(27)$ keV, which occurred 1.3 µs after the recoil ion was implanted. Combining the data for both decay branches yielded a half-life of $1.16^{+0.50}_{-0.47}$ µs and an estimated production cross section of 5 nb for this state in ^{169}Au.

Seven proton-decay chains of ^{165}Ir^{g} were measured with proton emission energy $E_p = 1454(38)$ keV and $T_{1/2} = 1.20^{+0.82}_{-0.74}$ µs.

The results are compared with Wentzel–Kramers–Brillouin (WKB) calculations.The prospects of observing proton emission from even lighter gold and iridium isotopes are discussed.

Four α-decay chains of ^{165}Pt were measured with α-particle energy $E_\alpha = 7272(14)$ keV and $T_{1/2} = 0.26^{+0.26}_{-0.09}$ ms, with an assumed α branching ratio of ≈100%.

One α-decay chain of ^{170}Hg was measured with $E_\alpha = 7590(30)$ keV and $T_{1/2} = 0.08^{+0.40}_{-0.04}$ ms, with an assumed α branching ratio of ≈100%. Reduced α-decay widths were compared with systematic data in the region, indicating that both α decays are unhindered. Combining the α-decay Q values measured with extrapolated masses indicates that the new nuclides are both unbound to 2-proton emission by >1 MeV. However, this decay mode does not compete as their α-decay half-lives are too short. Improved data were obtained for the α emitters ^{166,167}Pt, produced via the ^{96}Ru(^{78}Kr,α4n) and ^{96}Ru(^{78}Kr,α3n) reactions at bombarding energies of 390 MeV and 418 MeV, respectively.

The results of this thesis are presented in 2 refereed publications [1, 2].

Acknowledgements

I would like to thank, first and foremost, my full supervisory team, Prof. Robert Page, Prof. Juha Uusitalo, Prof. David Joss and Dr. Jan Sarén. You have all be instrumental in my success, and without each of you I could not have become the physicist I am today. The time you have taken to teach me is appreciated immensely, and there have been lessons taught I will carry with me forever.

I would like to thank the groups in both Liverpool and Jyväskylä, without whom what we do would not be possible. Nuclear spectroscopy is seldom a solitary endeavour, and it takes all of us working together to pull apart the fabric that covers the edge of what we know. So many people who have been part of my physics world have been helpful to bounce ideas with, show me the stupid thing I was missing and remind me the world is bigger than physics. The many hours, both in Liverpool and Jyväskylä, spent playing games and relaxing have kept me sane (mostly). To all my friends from along the way, thank you.

Finally, all my love to my fiancée Jess. I don't know how you didn't murder me, I would have done.

"It is called 'Force' in your tongue. But as you push the world, so does the world push back. Think of the way force may be applied effortlessly. Imagine but a whisper pushing aside all in its path. That is 'Fus.' Let its meaning fill you. Su'um ahrk morah. You will push the world harder than it pushes back." - Paarthurnax, Skyrim

Contents

Chapter 1

Introduction

Atomic nuclei account for more than 99% of all baryonic matter. The many-body nature of the interactions between strongly interacting protons and neutrons render it difficult to predict the observable properties of heavy nuclei from a basic nucleon-nucleon interaction. A comprehensive description of the nucleus would not only be of intrinsic interest for nuclear physics, but could also benefit other fields where many-body systems are common. While the nuclear potential that arises from the complicated interactions between nucleons is hard to calculate ab initio, models can be constrained experimentally by measuring eigenstates of the nuclear wave function. For heavy neutron-deficient nuclei, measurements of proton emission energies and half-lives can help to assign the binding and orbital angular momentum of the emitting states. This in turn allows the location and properties of single-particle states to be determined, which contribute to a map of states used to constrain the nuclear potential over a broad mass surface.

Attempting to measure exotic proton drip line nuclei presents many challenges. The often extremely small production cross sections of the lightest isotopes of heavy elements make it essential to use selective and efficient techniques. Short half-lives which greatly decrease close to the proton drip line [3] present the largest challenge. Such nuclei are therefore often studied by combining an in-flight separator with a fast, efficient decay spectrometer capable of resolving the α-particle and proton energies of different reaction products. The energy and half-life of α and proton decays are useful quantities to measure, greatly assisting with assignments of nuclear binding and spin of emitting states. They can also be used to calculate other useful quantities such as reduced decay widths and decay Q-values, which allow systematic comparison with other nuclei in the same region. Analysis of these overarching trends across different masses of different elements allows us great insight into how the nucleus is bound and how shell structure affects the nucleus far from stability. If short-lived nuclei can be separated and studied at a focal plane with the prerequisite equipment in $\sim$500 nanoseconds, decay spectroscopy is often possible for nuclei with microsecond lifetimes.

When searching for a new nuclide, it is important to consider the quantity it is possible to produce in a reasonable time frame. Once produced, their half-lives relative to the sensitive time of the equipment and the flight time through a separator

determines whether they can be observed. These factors determine which of the several separators that are available globally will be used in any given experiment. This work focuses on two experiments that were conducted using the MARA vacuum-mode mass separator at the University of Jyväskylä, Finland, which is one of a small number of recoil mass separators in operation at a suitable facility. The focal-plane detectors are fully instrumented with digital electronics, which is critical for this experiment.

Figure 1.1 shows the area of the proton drip line this work focused on near the N = 82 shell closure. The objectives were to produce ^{170}Hg and ^{169}Au in the 4n channel and 1p4n channel, respectively from compound nucleus ^{174}Hg* and ^{165}Pt and ^{165}Ir would be produced in the 5n channel and 1p4n channel, respectively from compound nucleus ^{170}Pt*. The half-lives and production cross sections systematics in the region indicate whether the production of these nuclei is feasible. Figure 1.2 shows how the half-lives of the elements in this region vary with neutron number. The general trend on this logarithmic scale of half-life increasing monotonically with neutron number occurs because α decays connect states of the same spin and parity J^π, meaning Q_α increases monotonically with neutron number for the nuclei shown. The trend for Re is non-linear as proton decay gradually becomes the dominant decay mode with decreasing neutron number. Iridium sees a similar effect, but with an odd-even staggering in Q_p making it less smooth, with the staggering seen in gold being more complex still.

A simple forecast of the lines shown in Figure 1.2 would suggest that the half-life of the next lightest isotope for each element would be between 1-100 μs. Proton or α decays slower than 5 μs can be resolved with the MARA mass separator in the conventional way, and any decay time between 600 ns (the flight time through MARA) and 5 μs (the nominal preamplifier trace length) can be resolved with traces. Even nuclides with a half-lives $\leq$600 ns can be seen with traces, although most decays would occur during the flight through MARA.

A similar forecast can be performed with Figure 1.3, which shows the cross sections of production for the lightest isotopes of Ir, Pt, Au and Hg. A trend of decreasing cross section with decreasing neutron number shows that more exotic nuclides have increasingly lower production cross sections [17]. With the exception of ^{169}Au, the next lightest isotope for each element would likely have a production cross section of $\leq$1 nb. This is not necessarily too low, as several factors can enhance production. Production probability can be maximised by optimising beam energy and production channel through target and beam choice. A cross section of 1 nb would usually require $\sim$5 days of beam time to produce a single atom of mass 120$\leq$A$\leq$190, assuming average values of beam intensity (2 pnA), target thickness (0.2 mg/cm^2), transmission efficiency ($\sim$40%) and particle detection efficiency ($\sim$70%). It is not uncommon, however, to run 2 week long experiments searching for a single nuclide. The hardest new nuclide to produce if one considers only Figure 1.3 would be ^{170}Hg, which will probably have a cross section below 1 nb. The easiest new nuclide to produce would likely be ^{169}Au, which could have a cross section over 10 nb. New isotopes of platinum and iridium will

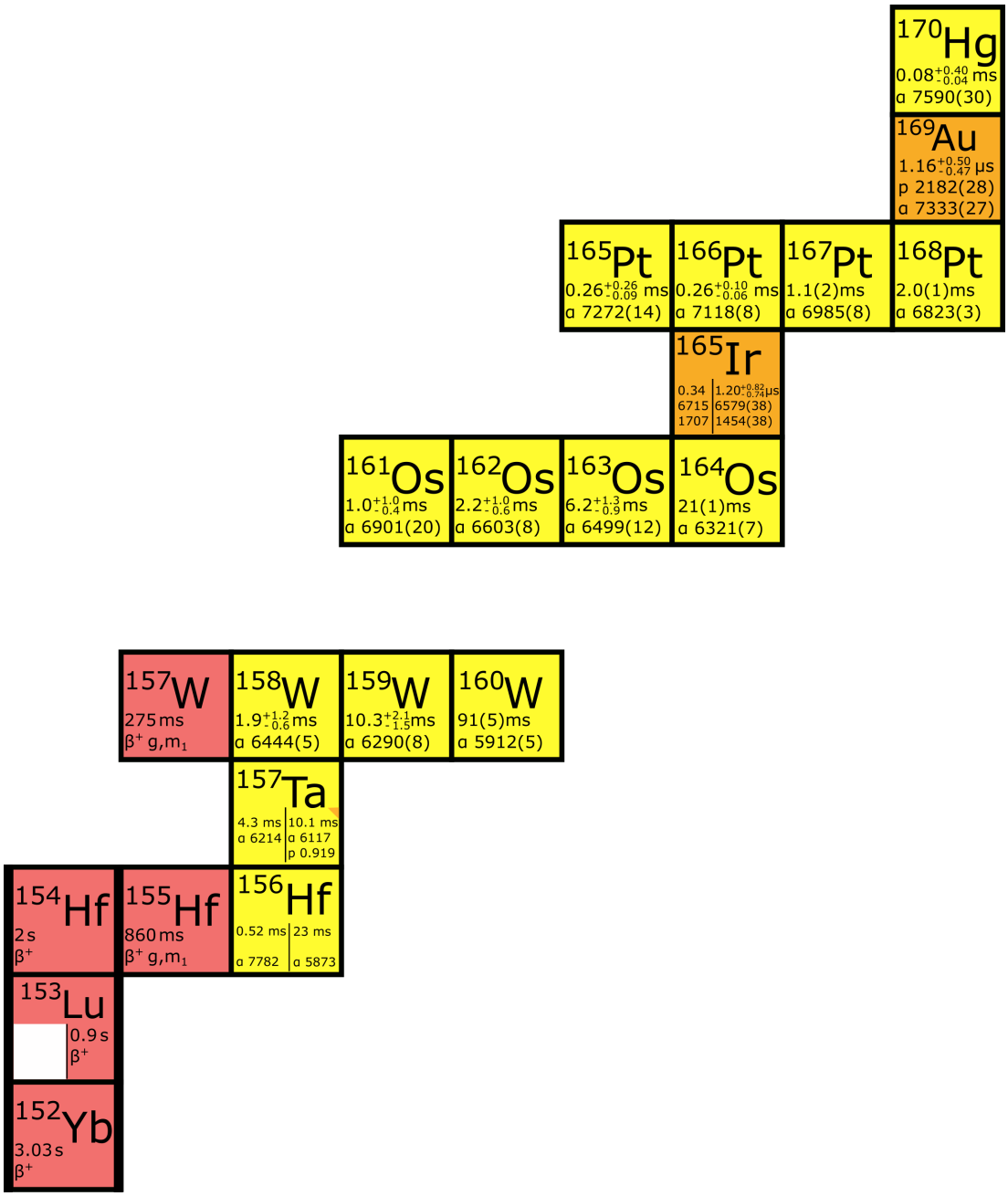

Figure 1.1: All nuclides measured in this work and their respective decay chains, terminating in all cases with a β^+ decay which was not detected. Data for nuclides not measured in this work taken from [4, 5, 6]. Some nuclei have been omitted to show the chains of interest to this work more clearly.

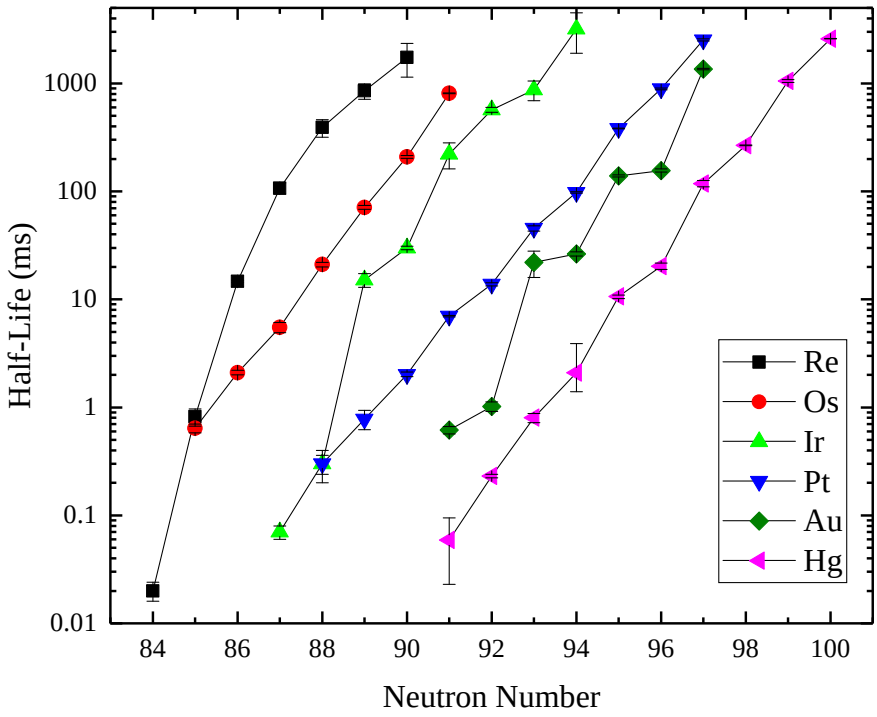

Figure 1.2: The half-lives in the region of the chart of nuclides relevant to this thesis. If a nuclide has more than one state that decays by particle emission, the value for the state with the longer half-life is plotted. All values were taken from NNDC at time of publication [7], and as such are a weighted average of all reported values. New values from this work are not included.

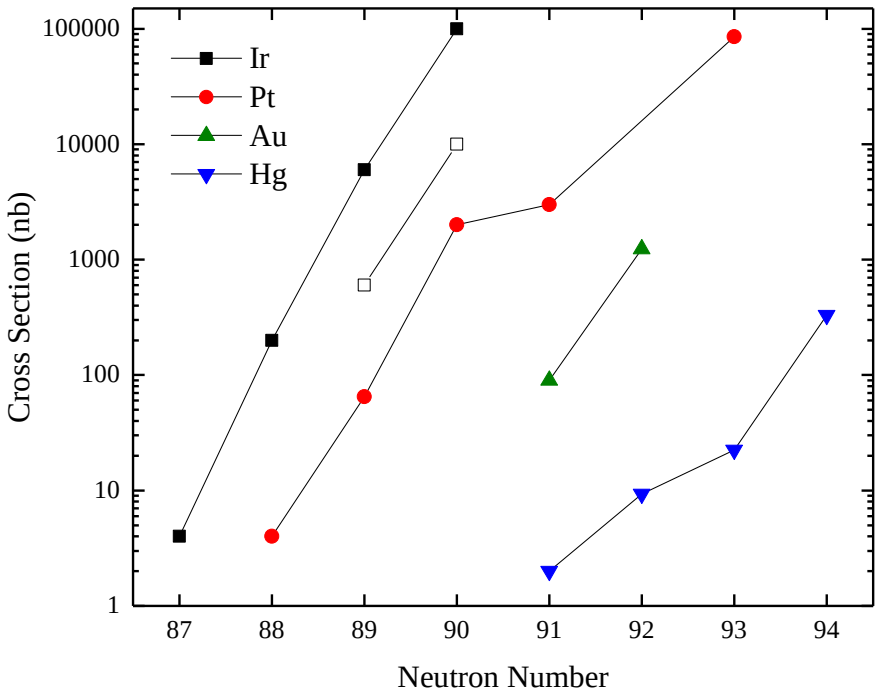

Figure 1.3: Cross sections of production in the region of the chart of nuclides relevant to this thesis. Open symbols denote the ground state of a nucleus in the case of iridium. The values for gold represent the combined cross section of both the ground and isomeric states. The values plotted for ^{171}Au and ^{172,173}Hg have been averaged from available data. Nuclides are produced in a variety of reactions detailed in source material, using the optimum beam and target combination at the best known optimum beam energies. [8, 5, 4, 9, 10, 11, 12, 13, 14, 15, 16]

be challenging to produce, with likely cross sections around 1 nb.

The reactions used in this work were ^{92}Mo(^{78}Kr,5n) at a bombarding energy of 418 MeV and ^{96}Ru(^{78}Kr,4n) at bombarding energies of 418 MeV and 390 MeV, respectively. Other 4 and 5 particle evaporation channels were also measured. The specific details of the two experiments are covered in section 3.2. The aim was to measure the lightest isotopes of Pt, Ir, Au and Hg, specifically the observation of the new nuclides ^{165}Pt, ^{169}Au, ^{170}Hg and new ground state ^{165}Ir^{g}. Both ^{165}Pt and ^{170}Hg are predicted to decay via α decay, and should be observable with conventional correlation analysis. Both ^{165}Ir^{g} and ^{169}Au^{m} are predicted to decay via proton-emission, and are likely to be too fast for conventional techniques. They should be observable in preamplifier traces of the energy signal generated when the nuclide is implanted in a silicon detector. These techniques are covered in more detail later in Sections 3.6.2 and 3.6.1.

Chapter 2

Theoretical Concepts

This section will provide the theoretical foundation necessary for understanding this thesis. The underpinning theory of radioactive decay is briefly summarised. Finally, the methodologies used to calculate the values and their uncertainties in this work are described.

2.1 Nuclear Models

The atomic nucleus is the dense core of an atom, which consists of protons and neutrons. A nucleus will have a mass lower than the sum of its constituent parts, because there is potential energy holding it together referred to as binding energy. The binding energy can be calculated by taking the mass difference between the nucleus itself and the sum of its parts

$$B(Z,A) = \left(Z \cdot M_H + (A-Z) \cdot M_n - M_{atom}\right) c^2, \tag{2.1}$$

where M_{atom} is the mass of the atom, M_H is the mass of a hydrogen atom and M_n is the mass of a neutron. If binding energy per nucleon is plotted against mass number, the result is known as the binding energy curve and illustrates the energy positive division between fusion and fission.

When removing nucleons from the nucleus, the binding energy difference between the initial and final states is called the separation energy. The neutron S_n and proton S_p separation energy can be written both in terms of binding energy difference and mass difference,

$$S_n = B({}^{A}_{Z}X_N) - B({}^{\mathrm{A-1}}_{\mathrm{Z}}\mathrm{X}_{N-1}) = \left(m({}^{\mathrm{A-1}}_{\mathrm{Z}}\mathrm{X}_N - 1) - m({}^{A}_{Z}X_N) + m_N\right) c^2, \tag{2.2}$$

$$S_p = B({}^{A}_{Z}X_N) - B({}^{\mathrm{A-1}}_{\mathrm{Z-1}}\mathrm{X}_N) = \left(m({}^{\mathrm{A-1}}_{\mathrm{Z-1}}\mathrm{X}_N) - m({}^{A}_{Z}X_N) + m({}^{1}H)\right) c^2. \tag{2.3}$$

Similar to ionisation energies in atomic physics, these separation energies reveal information about the strength of binding for the outermost valence nucleons. The points where exotic nuclei far from their stable isotopes become unbound to single particle emission are called the drip lines. At the proton dripline, the binding energy of

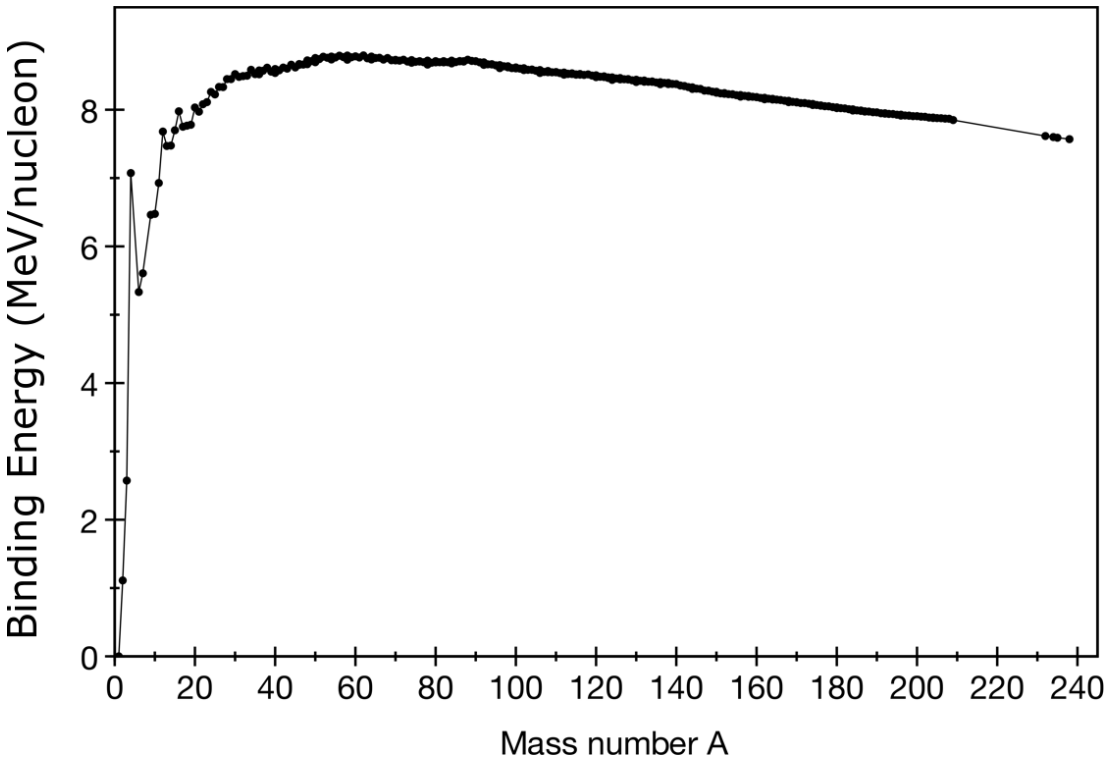

Figure 2.1: The binding energy per nucleon plotted as a function of mass number A. The nuclide with the lowest average mass per nucleon is ^{56}Fe and the nuclide with the highest binding energy per nucleon, i.e. the most tightly bound, is ^{62}Ni [18].

the outermost proton $S_p \leq 0$, making it an interesting area to study. Nuclides in this region exhibit rare and unusual behaviours such as proton emission, an inherently rare process that occurs in $< 1\%$ of nuclei. There are many combinations of valence neutrons and protons in this region not found near stability, and certain neutron orbitals can have lower energies in this extreme region. As they shift, so do other shell orbitals nearby, creating energy differences as occupations of the orbitals change. This occurs due to low numbers of neutrons in the outer shell of a nucleus, making this behaviour unique to the proton drip line. If a shell model formula can predict this energy level shifting then it is more likely to remain robust when forecasting what happens at the neutron drip line.

Another reason to study nuclei at the proton drip line is that determination of quantum properties such as spin, parity and binding energy is a routine task in this region. Proton and α-decay are both excellent ways to discover these properties, with no viable alternatives existing until closer to stability. Measuring stable nuclei is relatively trivial, but the difficulty of determining quantum numbers increases with distance from stability until these exotic decay modes become available.

2.1.1 Binding Energy

When trying to understand the shape of the binding energy curve, some interesting observations can be made. The binding energy of all but the lightest nuclides is $\approx 8\,\text{MeV/nucleon}$ within $\pm 10\%$. The second observation, as mentioned above, is that there are two distinct areas of the curve, the light side of iron where fusion is energy positive and the heavy side of iron where it gives way to fission. Some of the first efforts to explain this behaviour with a basic model were made by Weizsäcker in 1935 [19]. The core of the nucleus was described as a liquid drop, with its binding energy defined using the semi-empirical mass formula,

$$B(Z,A) = a_V A - a_s A^{2/3} - a_C Z(Z-1)A^{-1/3} - a_{sym}\frac{(A-2Z)^2}{A} + \delta(A,Z). \qquad (2.4)$$

These terms are all individually motivated and each of the constants is defined by a semi-empirical experimental fit. The volume term a_V represents the ≈ 8 MeV/nucleon flat linear relationship between binding energy and mass. It implies that each nucleon experiences the same potential as every other nucleon and has an identical number of neighbours.

Particles at the surface of the nucleus do not have this same number of neighbours and so the first subtraction comes from the a_s surface term. Since the surface area of the nucleus is proportional to R^2 and $R \propto A^{1/3}$ it follows that for a_s, $B(A,Z) \propto A^{2/3}$.

The Coulomb term a_C accounts for the positively charged protons that repel one another and reduce the binding energy of the nucleus as a whole. Unlike in the volume term, every proton repels every other proton equally, so a_C scales with $Z(Z-1)$. In

principle, this term can be calculated exactly with

$$\frac{3}{5}\frac{e^2}{4\pi\epsilon_0 r_0}\frac{Z(Z-1)}{A^{1/3}}, \tag{2.5}$$

where r_0 can be taken as 1.2 fm to give a value $a_C = 0.72\,\text{MeV}$. It is usually left as the constant a_C so it can be adjusted for different values of r_0.

The stability of nuclei is tied to the $N = Z$ line, and the symmetry term a_{sym} is introduced to represent that nuclei with extreme proton and neutron configurations relative to their stable isotopes are less stable. This term is particularly important in lighter nuclei where the stability adheres to the $N = Z$ line more closely (in heavier nuclei the Coulomb term quickly dominates). It reflects the ratio between protons and neutrons, taking the form of $\frac{(A-2Z)^2}{A}$.

The pairing term δ accounts for nucleons forming pairs with others of their species, giving rise to local stability peaks and troughs relative to other nuclei in the same region.

The binding energy formula and the liquid drop model comprise an effective simple model of the nucleus. However, the liquid drop model breaks down for nuclei in which we must consider quantum mechanical effects, the most obvious of which are the deviations see at $N, Z = 2,\ 8,\ 20,\ 28,\ 50,\ 82,\ 126$[1]. The increased binding energy at these numbers is what has led to them being referred to as magic numbers and to understand them we must first consider the shell like behaviour of nuclei.

2.1.2 Shell Model

In atomic physics, the shell model has already helped to clarify many of the experimental observations that have been made. The idea that electrons fill shells and sub-shells, in order of increasing energy in keeping with the Pauli principle, also makes physical sense. The electrons can have non-overlapping physical orbits around an externally provided potential. When nuclear physicists applied this same logic to the nucleus it yielded a lot of promising results, such as nucleons filling sub-shells and dramatic changes to measured properties when sub-shells are full. If one plots the difference between measured S_p or S_n values and their semi-empirical mass formula predictions against proton or neutron number [21], the discontinuities in the graph seen at the same proton and neutron numbers indicate the complete filling of a major shell. These are the aforementioned magic numbers; when a major shell is completely full, the relative binding of a nucleus is increased.

However, several incongruities in the nuclear shell model exist compared with its atomic counterpart. The potential that creates the shells in a nucleus is not external, but produced by the nucleons themselves all interacting with one another. It is no longer sensible to think of them as having non-overlapping orbits, as the size of a

[1] The magic number 126 is still subject to debate for protons, where it is thought to be between 114 and 130 [20].

nucleon relative to the size of the nucleus is not comparable with the electron-atom equivalent. To overcome these problems, the fundamental assumption of the shell model is necessary: the motion of one individual nucleon is governed by the potential created from all the other nucleons around it. Calculating this potential exactly is a non-trivial process, so instead it is assumed that each nucleon experiences the same effect and the potential is reduced to a two body problem.

When addressing the lack of collision free orbits, the Pauli exclusion principle must be considered. If two nucleons at the bottom of a potential well collide, it is unlikely that either one of them will gain enough energy to be promoted to the valence band at the top of the shell structure. Since every level between them and the valence band is full and cannot accept another nucleon, the collision is forbidden and does not happen. In this way, the nucleons can orbit one another as they appear to be 'transparent' [22].

The potential created by the nucleons interacting with and moving independently of one another can be described by a Woods-Saxon (W.S.) potential defined as,

$$V_{W.S.}(r) = \frac{-V_0}{1 + e^{(r\,-\,R/a)}}, \tag{2.6}$$

where a is the diffuseness parameter, (typically $a \approx 0.5$ fm), r is the distance from the nuclear centre, V_0 represents the depth of the potential well and has units of energy (typically $V_0 \approx 50$ MeV) and R is the mean nuclear radius, defined by $R = 1.25 \cdot A^{1/3}$ fm. This potential fulfils many of the necessary requirements; it is monotonically increasing with distance, nucleons at the surface of the nucleus experience the largest force, $V \to 0$ as $r \to \infty$ and for heavy nuclei, it resembles the density distribution of the nucleus. It cannot be solved using the Schrödinger equation analytically but it can be solved numerically in three dimensions to obtain the energy levels in Figure 2.2b. The levels are labelled with spectroscopic notation $(s, p, d, f, g, h, i...)$ to denote different values of l $(0, 1, 2, 3, 4, 5, 6)$. An important difference in spectroscopic notation is observed here; the index n is now the number of levels with the same l value as opposed to the principal quantum number. The degeneracy of each level, or the number of nucleons each level can hold, is the same as in atomic physics $(2(2l+1))$, with the $(2l+1)$ arising from the splitting due to m_l, the magnetic quantum number, and the prefactor of 2 comes from the splitting due to m_s, the spin quantum number. Neutrons and protons are counted as non-identical particles and as such a $1s$ level can hold two neutrons and two protons simultaneously.

Despite the shortcomings of the Woods-Saxon potential, it reproduces some of the magic numbers observed experimentally, but above $N, Z = 20$ the models both deviate from what is observed. In order to adjust the Woods-Saxon potential, fine adjustment is needed that does not break the physical meaning already present. Many unsuccessful attempts to add small terms to the existing formula took place in the 1940s until two teams came across the correction needed independently of one another simultaneously [24, 23]. By including a spin-orbit potential coupled to the Woods-Saxon potential, the

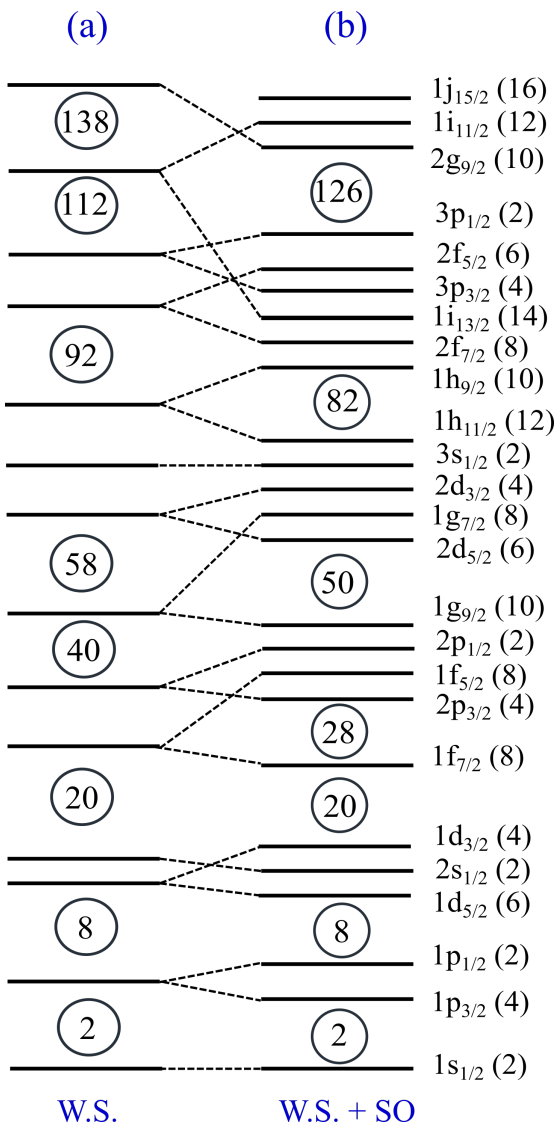

Figure 2.2: The energy levels of single-particle orbitals calculated from two different nuclear potentials by numerically solving the three-dimensional Schrödinger equation. The potentials are: (a) Woods-Saxon potential and (b) Woods-Saxon potential with Spin-Orbit coupling. Figure adapted from [23, 24].

magic numbers could be reproduced, as shown in Figure 2.2b (even predicting a new magic number at $N, Z = 184$, which has yet to be observed). This idea is borrowed from atomic physics, where the spin-orbit coupling comes from the interaction of the electrons magnetic moment with the magnetic field generated by its orbit around the nucleus, causing fine structure of spectral lines. The potential has the form $-V_{SO}(r)\mathbf{l}\cdot\mathbf{s}$, where $\mathbf{s}$ is the spin angular momentum and $\mathbf{l}$ is orbital angular momentum. These two quantities, like their atomic physics counterparts, can be added to give total angular momentum, $\mathbf{j} = \mathbf{l} + \mathbf{s}$. The spin on an individual nucleon $\mathbf{s} = \pm\frac{1}{2}$, so the values of $\mathbf{j}$ follow the form of $\mathbf{j} = \mathbf{l} \pm \frac{1}{2}$, with the exception of $\mathbf{l} = 0$ where only $\mathbf{j} = \frac{1}{2}$ is allowed. We can evaluate the expectation value of $\langle \mathbf{l}\cdot\mathbf{s}\rangle$ with:

$$\langle \mathbf{l}\cdot\mathbf{s}\rangle = \frac{1}{2}\left[\mathbf{j}(\mathbf{j}+1) - \mathbf{l}(\mathbf{l}+1) - \mathbf{s}(\mathbf{s}+1)\right]\hbar^2 \tag{2.7}$$

$$\langle \mathbf{l}\cdot\mathbf{s}\rangle = \begin{array}{cc} \frac{1}{2}\mathbf{l}\hbar^2 & \mathbf{j} = \mathbf{l} + \frac{1}{2} \\ -\frac{1}{2}(\mathbf{l}+1)\hbar^2 & \mathbf{j} = \mathbf{l} - \frac{1}{2} \end{array}$$

There are now $(2\mathbf{j}+1)$ levels in each $\mathbf{j}$-orbital, coming from new magnetic substate value m_j (m_s and m_l are no longer 'good' quantum numbers in this coupled system). There is further degeneracy involved when one considers that the shell model is based on a spherical nucleus, which is not always true. The nuclei studied in this work, however, are all roughly spherical and so the deformed shell model will not be covered.

2.1.3 Valence Nucleons

In an even-Z, even-N nucleus, the tendency of nucleons to be pairwise and couple to 0^+ pairs means the ground state spin (here and from now on, spin will mean total angular momentum I) and parity will be 0^+. For odd-A, the shell model successfully predicts and explains the spins and parities (calculated $\pi = (-1)^l$) of nearly all nuclei. It does this based on the 'independent particle model', which means it treats the last unpaired nucleon as the sole source of all the nuclear properties. This vast oversimplification means a natural extension to the shell model is to consider that all nucleons that are not part of a closed shell contribute to the nuclear properties. These nucleons are considered 'valence nucleons', which are important when considering the probability of a radioactive decay taking place, especially α decay. If an unpaired neutron or proton is part of a group of valence nucleons, the separation energy is not the same as when it is the last neutron or proton above a closed shell [21]. Similarly, α-decay is more probable if there are two protons and two neutrons in the valence shell, even though the extreme independent shell model would consider neither pair as valence.

2.2 Radioactive decay

Radioactive decay is the process by which an unstable nucleus spontaneously releases energy, usually in the form of electrons, positrons or electron capture (β-decay), protons (p emission), neutrons (n emission, fission) or protons and neutrons together (α decay, fission). There are a set of conservation laws which govern which decay type can happen at any given time, as mass-energy and angular momentum, at least on the scale of typical atomic nuclei, are conserved.

The fundamental underpinning of radioactive decay theory is that the probability of any radioactive decay occurring is constant and independent of the atoms age. The wide variation in start and end conditions, i.e. emission from different nuclei, allows for a varied landscape of decays. Most decay types (not β^-) have two main properties: an energy and a half-life. The energy of a decay is simply the difference between the mass of the emitting nuclide, the mother, and the sum of the masses of the decay products (the daughter nuclide and any decay particles). This emission energy is referred to as the reaction Q-value, and is the mass energy lost by the mother nuclide as it moves towards stability.

The half-life $T_{\frac{1}{2}}$ is the average amount of time it would take for half of a sample of a radionuclide to decay to its daughter product. Half-life is related to other relevant quantities by simple relations such that

$$T_{\frac{1}{2}} = \frac{\ln(2)}{\lambda} = \ln(2) \cdot \tau, \tag{2.8}$$

where λ is the disintegration or decay constant and τ is the mean lifetime of the decaying species. Similarly, $\lambda = \frac{1}{\tau}$, meaning a nucleus is likely to survive for the inverse of its decay constant. Both of these quantities can be used to describe the decay of a sample such that

$$N(t) = N_0 e^{-\frac{t}{\tau}} = N_0 e^{-\lambda t}, \tag{2.9}$$

where N_0 is the original number of mother nuclide atoms at time $t = 0$ and N is the number of atoms remaining at time t. Measuring the number of atoms in a sample is not practical, so often samples are defined by their activity A, i.e. the rate at which atoms are decaying $\frac{dN}{dt}$. Usually measured in Bq (units of s^{-1}), activity can be defined by

$$\frac{dN}{dt} = A(t) = \lambda N(t) = A_0 e^{-\lambda t}. \tag{2.10}$$

This would define the initial activity of the sample $A_0 = \lambda N_0$. This equation does not account for the fact that some nuclear decays result in other radioactive species, which also decay with different half-lives. As such, this can be considered as the single channel activity; the activity arising solely from the original nuclide.

Some nuclides have multiple concurrent decay paths open to them, each having a probability of occurring at time t relative to other paths defined by the branching ratio

BR. The partial decay constants of the two (or more) branches are defined as

$$t_{1/2}^{Branch} = \frac{t_{1/2}^{Total}}{BR} = \frac{1}{\lambda^{Branch}} = \frac{N}{-\left(dN/dt\right)^{Branch}}. \tag{2.11}$$

The total half-life $t_{1/2}^{Total}$ is found by summing together all the partial half-lives, and $0 \leq BR \leq 1$.

$$\frac{1}{t_{1/2}^{Total}} = \sum_{i=1}^{n} \left(\frac{1}{t_{1/2}^{1}} + \frac{1}{t_{1/2}^{2}} + ... \frac{1}{t_{1/2}^{n}} \right) \tag{2.12}$$

$$1 = \sum_{i=1}^{n} (BR_1 + BR_2 + ...BR_n) \tag{2.13}$$

$t_{1/2}^{x}$ represents any partial half-life of decay x and BR_x represents its branching ratio.

2.2.1 Alpha Decay

Alpha decay is when an unstable nucleus undergoes spontaneous radioactive decay by emission of a ^{4}He nucleus. It is described by

$$^{A}_{Z}X \ \rightarrow \ ^{A-4}_{Z-2}Y \ + \ ^{4}_{2}He, \tag{2.14}$$

where X in the starting element with proton number Z and mass A. Y is the daughter nuclide with proton number $Z-2$ and mass $A-4$. Alpha decay from a mother nucleus also carries away quantum angular momentum l_α. Angular momentum is a conserved quantity and the amount that an α particle can possess is limited by the selection rules,

$$|I_{initial} - I_{final}| \leq l_\alpha \leq |I_{initial} + I_{final}|. \tag{2.15}$$

The parity of the final state can be determined by $\pi_{final} = \pi_{initial} \cdot -1^{l_\alpha}$. Alpha decay occurs in neutron-deficient nuclei, starting at Z = 52 with tellurium and becoming more common above N = 84, two neutrons above the N = 82 neutron shell closure. It can be viewed that the emitted α particle is 'preformed' inside the nucleus before emission. The Rasmussen model [25] shows the α particle tunnelling through the Coulomb barrier but it is difficult to determine the exact preformation point. In the work of Qi *et al.* [26, 27], the α particle is modelled from the point where the nuclear force is no longer present, so as to avoid sensitivity to choice of nuclear potential, outwards through the Coulomb barrier.

When an α particle is emitted, the energy that is released is defined as the Q_α value. This quantity can be calculated from the difference in the masses of the mother particle and the daughter particle,

$$Q_\alpha = (M_{Mother} - M_{Daughter} - M_\alpha) \cdot c^2. \tag{2.16}$$

The measured α particle energy E_α can be used to determine the Q_α value using

$$Q_\alpha = E_\alpha \frac{M_{Mother}}{M_{Daughter}} \approx E_\alpha \left(1 + \frac{4}{A_{Daughter}}\right). \tag{2.17}$$

When combined with mass systematics, Q_α values can be used to determine other useful quantities like Q_p and Q_{2p} values, which can in turn be used to predict the primary decay mode of undiscovered nuclei. The half-life of an α decay is also important when comparing nuclei to one another through calculation of the reduced α-decay width. Decay widths can indicate whether a particular decay path is allowed or hindered, with very low values possibly indicating spin, parity or structural changes. The reduced width δ^2 is calculated with $\delta^2 = {}^{\lambda h}/_{P}$ and P is calculated by

$$P = -\int_{R_i}^{R_0} \frac{(2M)^{\frac{1}{2}}}{\hbar} \left[V(r) + \frac{2Ze^2}{4\pi\epsilon_0 r} + \frac{\hbar^2}{2mr^2}\, l(l+1) - E\right]^{\frac{1}{2}} dr, \tag{2.18}$$

where R_0 and R_i describe the limits of distance from nucleus r from 0 to infinity, respectively. M is the reduced mass and l is the orbital angular momentum of the α particle, Z is the proton number of the daughter nucleus and E is the Q_α value of the reaction with a screening correction [28]. The first term is the central nuclear potential, the second term is the Coulomb term and the third term is the spin-orbit term. The potential $V(r)$ is different for different decay types and for α radiation, the Igo potential is used [29], which is defined as

$$V(r) = -1100 \exp\left(-\left[\frac{r - 1.17A^{\frac{1}{3}}}{0.574}\right]\right) MeV, \tag{2.19}$$

where A is the mass of the mass number and r is the distance in fermis. This potential gives a good fit for target elements between Ar and Pb, and closely resembles a Woods-Saxon potential. Finally, the half-life of a nucleus must be known in addition to its energy so the reduced width can be calculated. In this way, the reduced width constitutes an energy, mass and angular momentum independent means of comparing different α-decaying species. Deviations from overall trends in reduced widths are therefore often indicative of nuclear structure effects.

2.2.2 Proton Emission

Proton emission is a relatively rare decay type, occurring only in proton-rich nuclei or from a high-lying excited state following a β-decay (β-delayed proton emission). It is defined as an unstable nucleus emitting a proton, and is described by the following formula,

$${}^{A}_{Z}X \;\rightarrow\; {}^{A-1}_{Z-1}Y \;+\; {}^{1}_{1}p, \tag{2.20}$$

where X in the starting element with proton number Z and mass A. Y is the daughter nuclide with proton number $Z-1$ and mass $A-1$. The process is similar to α decay,

but does not require the preformation of the emitted particle. This small change makes proton decay especially attractive to study because the decay is inherently very simple; a proton tunnels through the potential barrier and is emitted. The half-life of any given proton decay is extremely sensitive to the spin of the emitting nucleus, and can assist with spin assignments of emitting states. Proton-decay energy measurements can assist with determination of binding energies of the emitting nucleus and the excitation energy of the emitting level.

For a proton to be emitted from ground state, the nucleus has to be proton-unbound, which means the proton separation energy has to be negative. The proton separation energy is the inverse of the proton decay Q value, and can be calculated with

$$Q_p = -S_p = (M_{Mother} - M_{Daughter} - M_{^1H}) \cdot c^2, \tag{2.21}$$

where M_i are the masses of the mother, daughter and hydrogen nuclei. Similarly to α decay, the measured energy of an emitted proton can be used to determine the Q_p value.

$$Q_p = E_p \frac{M_{Mother}}{M_{Daughter}} \approx E_p \left(1 + \frac{1}{A_{Daughter}}\right) \tag{2.22}$$

The reduced proton decay widths are calculated using the Becchetti-Greenlees [30] potential instead of the Igo potential, which is an optical nuclear potential commonly used to calculate reduced proton decay widths.

Chapter 3

Experimental Methods

In this chapter, the basis of fusion-evaporation nucleus formation and of how radiation is detected, the apparatus used and the experiments undertaken in this thesis, as well as analysis techniques used are presented. All the experimental work in this thesis was conducted at the University of Jyväskylä Accelerator Laboratory, Jyväskylän Yliopiston Fysiikan Laitoksen Kiihdytinlaboratorio (JYFL). The author was part of the γ-RITU group, and work was facilitated by the aid of the group and of the accelerator staff.

3.1 Fusion-Evaporation Reactions

Fusion-evaporation reactions occur when a high-energy incident projectile nucleus bombards a target nucleus with enough energy to overcome the Coulomb barrier and fuse the two nuclei together. The recoiling fused nucleus ('recoil') is produced with greater energy than it would have in its ground state. The excess energy is lost by evaporating high-energy particles from the recoil. Typically, a proton-rich nucleus will shed protons and α particles, but neutrons are also evaporated with a lower probability.

This production method can reliably produce proton-rich nuclei approaching or even beyond the proton drip line by utilising nuclear stability drifting away from the N = Z line with increasing Z. Lighter nuclei have higher proton to neutron ratios than heavier nuclei, so the fusion of two such light nuclei results in a compound nucleus that is relatively proton rich. This alone is no longer enough to produce something considered exotic in nuclear physics; the evaporation channels of a given compound nucleus show the probability of it becoming something more exotic. An evaporation channel is defined as the specific set of particles emitted from a compound nucleus, producing a specific residual nuclide. An example from this work is the production of ^{169}Au from a ^{174}Hg* compound nucleus by evaporating 1 proton and 4 neutrons (the 1p4n channel).

3.1.1 Formation of a compound nucleus

In order for two atoms to fuse together, their kinetic energy must be great enough to overcome the repulsive Coulomb force that any two like charged objects experience. If the nuclei become close enough, the strong force becomes dominant and fusion occurs. This minimum kinetic energy requirement is referred to as the interaction barrier. The Bass model [31] was used in this work when calculating interaction barrier heights, and is described by the following equation,

$$B_{int} = \frac{Z_p Z_t e^2}{4\pi\epsilon_0 R_{12}} \left[\frac{R_{12}}{R_{12} + d_{int}} - \frac{1}{x} \frac{d}{R_{12}} \exp\left(\frac{-d_{int}}{d} \right) \right], \tag{3.1}$$

$$x = \frac{e^2}{a_s R_{12}} \frac{Z_p Z_t}{A_p^{1/3} A_t^{1/3}},$$

where $R_{12} = R_1 + R_2 = r_0 \left(A_p^{1/3} + A_t^{1/3} \right)$ is the sum of the nuclear radii, $A_{p,t}$ and $Z_{p,t}$ are the mass and proton numbers of the projectile and target nuclei, respectively, a_s = 17.23 MeV is the surface term from the liquid drop model, d and d_{int} are adjustable parameters for the range of the nuclear force and the interaction distance, respectively. For lighter $A \leq 40$ nuclei the barrier height is more dependant on d, whereas for heavier nuclei it depends more on d_{int}. Bass states that values of d = 1.35 fm and $d_{int} = 2d$ = 2.70 fm are valid for a wide range of projectile and target masses assuming one takes r_0 = 1.07 fm [31].

Whether a projectile nucleus impinging on a target nucleus will have sufficient kinetic energy to overcome this interaction barrier can be determined. The centre-of-mass energy of the collision can be calculated from the lab frame energies with equation,

$$E^{CoM} = \frac{m_t}{m_p + m_t} E_p^{lab}, \tag{3.2}$$

where E_p^{lab} is the energy of the projectile in the lab frame. The superscript notations ^{CoM} and ^{lab} indicate the centre of mass and lab reference frames, m_t and m_p are the masses of the target and projectile nuclei, respectively, and it is assumed that the target is at rest in the lab frame. If E^{CoM} is greater than the interaction barrier then the nuclei can fuse together into a compound nucleus described by $^{(Z_p+Z_t)}(A_p + A_t)$. This new nucleus has no 'memory' of the constituents and the collision is perfectly inelastic as both projectile and target are consumed completely. The velocity and energy of this compound nucleus can be calculated from the masses of the initial nuclei and the energy of the projectile such that,

$$v_c^{lab} = \frac{m_p}{m_p + m_t} v_p^{lab} \qquad E_c^{lab} = \frac{m_p}{m_p + m_t} E_p^{lab}. \tag{3.3}$$

The momentum of the compound nucleus in the centre-of-mass frame is 0, so $v^{CoM} = 0$. It therefore follows that the kinetic energy of the projectile particle must add to the

excitation energy of the compound nucleus. Additionally, the binding energy of the compound nucleus is dependent on the binding energies of the projectile and target. It is rarely the case that the sum of the constituent binding energies exactly gives the compound binding energy, so the difference between these two values adds to the excitation energy of the compound system. This binding energy difference is the Q-value of the reaction and can be defined as

$$Q = (m_t + m_p - m_c)c^2 = (m_{initial} - m_{final})c^2 \tag{3.4}$$

The sum of these two constituents exactly gives the excitation energy, $E^* = E^{CoM} + Q$, which determines how many particles can be evaporated to form other nuclides. The evaporation energy of any given nucleon is ≈8 MeV, as one would expect from the binding energy formula. A nucleon at the core of the nucleus would obviously have a higher binding energy, and one at the surface a lower one, but it is a good approximation. The available evaporation channels depend on whether the emitted particle is a neutron or proton, the quantity of each in the nucleus and whether they belong to a closed shell or not. Compound nuclei produced near the proton drip line will preferentially evaporate protons because the nucleus becomes stable more quickly relative to evaporating neutrons. This means the neutron evaporation channels have a lower cross section. Producing nuclei in this way favours yrast states.

3.2 Beams and Targets Used

The beam in all reactions in this work was ^{78}Kr, supplied by the K130 cyclotron. The targets and beam energies used are shown in Table 3.1.

Table 3.1: The beam energies, targets and irradiation times for the experiments reported in this work. The incident beam was ^{78}Kr in each data set and the beam energies given were measured upstream of the target. The target thicknesses are the nominal values provided at point of manufacture. Table taken from [1].

Beam Energy [MeV]	Target	Target Thickness [$\mu g/cm^2$]	Beam Charge State [e]	Irradiation Time [h]	Average Intensity [pnA]	Data Set	Local Code	Traces Taken
418	^{92}Mo	500	15+	67	12	A	L04	Yes
418	^{96}Ru	170	15+	257	12	B	L04	Yes
390	^{96}Ru	170	16+	179	5	C	R52	No

The ^{96}Ru target was a foil of 96.52% isotopic enrichment supported by a 60 μg/cm^2 thick layer of carbon. The target was mounted so that the carbon layer was upstream of the ^{96}Ru material. The ^{92}Mo target was a self-supporting foil of ∼97% isotopic

enrichment. The electric and magnetic fields of MARA for data sets A were chosen to optimise the transmission of E_k = 169 MeV, A = 165 and q = 33.5e particles. For data set B, they were optimised for E_k = 169 MeV, A = 169 and q = 33e particles and for data set C E_k = 165 MeV, A = 170 and q = 34.5e particles. The 390 MeV beam energy was selected for production of the four-particle evaporation channels with reference particle ^{170}Hg. The 418 MeV beam energy was selected for production of the 1p4n evaporation channel with reference particles ^{165}Ir and ^{169}Au.

3.3 The MARA vacuum-mode mass separator

The Mass Analysing Recoil Apparatus (MARA) vacuum-mode mass separator is a device available for nuclear spectroscopy studies at JYFL [32]. The main component that distinguishes it from other separators, most notably from RITU which is less than 10 m away, is the large titanium plate electrostatic deflector that sits at the heart of the separator. The separator has a $Q_M Q_M Q_M D_E D_M (+Q_M$ correction) configuration (see Figure 3.1), where Q represents a quadrupole magnet, D a dipole, and subscripts $_M$ and $_E$ denoting whether they generate a magnetic or electric field. This combination gives MARA the capability to separate ions by their mass to charge ratio. This section will detail the main components of MARA, its operating principles and any ancillary and auxiliary detectors. For a more detailed description of MARA, refer to the thesis of Jan Sarén [32].

3.3.1 Target Position

The target position of MARA sits downstream from 2 quadrupole magnets (not pictured in Figure 3.1) used to focus the beam onto the target after being steered into the MARA cave. The target chamber is before the 3 quadrupole magnets seen in Figure 3.1, but is not shown. It can contain a variety of target foil holding apparata, including but not limited to a 3 target ladder, a four target fan, an 11 target windmill and a rotating target holder than can continuously rotate a foil target. It also houses a carbon "reset foil" after the main target position to ensure that all recoiling nuclei have the desired charge state distribution. Sometimes, short-lived isomers are produced and decay directly, altering the charge state of that nuclide. In the carbon foil, all ions either capture or lose electrons many times such that statistically the Gaussian distribution of charge states is restored. A carbon foil can also be mounted at the entrance to the chamber, with the purpose of reducing the energy of the beam by a small amount. This "degrader" foil can be helpful when the incident beam energy needs reducing by a small amount, such that retuning the cyclotron used to produce the beam would not have enough sensitivity or would take too long. The target chamber may also house the JYU Tube detector, which was not used in this work. A separate, smaller target chamber, with identical capabilities except the ability to hold the target windmill or rotating targets, can be used when JUROGAM III is at the MARA target position.

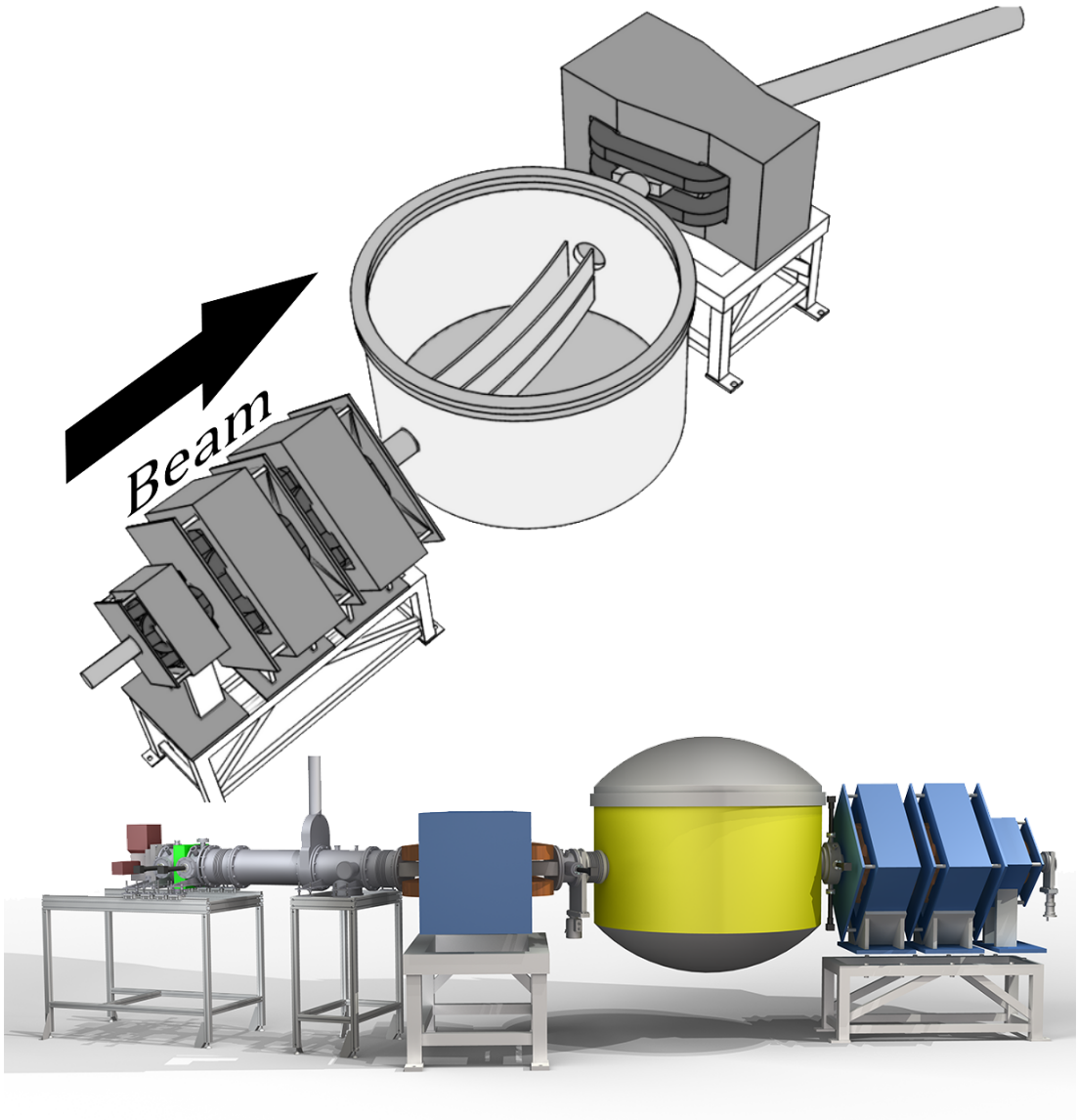

Figure 3.1: The main optical components of MARA shown as they appear in the separator. The configuration in the direction of the beam (indicated on figure) is $Q_M Q_M Q_M D_E D_M (+Q_M$ correction). Note that the beam is incident from the left of the top figure and from the right of the bottom figure due to the orientations MARA is shown in.

3.3.2 Mass Separation

The main purpose of MARA is to separate certain desired nuclides from the vast plethora produced by the reactions between beam and target. This is done by taking advantage of certain properties of the motion of a charged particle in the presence of an electric or magnetic field. Overall, the motion is described by the Lorentz force.

$$\vec{\boldsymbol{F}} = q\left(\vec{\boldsymbol{E}} + q\vec{\boldsymbol{v}} \times \vec{\boldsymbol{B}}\right) \tag{3.5}$$

Electrostatic Deflector

The MARA electrostatic deflector consists of two titanium plates, 140 mm apart from one another, with a curvature radius (ρ_0) of 4.000 m and a height of 40 cm. This gives the cathode a curvature of $R_1 = 3930$ mm and the anode a curvature of $R_2 = 4070$ mm. More details are listed in Table 3.2. These plates were manufactured by Danfysik A/S, and constitute the most expensive single component in the whole separator. They were made with very high precision as the field between them used to separate the recoils in the ion-optical particle region must be constant. Only ≈10 cm of their 40 cm height is actually needed, but the extra height means electric field deviations at the top and bottom edges will affect the recoils as little as possible. The plates also have shunts at these edges to minimise the fringing electric field. There is a 15 mm gap in the anode extending from ≈ 10° to ≈ 19° along the principle beam axis (the axis of the beam before it hits the target foil). This is so that the majority of the unreacted beam can be dumped without touching the plates themselves. This 'split anode' was a very challenging component to model and design. The gap is large enough that even in extreme cases the unreacted beam can be dumped, but small enough that it does not cause deviations in the electric field. Small shims were introduced to the edges of the anode around the gap to assist with maintaining field uniformity. Both cathode and anode can be individually biased with a F.u.G. HCH series 250 kV power supply.

The electric field generated at a given voltage between two parallel plates is given by

$$E = \frac{V}{d}, \tag{3.6}$$

where E is the electric field strength in Vm^{-1}, V is voltage in V and d is plate separation distance in m. The force exerted on the particle is then given by the first term in the Lorentz equation,

$$\vec{\boldsymbol{F}} = q\vec{\boldsymbol{E}}. \tag{3.7}$$

We can use this relationship to form the idea of rigidity. Electric or magnetic rigidity describes the resistance of the path of a particle in motion to being bent by an electric or magnetic field. In this way, rigidity describes a radius of curvature that a given path

will take dependent on the kinetic energy of the particle. Electric rigidity is defined by

$$\chi_E = E\rho_E = \frac{pv}{q} = \frac{2E_k}{q}, \tag{3.8}$$

where χ_E is the electric rigidity, ρ_E is the bending radius of the electric field, p is the momentum of the charged particle, v, q and E_k are its velocity, charge and kinetic energy.

Magnetic Dipole

The dipole magnet poles are 10 cm apart and have a curvature radius (ρ_0) of 1.000 m. Further details about the specifications are detailed in Table 3.2. The dipole was manufactured by Danfysik A/S and has a maximum magnetic field strength of 1.0 T at 430 A. It is also equipped with surface coils that can be used to provide a small quadrupole component to the field (the +Q correction in the configuration).

The motion of a particle in this uniform magnetic field is given by the second term of the Lorentz equation,

$$qvB = \frac{mv^2}{r}, \tag{3.9}$$

where q is the charge of the charged particle in C, v is its velocity in ms^{-1}, m is its mass in kg, B is the magnetic field strength in T and r is the radius of the curved path the particle takes in m. We can see more easily that the dipole separates particles by their mass/charge ratio by rearranging the same formula to give

$$r = \frac{m}{q}\frac{v}{B}. \tag{3.10}$$

The recoiling nuclei are not all of one charge state, but rather of a distribution. Both the electric and magnetic fields can be optimised for the transmission of a particular charge state of a reference particle, usually the one populated most strongly by the chosen reaction. MARA then has an acceptance of between 2 and 5 charge states depending on incident beam energy and reference particle energy, but each of those charge states will be discrete and distinct optically after the deflector. The degree of optical mass separation is dependent on the mass, with heavier nuclei having smaller relative differences between their M/Q values. This means as the mass of the reference particle increases, there are usually more charge states collected and a smaller physical separation between masses. The upper limit for when masses can no longer be optically resolved is calculable using the ion optical equations in reference [32].

The motion of the charged particle in a magnetic field can be described by its curvature radius ρ_B and the magnetic field strength B using the magnetic rigidity equation

$$\chi_B = B\rho_B = \frac{p}{q} = \frac{\sqrt{2E_k m}}{q}. \tag{3.11}$$

It is possible to set the E and B fields to values such that the E_k terms cancel in both

rigidity formulae, negating energy dispersion as a factor. The electrostatic deflector separates nuclides by their energy, and the magnetic dipole splits each charge state by momentum, so the combination gives MARA the optically distinct mass separation it needs.

Table 3.2: The key physical properties of the electrostatic deflector and magnetic dipole present at MARA. More information can be found in reference [32].

	Electrostatic Deflector	**Magnetic Dipole**
Curvature Radius (ρ_0) [m]	4.000	1.000
Bending Angle [°]	20	40
Plate Orientation	Vertical	Horizontal
Plate Separation [mm]	140	200

3.3.3 Mass Slits

In order to limit the amount of data seen at the focal plane, MARA is equipped with a set of adjustable sheets of metal that can be moved in and out of the optical path of the ions to act as a physical barrier to well separated ion optical components. The two main groups used in this work were the 'mass slits', located at the focal plane either side of the MWPC, and the 'energy slits', located between the electrostatic deflector and the magnetic dipole. The degree of physical mass separation at the focal plane is such that one can use the mass slits to stop certain masses from reaching the DSSD. They have three components, two horizontally adjustable slits before the MWPC on linear feed throughs and a third vertically and rotationally adjustable slit of 4 cm width after the MWPC. The horizontally adjustable slits can be brought in to stop a component of the beam on either side whereas the vertically adjustable slit, when dropped down, sits in the middle of the beam axis and can be rotated from parallel to the beam to perpendicular to block more beam components. The energy slits have two components, each a horizontally adjustable slit that can be used to block the horizontal edges of the beam after the deflector and before the dipole.

3.3.4 Focal Plane and Electronics

At the focal plane of MARA, a large vacuum chamber housed both the MWPC and the DSSD, as well as being capable of housing some of the optional ancillary detectors. The DSSD was mounted inside an aluminium chamber extension at the optical focus of the MARA separator and was fixed in place on an aluminium frame cooled with flowing chilled ethanol to -20°C. The DSSD channels were connected with Kapton ribbon cables to vacuum proof connections on the inside of the chamber wall. These then connected to Mesytech MPRT-16 16-channel triggering preamplifiers [33] biased by Mesytech MNV-4 NIM power distribution and control modules [34]. The preamplifiers were connected through Differential to Single signal (DOS) cards to Lyrtech VHS 105 MHz, 14-bit

Analogue to Digital Converters [35] (covered in more detail in section 3.3.4). The bias to the DSSD was supplied by an Ortec 428 Detector Bias Supply [36].

Focal Plane Detectors

The focal plane of MARA is centred around a DSSD that provides the majority of the spectroscopic information needed for identification of nuclides. In this work, two different experiments were conducted, and each used a different DSSD. The first used a 300 µm thick BB17 DSSD from Micron Semiconductor Ltd [37]. The second used a 300 µm thick BB20 DSSD also made by Micron Semiconductor Ltd [38]. The BB20 is a natural upgrade to BB17 and the differences between them are listed in Table 3.3.

Table 3.3: The DSSDs used in this work supplied by Micron Semiconductor Ltd. The nominal bias is the voltage given by the manufacturer supplied datasheet to fully deplete the detector. In practice, it is often necessary to increase the bias above this value when the leakage current increases to keep the detector fully depleted.

DSSD	X Strips (Junction)	Y Strips (Ohmic)	X Strip Pitch (µm)	Y Strip Pitch (µm)	Active Area (mm^2)	Nominal Bias (V)
BB17	128	48	1000	1000	127.97 × 47.97	60
BB20	192	72	670	670	128.61 × 48.21	60

Two 500 µm thick silicon 'punch-through' detectors can be mounted adjacently behind the DSSD to identify light ions that punch through the DSSD. Signals observed in the DSSD without a coincident signal in these silicon detectors or in the MWPC were assumed to be from radioactive decays of implanted nuclei. In this way, they act as a veto detector for overpenetrating recoils and for particles escaping the back of the detector that did not deposit their full energy in the DSSD. The punch-through detectors were installed in both experiments reported in this thesis.

The focal plane can also house additional ancillary detectors that are not used in this work. A series of silicon single crystal detectors can be installed around the DSSD on the upstream side. They make up an open sided box, with the opening upstream to allow the beam in. Their primary purpose is to act as an addback detector for α particles, conversion electrons or protons that escape the surface of the DSSD. A frame outside the vacuum chamber can hold six detectors, either segmented 'clover' type or single crystal 'phase one' type, and two detectors behind the DSSD can be replaced with the GREAT detector. No germanium detectors were used in this work.

Electronics

All detector signals were time stamped by a global 100 MHz clock to allow both temporal and positional correlations to be made between recoils and subsequent radioactive decays within the full detector array [39]. The signals are processed by a digital data

acquisition system (DAQ), instrumented by Lyrtech VHS 105 MHz, 14-bit Analogue to Digital Converters [35]. Each ADC card has 8 channels, with up to seven cards per crate, mounted across five NIM crates. The system is operated in triggerless full data readout mode, but a software filter is used to minimise the amount of data saved to disk. Each channel is present in the MIDAS data acquisition software package, which in turn allows the parameters such as rise time and shaping time to be set. The preamplifier outputs can be digitised to a 'trace', showing the shape of the signal passed to the DAQ. If traces are being recorded, each channel can be individually toggled to record traces of a user defined length of time. The channels are all connected to a program called MERGE, also based in MIDAS, which combines the data from all five crates into a single stream, which is passed to an event builder. This is the stage where the filter, if present, is applied, and where data is passed either to a tape server to be written to disk or to an online GRAIN proxy to be analysed in real time with GRAIN (see section 3.5).

3.3.5 Useful Quantities

Cross Sections

Production cross sections of nuclei seen in event data (i.e. not in traces and after 5μs when traces were being collected) were estimated from the measured yields of the nuclides of interest using

$$N_{\text{Produced}} = N_{\text{Det}}[\text{s}^{-1}] \cdot \frac{1}{\eta_{\text{trans}}} \cdot \frac{1}{\eta_{\alpha}}^{2} \cdot \frac{1}{\eta_{\text{flight}}}, \tag{3.12}$$

where N_{Produced} is the actual number of atoms produced per second, N_{Det} is the number of atoms detected per second and η_{trans} is the MARA transport efficiency, which varies between ∼20 - 40% depending on how many charge states of a nucleus are collected in the DSSD. Usually between 2-5 charge states are collected for a given mass corresponding to lower and higher overall transmission efficiency, respectively, as discussed in Section 3.3. In addition, the transmission is lower for the αXn evaporation channels compared with the pure Xn evaporation channels. This is because when an α particle is emitted in flight, the resulting momentum the recoiling nucleus experiences is large. Emitting the four particles individually usually does not affect the flight path as much as they are rarely all emitted in the same direction. The transport efficiency was simulated for each of the reference ions according to the different settings of MARA used during the experiment. η_{alpha} is the full energy α-detection efficiency, squared because at least two α-particles had to be detected for any given nuclide assignment. In this work the α-detection efficiency was measured to be ∼70% from 5 well-defined peaks in a parent-child matrix slice versus their escapes and background. η_{flight} is the correction due to losing some counts from the 600 ns flight time through MARA. This is a very minor correction and does not have much impact on the resulting cross section. For

nuclei observed in traces, the cross sections were estimated using

$$N_{\text{Produced}} = N_{\text{Det}}[\text{s}^{-1}] \cdot \frac{1}{\eta_{\text{trans}}} \cdot \frac{1}{\eta_{\alpha}}^{X} \cdot \frac{1}{\eta_{\text{trace}}}, \tag{3.13}$$

where η_{trace} accounts for both the flight time through MARA and the short search time the traces impose on event detection. The value of η_{trace} was calculated individually for different nuclei by using their calculated half-lives to plot a decay curve from their moment of production to a sufficiently long time after that most nuclei had decayed. This curve was integrated to account for the events that occurred during the flight time ($\sim 40\%$ of the total) and the events that occurred after the search time ($\sim 10\%$ of the total). The factor was therefore different for each nuclide due to their differences in half-life. The reason why η_{α} is raised to X rather than two is to account for any number of required full energy α particle captures, although in this work $X = 2$.

Mass-to-Charge Ratios

A feature of the MARA mass separator is its ability to separate ions physically according to their M/q ratio at the focal plane. The only experimental parameter needed for M/Q determination is the MWPC X coordinate of the recoil. The dispersion at the focal plane of MARA $\mathcal{D}$ is 8 mm/(% change in M/Q) [32], meaning that a 1% change in M/Q value will correspond to an 8 mm spatial separation. Section 3.3.2 demonstrates how the electric and magnetic fields of MARA can be optimised for the transmission of a reference particle with energy E_k, mass M_{ref} and charge state Q_{ref}, and section 3.2 lists what the reference particles are for data sets A, B and C. The M/Q value of a recoil is calculated using

$$\frac{M}{Q} = \frac{M_{ref}}{Q_{ref}}(1 + \delta_m), \tag{3.14}$$

where δ_m is the relative difference in M/Q compared with the reference particle, which can be calculated from the MWPC X coordinate. In this work, the M/Q spectra were calibrated using ^{165}Os, ^{169}Pt and ^{170}Pt for data sets A, B and C, respectively. The calibration of data set A will be used here as an example. A correlated x-coordinate distribution for ^{165}Os was collected by selecting events based on daughter and grand-daughter energies.

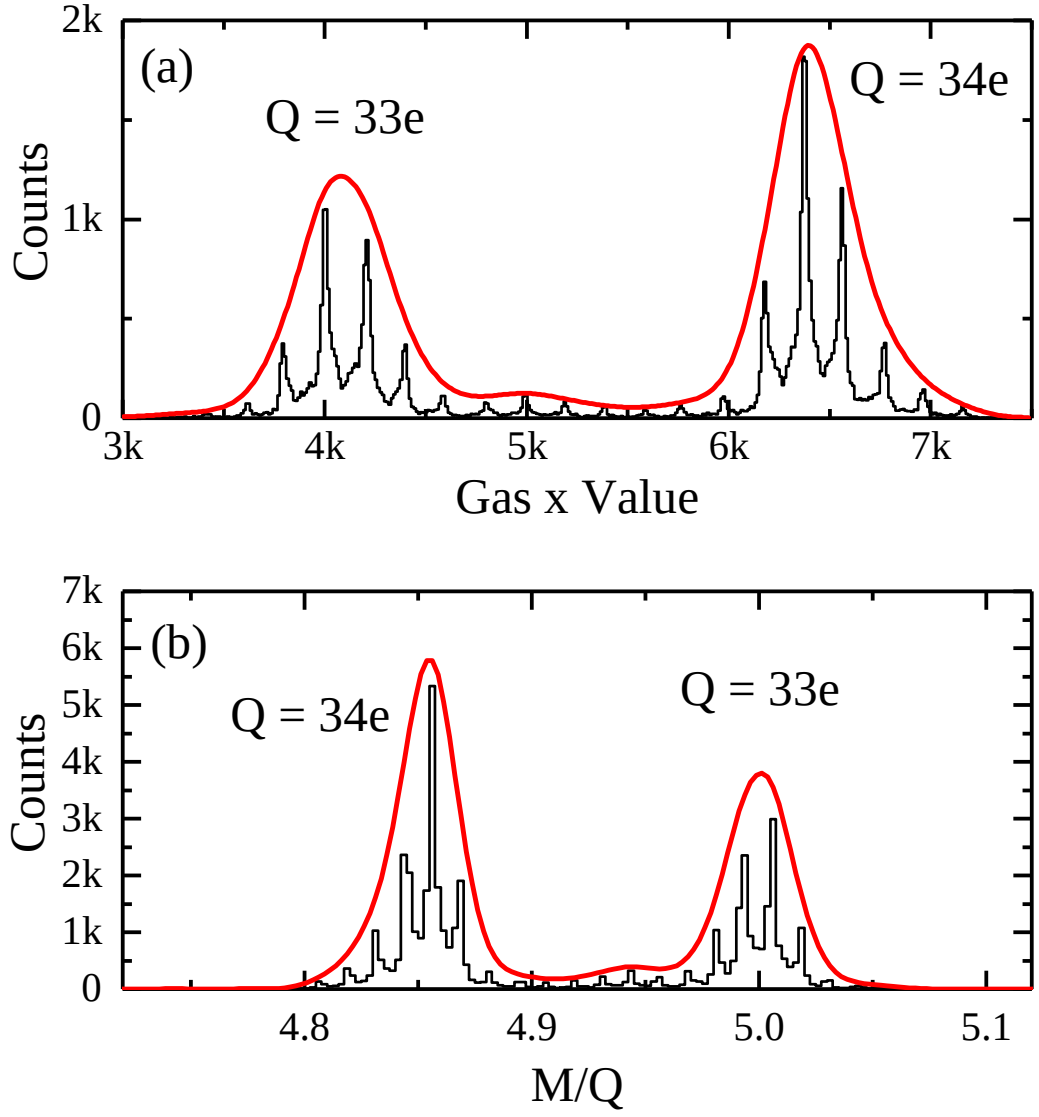

Figure 3.2: (a) The MWPC X coordinate spectrum of correlated ^{165}Os events from data set A. The black line is a histogram of the ADC values compressed a factor of 12, and the spiked patterning is a feature that arises from the local electric field around individual MWPC wires. The red line shows the smoothed distribution of charge states across the MWPC. (b) The M/Q spectrum of correlated ^{165}Os events from data set A. The MWPC wires are still visible, and again the red line shows the smoothed charge state distribution in M/Q.

These MWPC coordinates were plotted on a histogram from 0 to 16,384, the full range of the MWPC. Two clear peaks are present, corresponding to two collected charge states. Figure 3.2(a) shows both peaks, and the individual wires in the gas counter are visible in the sharp patterning. Q_{ref} = 33.5e for data set A, so the charge states observed at the focal plane are likely Q = 33e and Q = 34e. This information can be used to calculate the separation δx_{mm}^{Q} of each of the charge states Q from the reference

particle in mm with the formula

$$\delta x^{Q}_{mm} = \mathcal{D}\left(1 - \frac{M/Q}{M_{ref}/Q_{ref}} \times 100\right)$$

where $M = 165$, $Q = 33$e for the lower x-coordinate peak and $M = 165$, $Q = 34$e for the higher peak. The separations from the reference particle will be δx^{33}_{mm} = -12.1 mm and $\delta x^{34}_{mm} = 11.8$ mm for $Q = 33$ and 34, respectively, to a total of $\delta x^{tot}_{mm} = 23.9$ mm from one another. The separation between the two in MWPC coordinates δx^{tot}_{mwpc} can be calculated by taking the absolute difference between the mean coordinate of each peak $\left|\bar{x}^{33}_{mwpc} - \bar{x}^{34}_{mwpc}\right|$. Their ratio gives a factor G to convert MPWC coordinates to mm, so for data set A

$$G = \frac{\delta x^{tot}_{mm}}{\delta x^{tot}_{mwpc}} = \frac{2335}{23.9} = 0.0102.$$

The X coordinate in mm that the reference particle passes through the MWPC at x^{ref}_{mm} can be calculated with

$$x^{ref}_{mm} = \left(\bar{x}^{Q}_{mwpc} - \frac{\delta x^{Q}_{mm}}{G}\right) \cdot G,$$

where x^{Q} can be any charge state Q present in the spectrum. Finally, the M/Q ratio for any incoming recoil with MWPC coordinate x_{mwpc} is defined by

$$\frac{M}{Q} = \frac{M_{ref}}{Q_{ref}}\left(1 + \left[\frac{x^{ref}_{mm} - (x_{mwpc} \cdot G)}{\mathcal{D}} \times \frac{1}{100}\right]\right). \tag{3.15}$$

Figure 3.2(b) shows the M/Q spectrum for the ^{165}Os events in data set A. The individual MWPC wires are still visible in the histogram but the red line represents the smoothed distribution of the charge states.

3.4 Detecting Radiation

The basic principle of many radiation detectors is very similar. When radiation interacts with nuclear matter, electrons are liberated from atomic orbitals. These electrons are collected by using an electric field to draw them to a conductor, and the charge signal upon collection is amplified for analysis by some kind of circuit. For photons, these electrons are produced by the photoelectric effect, Compton scattering and pair production. Electrons, protons and heavier combinations of them with neutrons interact via coulomb scattering, though the mass difference between electrons and nucleons alters how the process takes place.

Detector material and the exact execution of this principle changes depending on the radiation being detected and what characteristic is being measured. For example, when measuring decay energy in low background and low-rate conditions, a semiconductor with a small band gap and low carrier mobility can be chosen. Many electron-hole pairs are produced, enhancing energy resolution, and the low background and rate obviate

issues from the longer collection times. Many detector materials require specialist operating conditions, such as high voltage or low pressure or temperature. The cost of detectors varies greatly with material, with some being made from hyper pure samples or rare elements. The conditions in which a detector will be used limit material choices; high incident flux, certain radiation types, the requirement for low background or high sensitivity, a strong magnetic field or simple physical size. Some detectors can provide particle positions or trajectories by segmenting the sensitive region with the readout electronics. In this section, why the detectors used in this work were suitable choices as well as their operating principles will be described.

3.4.1 Heavy Charged Particles

The process of Coulomb scattering sits at the heart of detecting heavy charged particles. Heavy in this context is used relative to the mass of an electron, i.e. any particle with mass $> 100\,m_e$. When a heavy charged particle passes through the detector material, it liberates electrons from their atomic orbitals and loses kinetic energy. It is possible for the particle to collide with a nucleus, but this is highly improbable considering the nuclei in the detector material only occupy around $\approx 10^{-13}\%$ of the volume. Nucleus-nucleus Coulomb interactions do take place, but do not account for a large proportion of the energy loss. The energy transfer from the heavy charged particle to the electrons is strongly dependent on its mass and charge. The reaction conserves momentum, so a heavier particle relative to the mass of an electron will lose less energy per collision. Assume (as is the case in this work) three scenarios: (a) a proton with energy 2 MeV, (b) an α particle with energy 7 MeV and (c) a ^{169}Au nucleus with energy 169 MeV. The maximum amount of energy a heavy particle can transfer to an electron would be a head-on elastic collision. If the electron is at rest for simplicity, the loss of kinetic energy for the particle would be described by:

$$\Delta T = T\left(\frac{4m_e}{M}\right)$$

where T is the initial kinetic energy of the particle and M is its mass. The energy lost by each particle in the example would be (a) 4.3 keV, (b) 3.8 keV and (c) 2.2 keV. It is obvious that it would take many interactions of this type for a particle to lose all of its kinetic energy, and this is the maximum energy loss per interaction case. Also note that the mass difference would mean the heavy particle would not be deflected by much and would likely not deviate greatly from a straight line. Nevertheless, the particle stopping distance in detector matter is very short because the range of the Coulomb force is infinite, so when travelling through the detector there are constant small interactions, meaning the particle loses its energy slowly but continuously. Particles of the same energy and mass therefore tend to have very similar and precise mean path lengths due to the very high number of small interactions.

Based purely on this model, the energy lost by a charged particle would be linearly

related to energy, but there is another component. The ionisation energy of an atom is usually $\approx Z \cdot 10\,\text{eV}$. Clearly, for all but the lowest energy collisions, enough energy will be transferred to an electron for it to be liberated. In those rare collisions where an electron is not liberated, the atom will become excited, then subsequently de-excite and emit a photon. This energy is not measured by most detectors but is of such negligible contribution to the total deposited energy that it does not affect the result with any meaningful significance. Most of the electrons will be given enough energy that they can also ionise another atom, which are referred to as secondary electrons. We must include all the electrons liberated in our model as to account for the full charge deposition the detector will measure.

The relationship between the range of particles in matter and their energy and mass was first described by Hans Bethe in 1930. The equation is often referred to as the Bethe-Bloch formula after one of the corrections made to it accounting for electrons carried with the particle losing energy. It can be found in many textbooks (for example see reference [21]).

$$-\frac{dE}{dx} = \left(\frac{e^2}{4\pi\epsilon_0}\right)^2 \frac{4\pi z^2 N_A Z \rho}{mc^2\beta^2 A}\left[\ln\left(\frac{2m_e c^2\beta^2}{I}\right) - \ln(1-\beta^2) - \beta^2\right], \tag{3.16}$$

where $v = \beta c$ and z are the velocity of the particle and its proton number, ρ, Z and A are the density, atomic number and mass of the matter it is travelling through and $N_A = 6.022 \times 10^{23}\ \text{mol}^{-1}$ is Avogadro's number. I is a parameter used to determine the average ionisation and excitation energies for the atoms in the material. In principle this could be calculated, but in practice it is treated as an empirical constant with value $I = 10 \cdot Z$ eV. The mean range of a particle can be found by integrating this formula from its initial energy to zero, but it breaks down at low energy when the particle begins to capture electrons and $E \leq I$. This relationship is shown in Figure 3.3.

3.4.2 Gas-Filled Counters

Like many detectors, the function of a gas-filled counter is to use a constant electric field to drive the electrons created by the passage of a heavy charged particle through matter towards electrodes for collection. The simplest form of such a detector would be a parallel plate capacitor filled with air. When a heavy ion strips electrons from atoms in the air, recombination is prevented by the drift field inside the parallel plates, which pulls the electrons towards the positively charged plate (anode). The stripped positively charged ions are pulled towards the negatively charged plate (cathode). The amplitude of the observed signal will be directly proportional to the number of electrons produced in the interaction and independent of the voltage driving them (providing it is high enough to prevent recombination). This signal would be small and often require amplification by a factor of tens thousands before it could be studied. This region of operation where only the primary produced electrons are collected is the operating mode of an ion chamber.

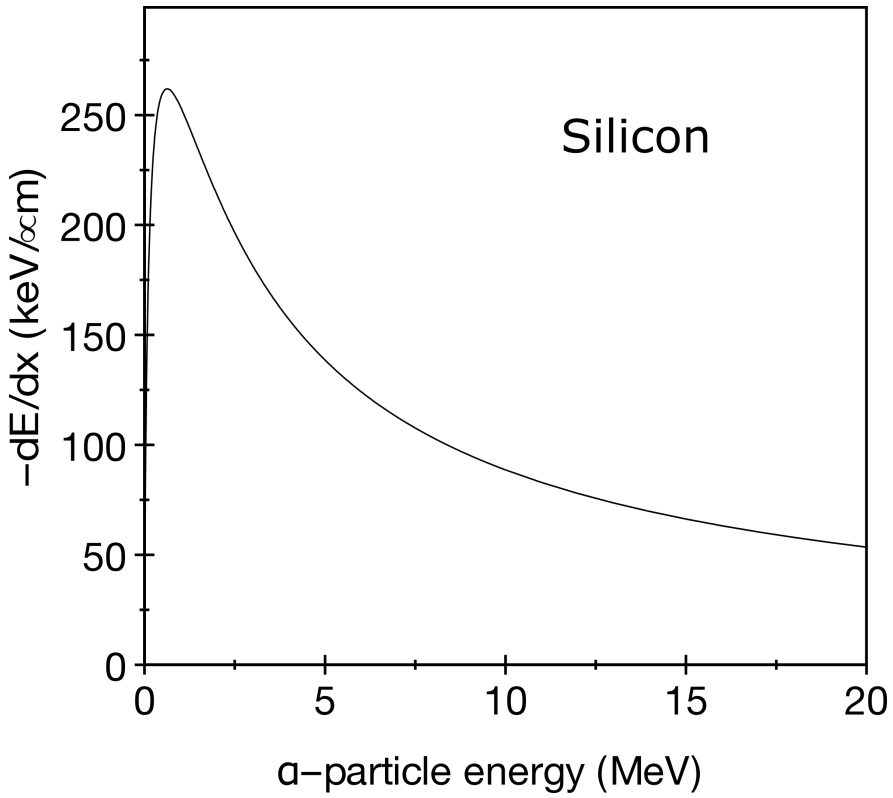

Figure 3.3: The relationship between energy lost per unit distance and current α-particle energy in silicon.

The collection time of the primary charge produced by a particle is on the order of milliseconds, which is slow compared with many nuclear lifetimes. This long collection time precludes use of the counter for monitoring high energy events or high activity rates. Collection times can shortened to a few μs by considerably increasing the electric field so that each electron is accelerated upon production. This means much higher activity levels can be imaged while maintaining time resolution between them. When an accelerated electron travels from its production point towards the anode, it has enough energy to liberate additional secondary electrons. These are, in turn, accelerated by the electric field and produce further electrons. This process is called a Townsend avalanche [21], and the strength of electric field needed to trigger it depends on the gas and its pressure, the geometry of the counter and the ionising radiation. The counter is operated so that the number of secondary electrons produced is proportional to the initial energy of the heavy particle. This region of operation is called the proportional region, and counters that operate with electric fields in this region are called proportional counters.

If one continues to increase the electric field even further, soon the avalanche becomes so severe that regardless of where a particle ionises the first atom, the entire counter will participate in the avalanche resulting in the exact same output for any input radiation. This is called the Geiger-Müller region, and is the common operative mode of Geiger counters.

Multi-Wire Proportional Chambers

A Multi-Wire Proportional Chamber (MWPC) is a kind of proportional counter used to track the passage of charged nuclei. Generally this counter consists of two planes of thin wires, 2-3 mm apart, spaced at regular intervals. In most cases the two planes will have wires aligned at 90° to one another and biased to ∼500-1000 V. The wires act as a cathode, drawing electrons with locally strong electric fields towards the grid with little lateral motion. The walls of the chamber act as the anode, usually at ground. A low pressure gas with a low ionisation energy flows through the chamber. The charge produced when a particle passes through is collected by the wires nearest the ionisation path, allowing 2 dimensional spatial information to be inferred from which wires collect charge pulses. This kind of detector can also be used in a telescope arrangement to track longer path lengths of radiation.

Both experiments in this work used the same MWPC. A grid of 20 μm gold-coated tungsten wires with 1 mm spacing was biased to 485 V with a Mesytech MHV-4 high precision bias supply unit [40]. The flowing isobutane gas at a pressure of 3.5 mbar was confined by two thin Mylar windows. An Ortec 566 Time-Amplitude Converter (TAC) [41] is used to determine which wire the charge was collected from, as each wire is connected in series through delay lines.

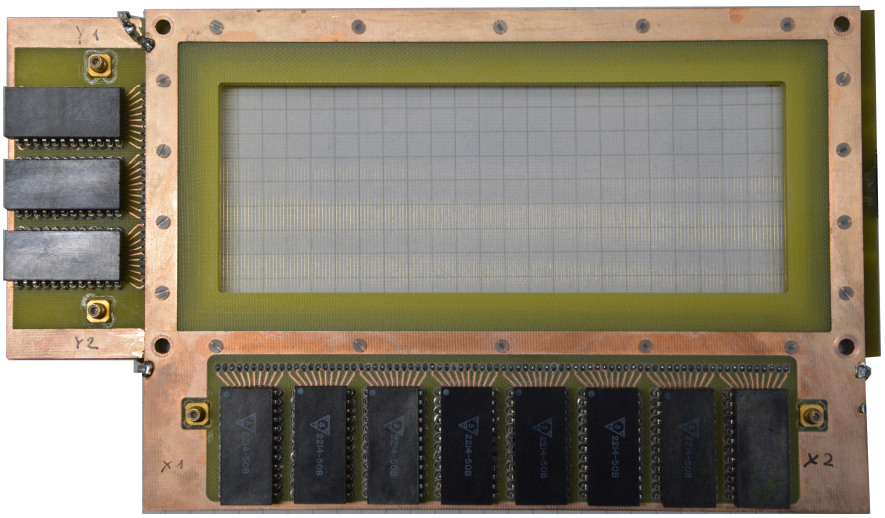

Figure 3.4: The MWPC used in this work. The vertical gold coated wires are visible on the front side of the counter.

3.4.3 Semiconductor detectors

Semiconductors can be characterised by their band gap, typically ∼1 eV, which is the energy required to promote an electron from the valence band to the conduction band. The valence band is always considered full and is comprised of the electrons bound by the crystal structure and therefore not free to conduct charge. The conduction band is seen as a continuous level above which any electron is not bound by the crystal, and can therefore contribute to conduction. For some detector materials this gap is so small that the thermal energy of an electron at room temperature can be great enough to promote it across the band gap. Such detectors are cooled with varying degrees of cryogenics in order to reduce thermal noise.

To make a semiconductor detector, two electrodes are connected to either side of a p-n junction, a reverse bias is applied which creates an electric field and a region of semiconductor is depleted of free charge carriers. When radiation passes through this 'depletion region', the electrons that it ionises are promoted from the valence band to the conduction band, the electric field moves them towards the cathode and they produce a pulse that can be measured. The holes that the electrons leave behind in the valence band can also be thought of as slower moving charge carriers, hence this process is often referred to as electron/hole pair generation. The number of electron/hole pairs generated is proportional to the energy of the ionising radiation, and the average energy needed to create one electron/hole pair, found by taking the average of the ionisation energies of the electrons bound to a Si atom, is well known for most common semiconductor materials. The energy of radiation can therefore be determined from

the number of electron/hole pairs it generates, and the low energy needed to produce any given electron/hole pair relative to the energy of most measured radiation gives semiconductors very high ΔE resolution. The statistical variation of the pulse height is very small due to the number of electrons that produce it. Electrons tend to have high mobility, so semiconductor detectors can have good timing resolution. Semiconductor detectors are solid crystals, so compared with gaseous or liquid detectors, they have small form factors which can stop high energy particles and measure their energy in small or restricted spaces.

Double-sided Silicon Strip Detectors

In this thesis, the only semiconductor detector material used was silicon. Silicon detectors offer very good energy and timing resolution and can be manufactured in a variety of specifications. A typical silicon detector will consist of a single crystal, cut along a specific crystal axis to maximise electron-hole mobility, bonded to a frame with the smallest possible surface area loss and electrically bonded with a very fine wire. The difference between an unsegmented silicon detector and a double-sided silicon strip detector (DSSD) comes from how the charge carriers are extracted. A typical DSSD will have strips on the surface of the silicon, often etched on through lithographic techniques, running top to bottom on one side and left to right on the other. The silicon wafer is first passivated around 300°C to form a layer of silicon dioxide on the surface of the crystal. Next, a photoresist mask is applied and channels where the p-type dopants will be added are etched. A tandem or linear accelerator is used to implant a $\sim$100 keV beam of boron, other group 3 element or some other acceptor into the silicon to a depth of $\sim$0.5 μm, where it acts as a highly concentrated p-type dopant. With the p-n junction set up within the silicon, the wafer is placed into a sputtering or ion evaporation chamber where the metal contacts are added by heating a metal target (typically aluminium). The silicon dioxide is then chemically removed from the detector surface but remains present around the edges. The back side is coated with phosphorus or other group 5 donor material to act as a strong n-type backstop. The silicon is manufactured thin enough (often $\sim$100μm) that charge is collected from both sides of the detector. The grid pattern means that each side of the detector will collect charge in the two strips closest to the origin of the charge carriers. The top to bottom running wires give information on where the origin of the charge is on the horizontal x axis, and the left to right wires give information on the y position. These areas of sensitivity are referred to as strips, because it is a strip of possible charge origin. The width of the sensitive area of a strip, or the distance between two wires, is called the strip pitch, often on the order of 1-2 mm. There is a fundamental limit to how narrow the strip pitch of a DSSD can be; if the strip is too narrow then highly energetic particles like recoiling nuclei can become blurred across more than one, rendering the positional sensitivity less useful. This is especially true when one considers that the electric field at strip edges is non-uniform and difficult to model accurately. If a detector event

signal comes from a single x strip and y strip, then the overlap of the two is where the charge was generated, referred to as a pixel. The number of pixels in a DSSD is the number of x strips multiplied by the number of y strips, i.e the maximum number of individually distinct areas a charge could be detected. The caveat for this excellent spatial accuracy is that a DSSD requires each strip to be read out individually to its own channel. This is usually realised with a large multichannel data acquisition system (DAQ) or equivalent, and often requires banks of multichannel analysers working in tandem.

When biasing a DSSD, the manufacturer often quotes a nominal bias voltage necessary to fully deplete the detector. It is important that the detector be fully depleted so the entire crystal is capable of detecting radiation, maximising the active volume. It is not uncommon to exceed this nominal voltage for a number of reasons, foremost among them that within reasonable limits there are few to 'overbiasing' a silicon detector. Overbiasing can increase leakage current and lead to worse ΔE resolution, but as long as the breakdown voltage is not exceeded, no permanent damage is done by using a greater voltage than is necessary to fully deplete the detector. The leakage current across the bias resistor (typically $\sim 100\Omega$) usually rises throughout an experiment, meaning a higher voltage is required to maintain the electric field. If the experiment involves implanting ions in the DSSD, the ions become an impurity once they have decayed and can trap charge in the same way a dopant acceptor ion would. A higher electric field will strip these impurities more effectively, and minimises the noise they would create. It also minimises the noise from leakage current fluctuations as the detector remains fully depleted at all times.

Pile-Up and Dead Time

When free charge carriers are generated inside a semiconductor detector, the pulse that is collected has to be passed to a preamplifier. The preamplifier converts the charge pulse to a voltage pulse and amplifies it by the gain (usually x1) so it can be processed by DAQ electronics while preserving the energy and timing information. It does this by using parameters called rise time and decay time. In general, the rise time is the time taken to rise from a specified low value to a specified high value. In this case it is the time taken to rise from the baseline to the energy-proportional amplitude of the original pulse. The decay time is typically the time taken to go from 90% of the peak value to 10% of the peak value. In this case it is the time taken to restore the baseline so another event can be observed. The decay time, therefore, is an artificial tail that is added to the pulse from the detector, which causes the system to go into dead time. Dead time is when the detector is capable of detecting additional signals, but the electronics necessary to process the signal are not.

Two different modes were used to deal with dead time in this work, one when dealing with traces and one without. When traces were not being collected, if an event occurred during the dead time, the system does not process it at all and the information

is discarded. This is done to avoid paralysing the system by letting sequential events extend the dead time at high counting rates. When traces are being collected, events that occur during dead time are marked as pile-up events. The pulse is generated in the detector is passed to the preamplifier while it is still shaping the previous event, causing a bump or other feature on the tail of the original signal. These superimposed decays that happen in the tail of another event are referred to as trace decays. It is possible, although unlikely, to have two events within the silicon charge collection time, which is typically on the order of a few ns. The system settings and whether both events happen in the same pixel determine what happens in this instance, but usually the two charges are summed together.

3.5 Software and Code Languages

The GRAIN software package [42] is the standard tool for opening, reading and sorting data produced at the University of Jyväskylä on either the MARA or RITU separators. They both use the same Lyrtech-based data acquisition system (DAQ) which outputs 'run' files in 2 GB increments. GRAIN uses run files as its input and uses a .gains file to gain match the arbitrary energy units of the DAQ channels to keV values on a strip by strip basis. This is done by multiplying the raw channel number for each event by either a linear or second order polynomial fit specific to the X or Y strip the event was observed in. It also uses a configuration file to determine the trigger width, trigger delay and dead time as well as map channels to detector variables in the GRAIN Java classes. This file also allows selection of which channels are used as a trigger and when to ignore piled up events. Careful selection of trigger width is necessary so as to include only coincident information in one 'event'.

During this work, two main languages were employed to analyse data; Java and Python. The GRAIN software sorts data according to a Java 'sort code' and as such Java was used to conduct preliminary analysis, generate histograms and apply gating conditions to data. The sort codes can also be used to implement standard Java language functions outside of the GRAIN classes, so the traces needed for the analysis of ^{169}Au and ^{165}Ir could be exported to external files for ease of analysis. These exported files were then analysed using Python 3.4. This language was selected because of its high level functionality, diverse library of useful data analysis methods, the amount of online resources available, author familiarity and simple to use fitting and plotting features.

3.6 Analysis techniques

Two analysis techniques were used to separate the useful information from the 6 TB of data produced by the two experiments that make up this thesis. The correlation analysis technique is used to identify nuclides based on their known decay chains. The

trace analysis technique allows determination of α- or proton-decay energies of short-lived nuclides that are superimposed on recoil implantation signals selected using the correlation technique. This section discusses the methodologies with examples of how they were used in this work.

3.6.1 Correlation Analysis

Correlation analysis is useful when identifying decay radiation from short-lived exotic nuclides produced in nuclear reactions with low cross sections. Such nuclides are produced at high energies, so are often stopped by implantation in a silicon detector. The energy of any radiation emitted requires no kinematic correction. The average path length of a proton or α in silicon is short compared with DSSD pixel size, but similar to the implantation depth, making a typical full-energy detection efficiency ≈50-70%.

In order to distinguish between these implantations and their subsequent decays, a Multi-Wire Proportional Counter is used. When the MWPC is triggered (by a recoil passing through and generating charge carriers), if a coincident high energy signal (typically ∼100 MeV) is seen in the DSSD within a short time window, this indicates that the energy signal is from an implantation. An event without this MWPC coincident signal is usually assumed to be the decay of a previously implanted nuclide.

When a recoil 'mother' decays, the resulting nuclide left behind after the decay has happened, the 'daughter', is determined by the decay type. If the daughter also has a detectable decay chain, then the subsequent nucleus is referred to as 'granddaughter' and so on. Most α or proton decay chains in this work are only seen for three or four generations before reaching a long-lived β^+ emitter. The probability of detecting the full energy of three sequential αs is ∼34%, dropping to ∼24% for four and so on. The predictability of what the next decay in a chain will be means that characteristic sequence of decay energies and decay times provide a clear signature for identifying new nuclides.

Figure 3.5 shows the chain of decays following the ^{169}Au^m proton decay, one of the main discoveries in this thesis. The α-decay energies for ^{168}Pt, ^{164}Os, ^{160}W and ^{156}Hf are known, so the energies and half-lives of these decays form a unique fingerprint. If an observed decay is followed by decays matching the energies and decay times of ^{168}Pt, ^{164}Os and so on, then that observed decay could be from ^{169}Au. Similarly, if the second decay in the chain is ^{164}Os, and the first decay doesn't match the known α-decay energy or decay time of ^{168}Pt then that decay could be from ^{165}Ir. The greater the number of sequential full-energy α particles seen, the less ambiguous the assignment of the top of the chain becomes.

In order to track these decays using the GRAIN software package, the technique relies on a time stamped 'tagger'. A tagger is a user defined length of time where all decays are tracked and held in memory by GRAIN. Any given event is put into the tagger to allow correlations between it and other events, providing the time between them is shorter than the tagger length. In this work, this length was set at 10 seconds.

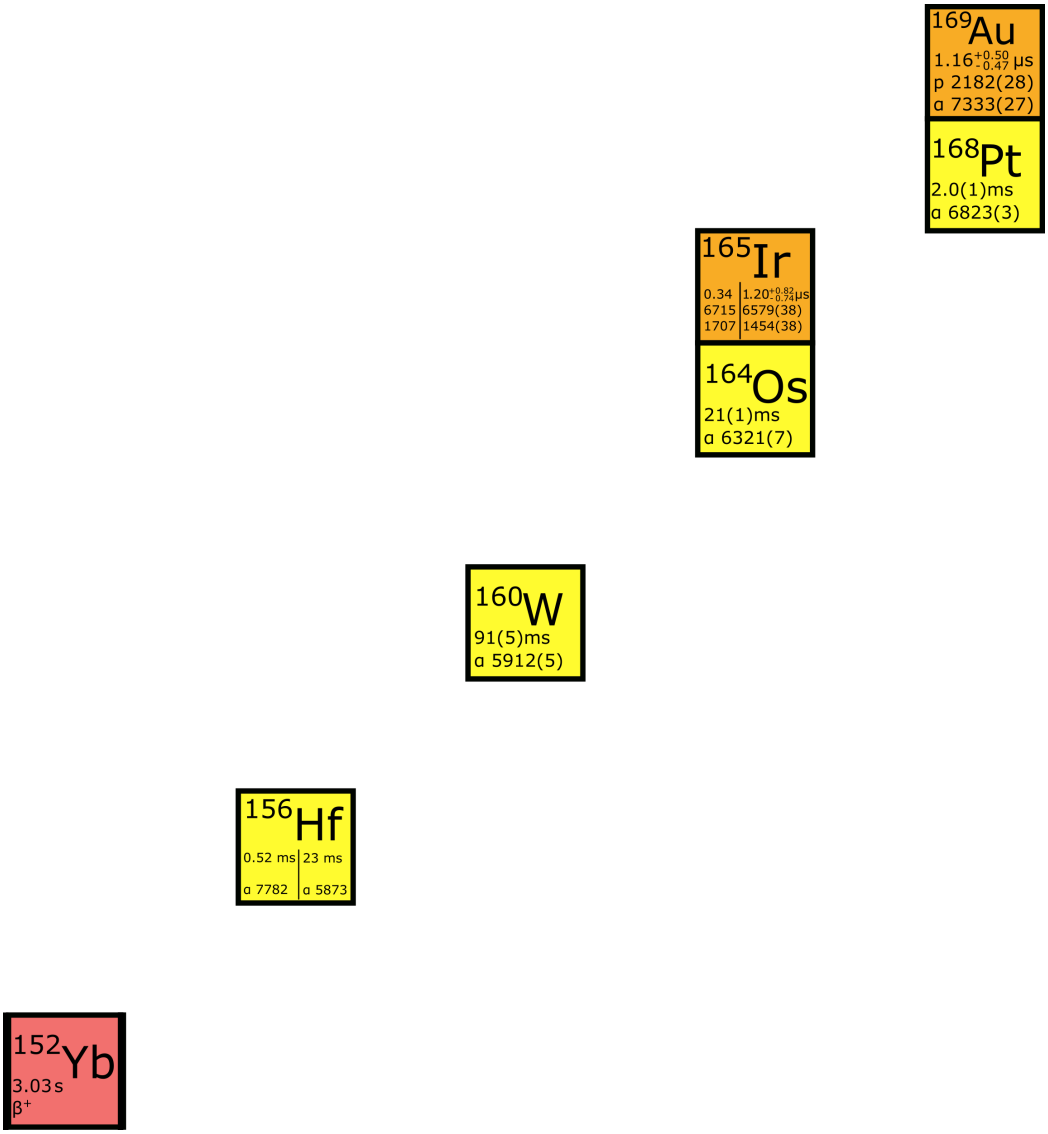

Figure 3.5: The chain of events used to identify proton decays from an isomeric state in ^{169}Au and from both ground and isomeric states in ^{165}Ir, here used to demonstrate how the correlation analysis technique can be used to isolate exotic decays from background. Orange nuclides primarily decay via proton emission, yellow by α-decay and burgundy by β^+ decay.

While the rate of events in the DSSD varied throughout the experiment, the total recoil rate in the DSSD after punch-through veto conditions had been applied was typically $\approx 100 - 500\,\text{Hz}$. Although the distribution was not uniform across the DSSD, the probability of a second recoil ion being implanted before short-lived decay chains were completed was low.

In order to distinguish recoils from primary beam, a Time of Flight versus Energy (ToF-E) gate was used. A two dimensional gate was created around the recoils, as their energy versus time of flight signature is different from that of the beam. If a decay event occurs following a recoil in the same pixel, then that event is considered 'correlated'. By plotting an energy spectrum of only correlated decays, the background seen is greatly reduced compared with plotting every decay-like event. This can be seen in the comparison between the main plots and the insets in both (a) and (b) in Figure 3.6, which also shows the effect of excluding all correlated decays where the recoil and event more than 10 ms apart.

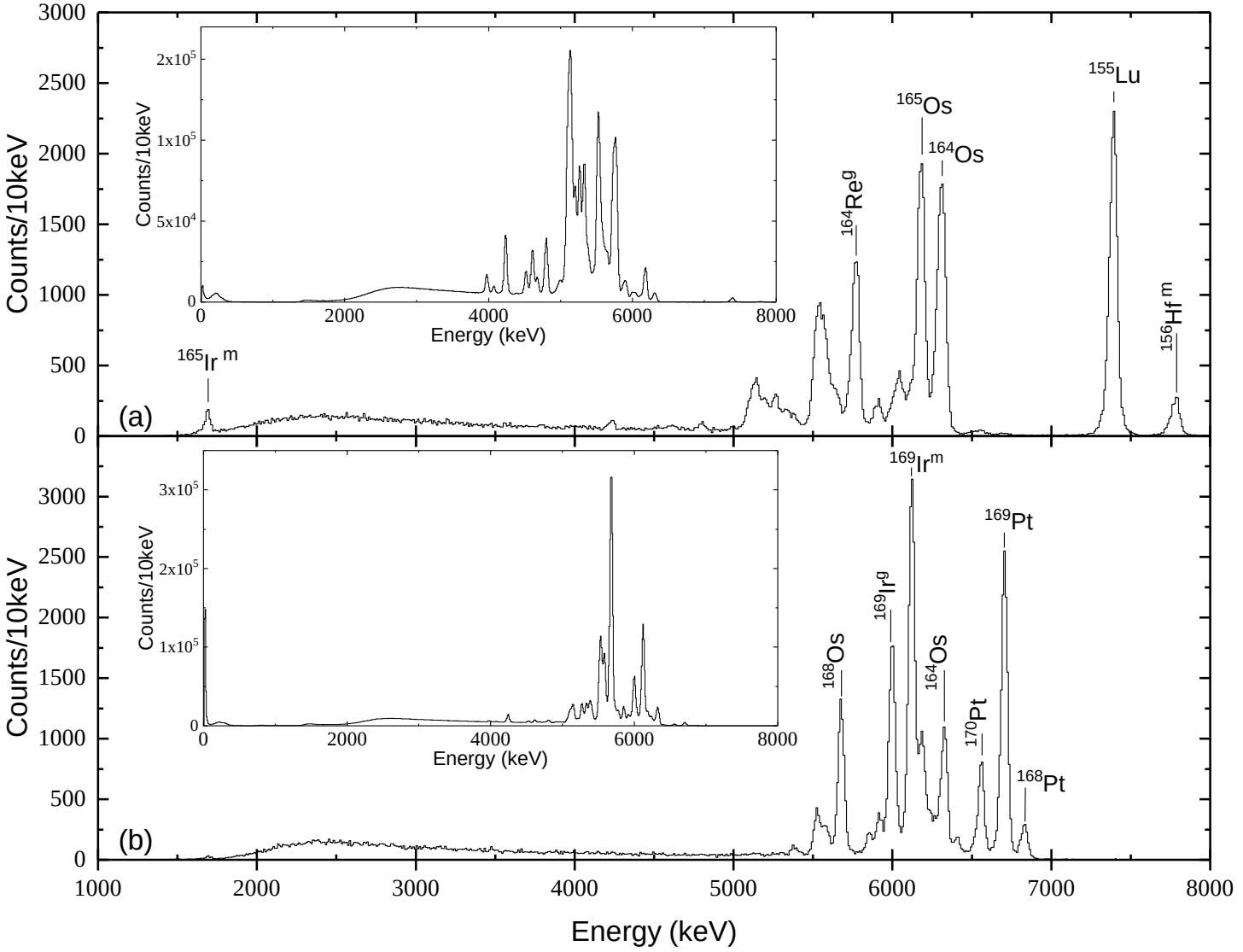

Figure 3.6: A decay product spectrum shows α-decay energies that follow a recoil within 10 ms from (a) data set A and (b) data set B. In both cases the inset shows the uncorrelated spectrum of α-decay energy in the same data set.

3.6.2 Trace Analysis

When a recoil is implanted in the DSSD, it creates a large number of charge carriers (for silicon, around 10^8) which are collected to produce an output pulse. The charge pulse from the silicon is passed to the preamplifier, which outputs a proportionally larger, inverted voltage pulse with a rise time and decay time defined by its settings (a typical decay time is ∼10-20 µs). After recoil implantation, the DAQ is unable to process further signals for $\approx 50\,\mu s$ until an electronic 'handshake' happens to signal DAQ readiness. Trace analysis provides a way to see the decays that occur during this dead time by imaging the signal the preamplifier passes to the DAQ. In this work, a sample rate equal to the DAQ clock was used (100 MHz or every 10 ns) to record 5 µs traces. An example of what this looks like is shown in Figure 3.7 (a).

Most traces look similar, restoring back towards the baseline, as the only thing generating the signal is the recoil or decay. Such typical traces are not always observed; a variety of events that can cause a trace to 'pile up'. The methodology for how these traces were separated from raw data and subsequently filtered is explained in detail below.

The baseline restoration in a trace is exponential with a decay constant proportional to $\frac{1}{RC}$, the time constant of the preamplifier capacitor and resistor. However, the time region the trace shows is so short compared with the decay as a whole that it appears approximately linear. In order to analyse the traces, the natural logarithm of them was taken so any slight exponential slope would be linear, making fitting simpler and more reliable as well as reducing the noise level. To take the natural logarithm of the raw trace, each point was multiplied by the following formula,

$$y = \ln\left[-1 \cdot (x_{Trace} - (\mathbf{max}(x_{Trace}) + 1))\right],$$

where x_{Trace} represents the trace height at time x, $\mathbf{max}(x)$ represents the maximum trace height for any time x and y is the result. The trace has the maximum height value subtracted to zero the baseline, and maximum+1 was subtracted to avoid taking the natural log of 0. The traces are negative, so multiplication by -1 makes them positive. The natural log was then taken of the baseline normalised positive traces.

Interesting Traces from Raw Data

The first step in separating interesting traces from raw data is searching for pile-up markers. As discussed in section 3.4.3, an event is marked as piled up when the preamplifier tries to pass a signal to the DAQ before its baseline voltage has been restored. This is the strongest indication that something other than a normal recoil implantation or decay has occurred; almost all piled up signals are deviations from the 'nominal' recoil implantation or decay trace. Figure 3.7 shows examples of what different piled up traces can look like.

The preamplifier pulses available from the BB17 DSSD (no traces were taken using

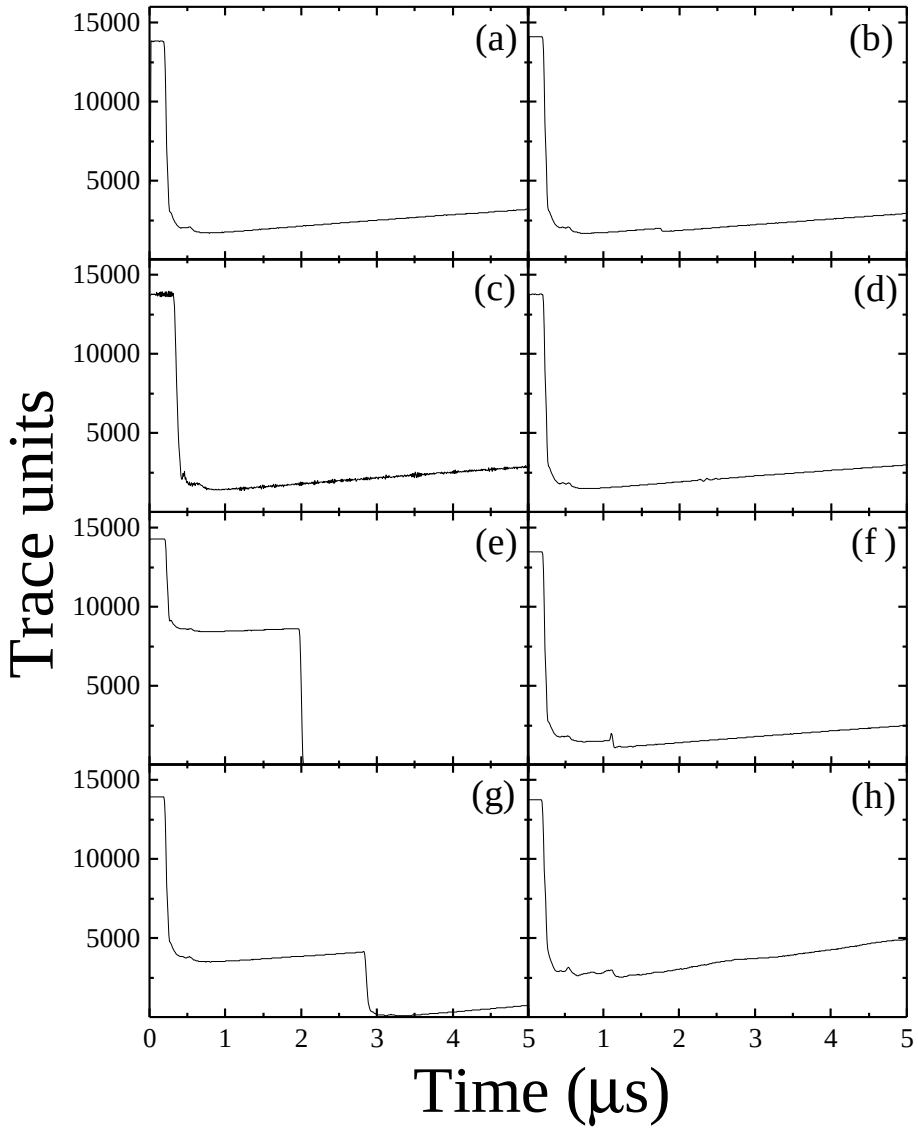

Figure 3.7: Examples of different traces that are marked as piled up. All the traces in this figure are taken from data set B. They show (a) a normal trace, (b) a useful event, possibly a proton decay, (c) higher frequency electronic noise, (d) a short burst of high-amplitude electronic noise, (e) a recoil hitting right after some lower energy previous event, (f) a useful event that has some odd electrical artefact, (g) two successive high energy events and (h) a wobbly signal for unknown reasons. All traces share a common artefact, the small bump around 0.5 μs, which is an unidentified anomaly in all traces.

the BB20 DSSD) were marked with whether the charge was collected from the X or Y side of BB17, or both. Selecting only events which were piled up on both the X and Y sides yields almost entirely proton decays, α decays or other real physical activity. However, some potentially interesting events piled up in only either X or Y, so manual filtering of all piled up events was performed. In addition to piled-up events, a basic algorithm was included in the initial GRAIN sort code to check the trace of any recoil event followed by a decay event. This algorithm scanned from 85 ticks (850ns), when an event could first be distinguished from the recoil implantation, to the end of the trace. If the absolute difference between the trace energy unit at tick (x) and the trace energy unit at tick (x+5) was greater than 80, this could be a real event when translated to keV (corresponding to ∼800 keV), so the trace was marked. If this same deviation happened more than 10 times in one trace, the trace was rejected as this was indicative of large quantities of high amplitude noise. The resulting traces, whether piled up or marked as interesting by the algorithm, were then saved to an external file. They were saved with Y and X strip number, the x-position the recoil passes through the MWPC and the subsequent 4 (or fewer where applicable) same pixel decay y-side energies and decay times. The strip number was recorded because something occurring in a pixel at the extreme edge of the DSSD was more likely to be from an electronics anomaly than from a short-lived decay. The recoil gas x-position was saved to enable calculation of the M/Q value.

The traces were imported into a Python program designed to show the user each trace individually. Useful data were manually filtered by checking traces for superimposed fast decay events, then assessing if energy reconstruction would be possible. This removed any electrical noise pile-up, any occurrences of two recoils hitting the same pixel within 5µs, any events too close to either edge of the trace to reconstruct their energy or any event where the noise was too strong to attempt fitting. The resulting list of selected traces was then saved in a new file for further analysis.

Trace Drop Height and Decay Times

To reconstruct the energy deposited in the detector, it is necessary to get the most precise possible value of the 'trace drop'. The term 'trace drop' here refers to the voltage difference observed when a fast decay is superimposed on a recoil trace, as can be seen in Figure 3.7(b). In ordinary (non-trace) circumstances, to determine the energy deposited in the detector, the full decay curve area from baseline pre-event to baseline post-event would be found by integration. The baseline post-event is not visible in the 5µs traces so a less precise method was used; measuring the drop in trace y units when a fast decay occurs.

It is noted here that the trace sampling method used was an unavoidable limiting factor. A trace has 16,384 y channels (14-bit sample) and a recoil implantation measures ∼10,000 trace units, depending on how the gain is set. This corresponds to an average recoil energy of ∼100 MeV at implantation, meaning each trace y-unit corresponds

to ∼10 keV. The $^{169}Au^{m}$ proton emission energy, predicted to be ∼2 MeV, in turn corresponds to around 200 trace units. This means the proton signal would be around 2% of the overall height of the recoil signal and the deviation from the nominal trace will be very slight. It also means that there is a limit on how precise any value from traces can be, namely the height of any individual y-unit, ∼ 10 keV. Considering it is not abnormal to see a noise level of ±5 trace units, it is clear that any information obtained from trace analysis will have large uncertainty.

In order to find the drop height of each trace event, a Scientific Python (SciPy) linear Orthogonal Distance Regression (ODR) [43] method was used to fit the trace data both before and after the decay. The decay time was initially identified by scanning along the trace for a rapid decrease compared with the normal line. This point was marked, then presented to the physicist to verify that it showed the start of a drop. Each point was manually adjusted, usually between 0 - 4 ticks (0 - 40 ns), so the start of each decay was marked as precisely as possible. Some uncertainty was present as the exact start of a decay is difficult to distinguish as it is an abrupt change and there was noise continuously in the traces. The start was determined as the point at which the trace dropped continuously to its maximum amplitude. This is shown graphically in Figure 3.8.

The traces were then presented to the physicist individually to be marked for one of two fitting methods. If the decay occurred far from the trace edges then the more accurate method, linear fitting, was used and comprised two different approaches. For the first approach, a line was fitted to the data from 100 ticks to the trace drop point, and another fitted from 20 ticks after the drop point till the end of the trace. The vertical distance between the two lines at the drop point was taken as the drop height. To ascertain if there was an optimum point in the drop from which to take the vertical difference, the measurement point was varied from the start to the end of the drop in 2 tick increments. The differences between each of the measurement points sampled were plotted on a histogram, which showed a peak with a centroid at 0 and a FWHM of 2.57 trace units. Therefore, the height difference was calculated at the start of the drop, as there was little impact on the result.

For the second approach, the sections of trace before and after the drop were compared and a line was fitted to the wider side. The gradient was then locked, and the same line was fitted to the average x and average y of the less populous side of the trace. The constant difference between the two lines was taken as the drop height. In order to determine whether the best fit or fixed gradient approach showed better agreement with the trace, both lines were presented to the user and the method used for each trace was determined individually. The best fitting line either side of the drop generally showed a better fit (see Figure 3.9), but when the drop occurred near trace edges the data set between the drop and the edge was often too small for a meaningful fit. In these cases, the forced gradient fit better represented the trace (see Figure 3.10).

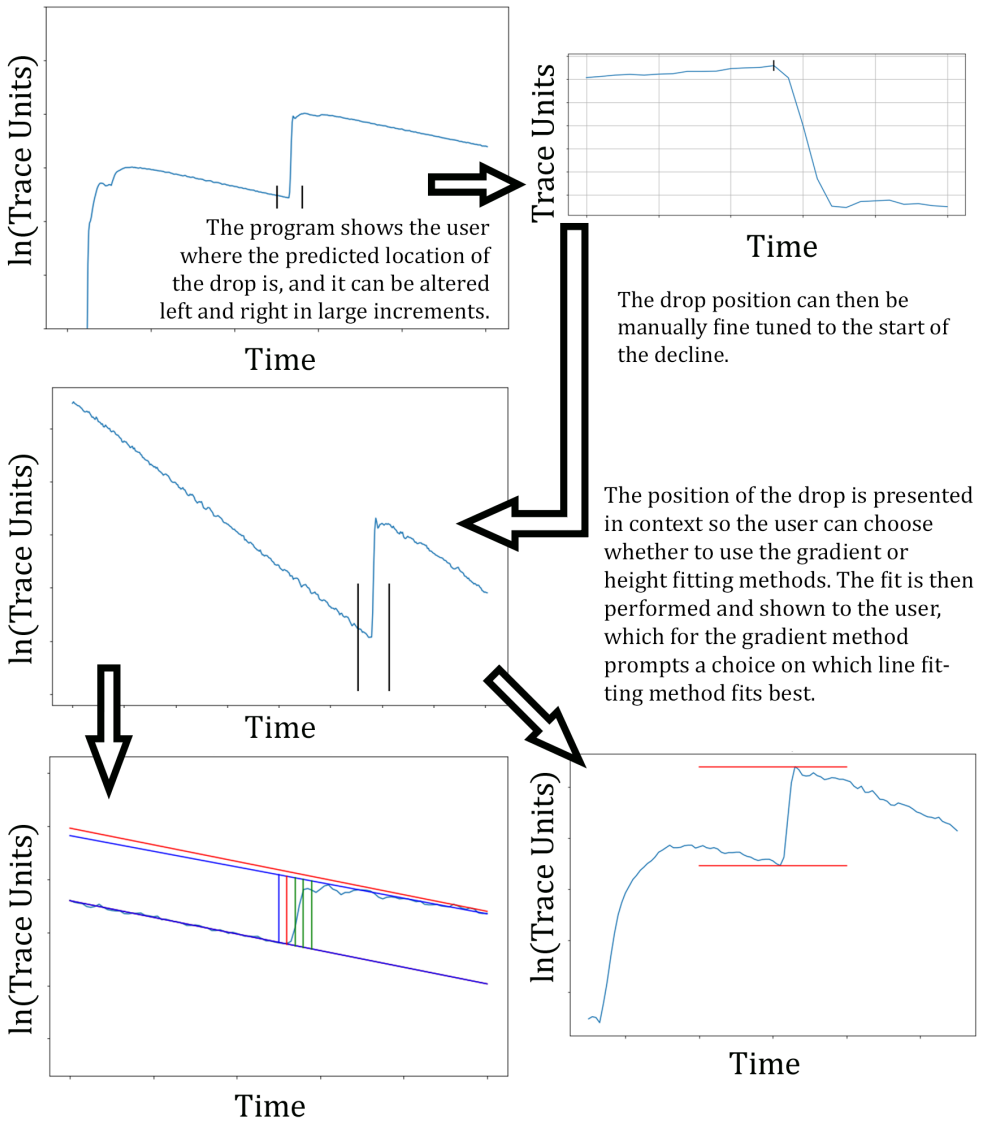

Figure 3.8: The methodology used to identify the decay times and trace drop heights of fast decay events that are superimposed on recoil traces. Time units in all plots are in 10 ns increments, but the exact time is not specified on axes as it is not relevant to the understanding of the method.

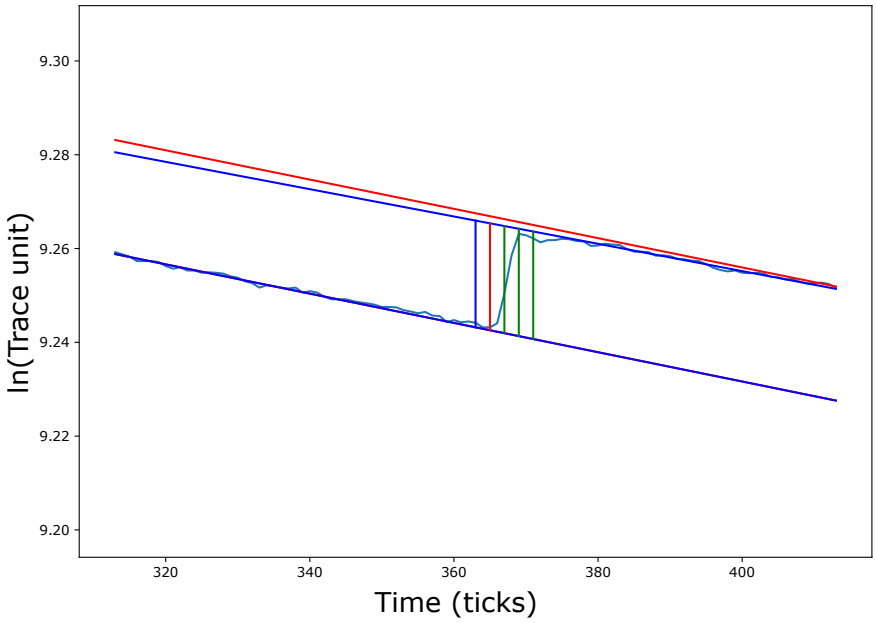

Figure 3.9: A trace which has been fitted with the gradient method. Both algorithms, fixed gradient shown in red and best fit shown in blue, show good agreement with one another. However, it is clear that the best fit approach is more accurate, and this was selected as the better fit. The drop was determined from the red vertical line at the start of the drop.

Some of the decays occurred too close to the edges of the trace and didn't have any pre- or post-decay data for a fit to be performed. The decay drop in these traces was determined by taking the difference between the maximum and minimum values within 20 ticks either side of the drop point (see Figure 3.11). The drop heights and decay times were written out to file for calibration (see section 3.7.2) and standard correlation analysis.

It is noted that the above set of methods was not the only one attempted in this work. A moving window deconvolution (MWD) method was also employed to assess whether it could yield either better estimates of the drop heights or of the decay times. The results from the MWD algorithm were similar to those yielded by the method above, but with poorer peak resolution and less accurate decay time estimation. It is thought that the energy resolution was worse because the MWD algorithm fits the small flat top of a peak to find the drop height, with a sample size of $\approx$20 values, whereas the gradient fitting method uses almost the entire trace. This larger sample size means the gradient method is less sensitive to the noise present in all the traces. It is thought that the timing resolution was worse because the MWD method uses a smoothing average function in order to be legible, and this smoothing average removes the sharp start of a trace present in the gradient method. Overall, it was decided that the set of methods using the whole trace was better in every regard compared with the MWD method.

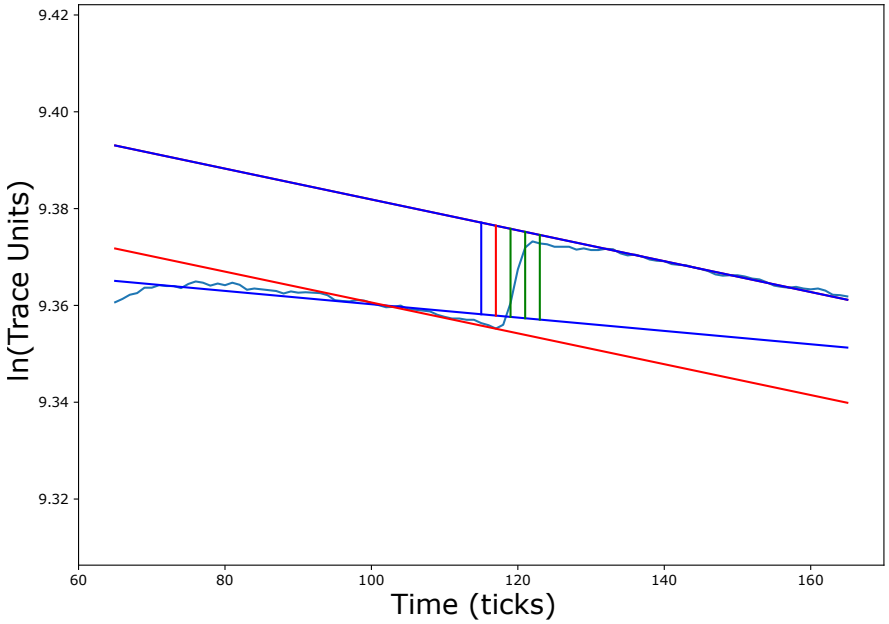

Figure 3.10: A trace which has been fitted with the gradient method. Both algorithms used are shown, fixed gradient shown in red and best fit to line shown in blue. It is clear that the best fit to both lines method is not an accurate representation of the trace drop, so the fixed gradient method was marked as the correct fit. The larger fitted section, in this case the side following the drop, was used to determine the gradient. This was then fixed and was fitted to the side before the drop. The difference between the y-intercept values is used to determine the drop height.

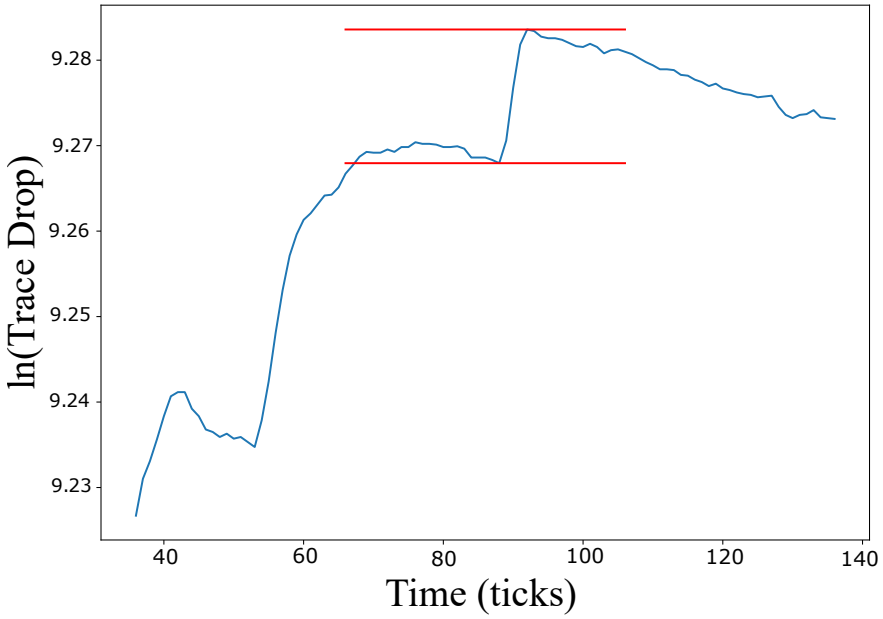

Figure 3.11: A trace which has been fitted with the maximum-minimum subtraction method. The drop itself is too close to the unfittable region below 85 ticks to make a reasonable assignment of drop height with the gradient method, and as such it's absolute height has been taken as its drop value.

3.7 Energy Calibration

There were two main energy calibrations performed in this work, each entirely separate. The first was the calibration of the trace energy units when reconstructing the energy of events whose decay was superimposed on a recoil trace (see section 3.6.2). The second was the calibration of the energy spectrum populated by events sorted by GRAIN, i.e. any event that was not seen in traces, but was recorded as a separate discrete event. It should be noted that the strips were individually gain-matched before both experiments using a three-line α source, and then calibrated during experiment using well-known α lines. This strip-by-strip calibration of the DSSD is usually applied by the 'gains' file required by GRAIN, and ensures that each strip shows the same energy for a known decay line. This means a calibration can be performed for the detector as a whole, as individual strip variations should not be present. During this work, the gains file was set such that it made no correction to event energies, and instead stripwise corrective factors were applied to raw DAQ channel numbers in the sort code. This was done to ensure event energies could be reproduced exactly because when GRAIN applies the gains it also applies a random smoothing correction of ± 10 keV. This is particularly important to avoid when determining the energy of new nuclides with very few counts. The time stamps on events remain unchanged, as these are hard coded in the run files.

3.7.1 Event Energy Calibration

The data used to calibrate the DSSD energy spectrum were taken from data sets A and B and sorted by two metrics; for each target, an energy spectrum was produced showing correlated decays that were preceded by a recoil implantation. Another energy spectrum was produced showing the same data, but with the additional condition that the decay happen within 50 ms of the recoil implantation.

To calibrate the energies observed in each experiment, the energy spectra were sliced into regions containing groups of well-defined peaks. The background was manually subtracted where necessary by modelling the escaping α particles expected in the region using simple linear interpolation. A Gaussian curve was fitted to peaks identified as known α decays using Python code, which can be found at Appendix 7.1. The fitting algorithm used was the SciPy ODR method. This uses a modified trust-region Levenberg-Marquardt-type algorithm [43], also known as the damped least-squares method, to estimate the function parameters. It was chosen because it can accept both x and y errors, allows a user-defined model equation for fitting to be defined and is easy to give starting parameters for very complex multi-Gaussian fits. The code outputs a centroid with uncertainty and a FWHM with uncertainty. The first set of calibration points was taken from a correlated α-decay spectrum produced from data set A with no minimum correlation time. The peaks are well separated from those of other radioactive decays and are well-known, which allowed a reasonably precise fit, as seen in Figure 3.12. The slight deviation of the fit at the low energy side is attributed

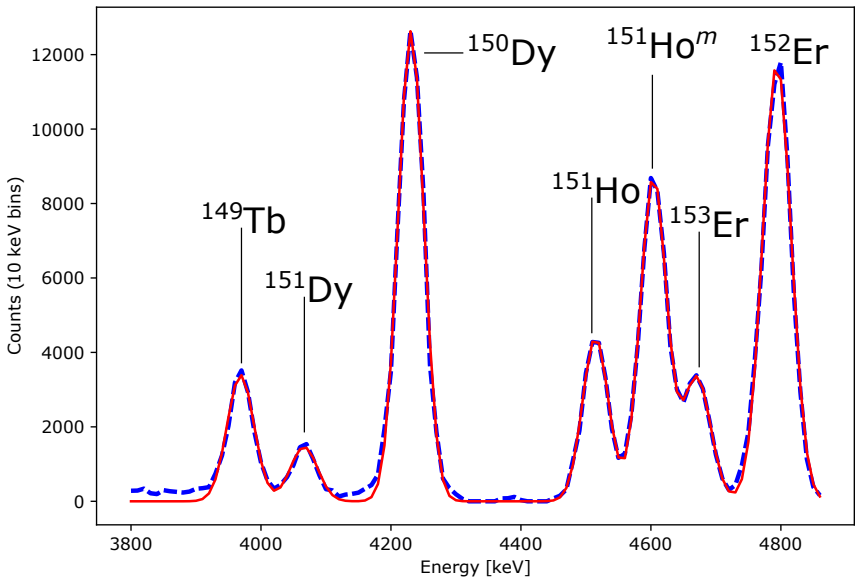

Figure 3.12: The Tb, Dy, Ho and Er peaks present in a correlated α-decay spectrum produced with data set A, shown in blue dashed line, with the plotted Gaussian fits overlaid, shown in red solid line. Calibration energies used and references are listed in Table 3.4.

to the simplicity of background subtraction. The second set of calibration points was taken from the main group of α-decay lines in a correlated α-decay spectrum produced with data set B and no minimum correlation time. This region was chosen because of the large number of events in the histogram and the nuclides present all have well-known α-particle energies. The fit agrees well with the data, as seen in Figure 3.13. The final set of calibration peaks was necessary to ensure the accuracy of the calibration at high energy. This region is where the α-particle energies for the α-emitting nuclei discovered in this work are expected to lie. In a correlated α-decay spectrum produced with data set A and a 50ms minimum correlation time, the ^{155}Lu^{m} and ^{156}Hg^{m} α-particle energies are very well separated and require no background subtraction. There is a slight deviation in the ^{155}Lu^{m} fit from the data at the peak edges and centroid, seen in Figure 3.14. This could be from the low number of counts present or an exponential term could be present both above and below the peak which was not included in the fit.

With the peaks identified, the best known literature value for each of the nuclides was found. Table 3.4 shows the values that were used in the calibration and their source. The centroids of the fitted Gaussian peaks with errors were plotted against their known literature values, and both a linear and quadratic fit were performed. The linear fit gave better agreement with the results, and Figure 3.15 shows the relationship between the centroid fits and the known values. It is noted at this point that this calibration is only valid for the range in which it is shown, and at no point was it extrapolated.

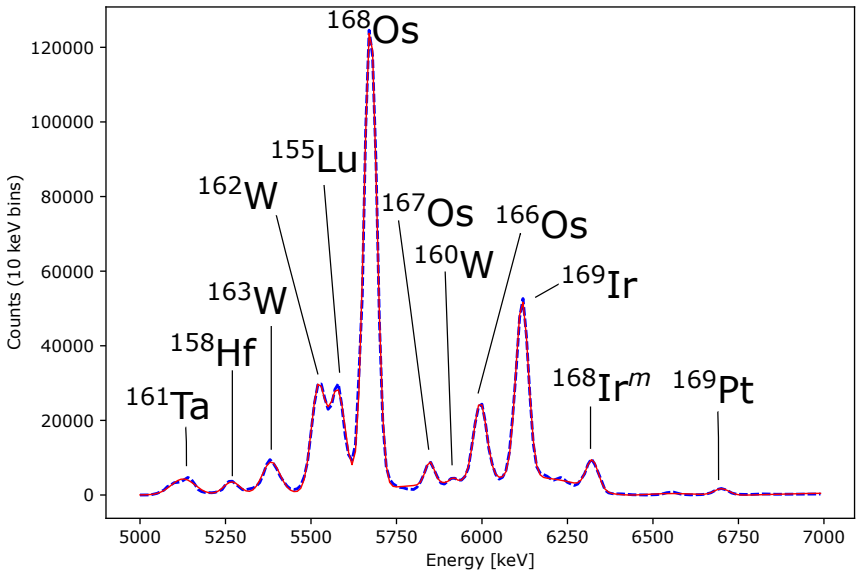

Figure 3.13: The main α peaks present in a correlated α-decay spectrum produced with data set B, shown in blue dashed line, with the plotted Gaussian fits overlaid, shown in red solid line. Calibration energies used and references are listed in Table 3.4.

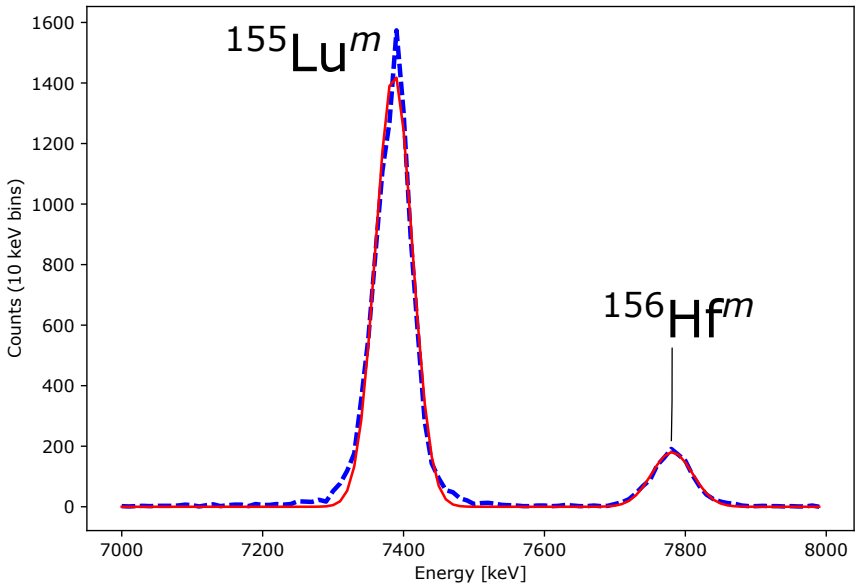

Figure 3.14: The $^{156}\mathrm{Hf}^{m}$ and $^{155}\mathrm{Lu}^{m}$ peaks present in a correlated α-decay spectrum produced with data set A, shown in blue dashed line, with the plotted Gaussian fits overlaid, shown in red solid line. Calibration energies used and references are listed in Table 3.4.

Table 3.4: The literature values for the α-decay energies used when calibrating the spectra. The values are separated left and right based on which data set they were used to calibrate.

Data set A			**Data set B**		
Isotope	Energy (keV)	Ref	Isotope	Energy (keV)	Ref
^{149}Tb	3967(3)	[44]	^{161}Ta	5148(5)	[44]
^{151}Dy	4069(3)	[44]	^{158}Hf	5269(4)	[6]
^{150}Dy	4236(2)	[44]	^{163}W	5384(2)	[44]
^{151}Ho	4521(3)	[44]	^{162}W	5534(3)	[44]
^{151}Ho^{m}	4607(3)	[44]	^{155}Lu	5578(4)	[45]
^{153}Er	4676(2)	[44]	^{168}Os	5676(4)	[44]
^{152}Er	4804(2)	[44]	^{167}Os	5836(2)	[44]
^{155}Lu^{m}	7390(5)	[6]	^{160}W	5912(5)	[6]
^{156}Hf^{m}	7782(4)	[6]	^{166}Os	6000(6)	[6]
			^{169}Ir	6126(5)	[44]
			^{168}Ir^{m}	6323(8)	[6]
			^{169}Pt	6678(15)	[46]

The energies given by GRAIN (see section 3.5) were then adjusted according to the linear calibration. The calibration error that was used in the uncertainty calculation (Equation 3.17) used the errors on the fitted line from Figure 3.15. The same code used to generate these values was also used to generate the stripwise gain corrections for the data set C, using many of the same peaks.

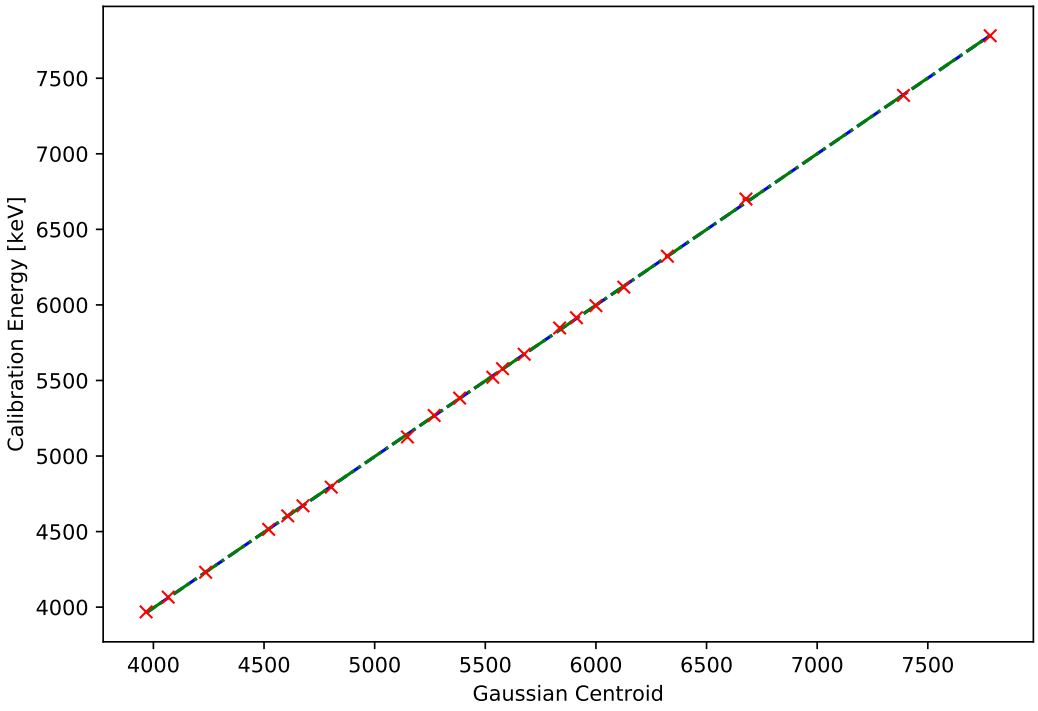

Figure 3.15: The linear (blue) and two-dimensional polynomial (green) lines of best fit on a plot of Gaussian centroids produced by the code versus known α energies of identified nuclides. Error bars are present on the graph, but may be too small to see easily. In fact, the lines themselves are so similar is is difficult to distinguish them. This calibration is valid only in the calibrated range and is not extrapolated at any point.

3.7.2 Trace energy calibration

Calibration of the trace energy units posed one of the largest challenges in this work as there were not many calibration data available. There are few nuclides with short enough half-lives or high enough production yields to be seen in traces produced in this work. This calibration was necessary because the algorithm the DAQ uses to calculate energy values from voltage pulses, i.e. the FPGA setup of the Lyrtech ADC, was not available to the author. An attempt was made to discern this algorithm by calculating energy values from the traces of known-energy α-decay events and comparing them against the energy given by GRAIN. Results from this study proved inconclusive as the DAQ algorithm gave clearly different results from each of the test case algorithms. Additionally, it is thought that the DAQ algorithm requires a full voltage pulse trace (from baseline to baseline), and the traces available from the data are only 5 µs long. It is possible that the remainder of each trace could have been simulated, but this would have introduced further imprecision to the final values. Therefore, extraction of energy values from traces required the two calibrations described in this chapter.

In total, 215 traces were produced in the L04 experiment that met the criteria for a calibration grade trace including those attributed to the new nuclides ^{169}Au and ^{165}Ir. The traces were separated into 4 categories: Those from the data set A, either with at least one α-decay-like event following the recoil or with no correlation, and those from the data set B, also either α-correlated or uncorrelated. There were 25 uncorrelated and 83 correlated traces from the ^{96}Ru target data and 57 uncorrelated and 50 correlated traces from the ^{92}Mo target data. The drop heights in trace y units, determined according to Section 3.6.2, can be seen in Figure 3.16.

There were two peaks in the correlated ^{96}Ru data, one in the uncorrelated ^{96}Ru data, three in the correlated ^{92}Mo and two in the uncorrelated ^{92}Mo data that were from identifiable decays.

In the ^{96}Ru correlated data, the lower-energy peak around 200 trace units is clear without any gating. This peak was attributed to the proton decay of ^{169}Au^{m} (see Chapter 4). There is also a wider peak around 720 trace units which was attributed to ^{169}Pt after correlating with daughter decay chains. Approximately 20,000 counts of ^{169}Pt were produced in data set B and its half-life of 6.99 ms is sufficiently short for some decays to be expected to occur within the 5 µs wide traces. The peak in the uncorrelated ^{96}Ru data around 670 trace units was assigned to ^{169}Ir. Approximately 100,000 counts were produced in data set B, so despite its long half-life of 640 ms, some decays are expected to occur in traces. Its decay chain is dominated by beta emission, so it being uncorrelated lends further support to this assignment.

The two lower-energy peaks in the ^{92}Mo target correlated data were assigned to the ground and isomeric state proton decays of ^{165}Ir (see Chapter 4). Approximately 1100 proton decays of the isomeric state were identified in event data, and its half-life of 0.3 ms is sufficiently short for decays to be expected within the traces. In the uncorrelated ^{92}Mo target data, the peaks around 800 and 850 trace units are assigned to

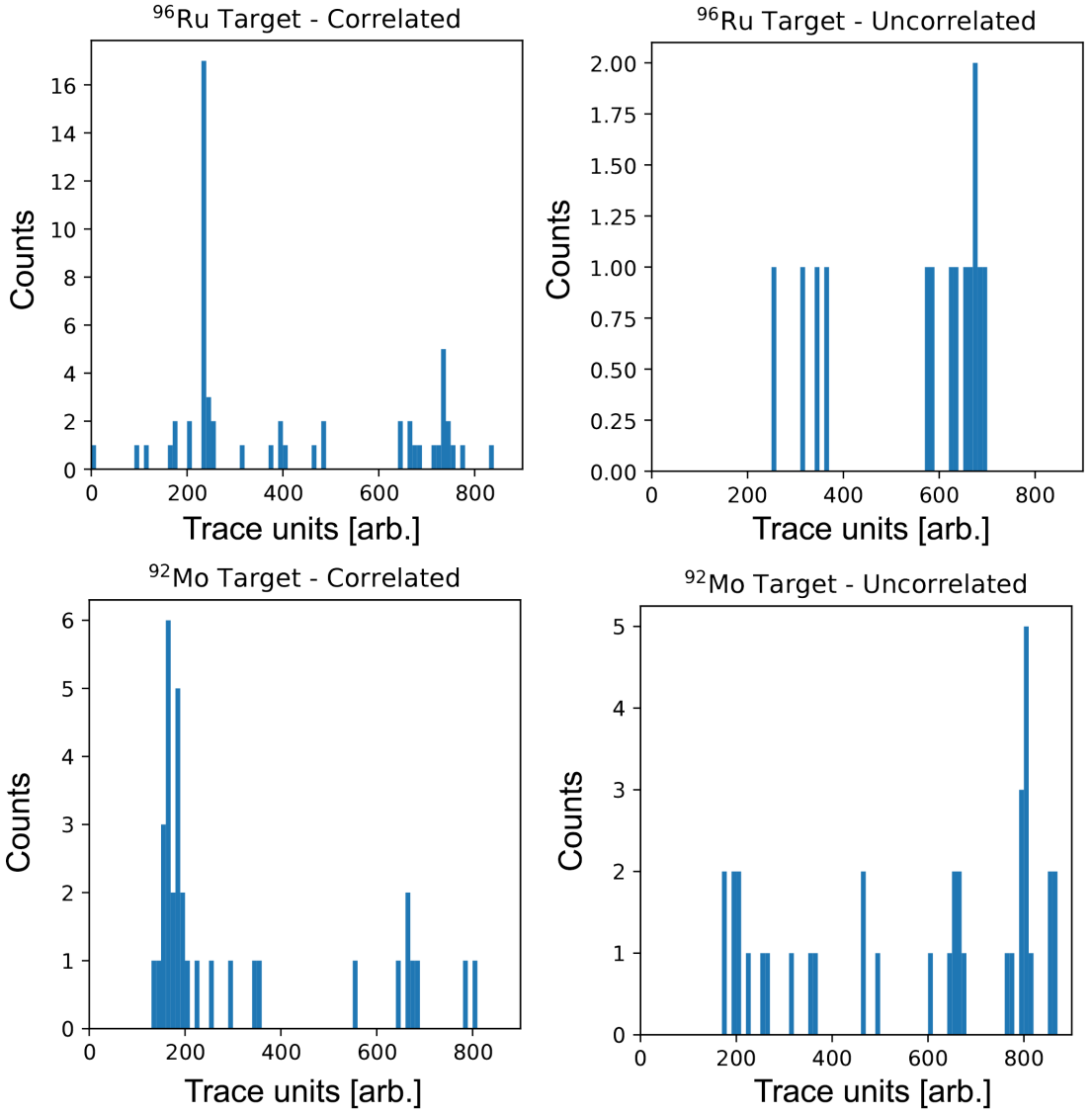

Figure 3.16: The determined drop heights of each of the trace decays in trace y units. The data are represented in four plots because they have different origins. The targets used to produce the data are labelled on each plot, as well as whether it was followed by correlated α-decays or not (correlated or uncorrelated).

$^{155}Lu^{m}$ (≈9,600 produced) and $^{156}Hf^{m}$ (≈1,350 produced), both of which are expected to be uncorrelated, lending further credence to these assignments.

In order to check these assignments, the first step performed was standard correlation analysis, the selection of the trace drops based on known daughter, granddaughter and great-granddaughter energies. The energies of events following the correlated traces were plotted in histograms to identify any chains that could allow assignment of a mother nuclide. The energy spectra of the correlated trace chains can be seen in Figure 3.17. The clearest identifications were the chains coming from $^{169}Au^{m}$ and ^{165}Ir, both showing multiple full chain correlations. The proton decays from ^{169}Au could not act as calibration points as they constitute the first observation of the nuclide, and the ^{165}Ir data were very carefully selected so no ground-state proton decays were included. The chains following ^{169}Pt showed clear correlation with α energies of ^{165}Os, ^{161}W and ^{157}Hf, supporting its assignment. The last possible calibration point from correlated traces was the decay at ≈650, which was tentatively assigned as ^{165}Os, but the chains are not particularly well defined. As such it was not used as a calibration point.

A preliminary rough calibration using just the ^{169}Pt and ^{165}Ir trace unit peaks supported the assignments of peaks to the decays from ^{169}Ir and the isomeric states of ^{155}Lu and ^{156}Hf, so they were used in the more rigorous final calibration. It was decided by the author that more data were necessary in the proton region of the calibration. If the $^{165}Ir^{m}$ data were to be used alone, an error sensitive fitting algorithm would not fit the point closely due to its large trace units centroid error. This would subject the entire proton region to a 'lever arm' effect where the fit would match the α region as accurately as possible. The small resulting gradient difference, when centred in the α region, would have a disproportionately large effect on the y-intercept and make the fit quality in the proton region worse. Therefore, other proton decays were identified in event data and used to cross-calibrate trace data. To do this, a calibration was performed for all nuclides observed in both trace and event data, plotting trace drop heights against energy peak centroids from event data. Decays from ^{169}Ir and isomeric states $^{155}Lu^{m}$ and $^{156}Hf^{m}$ were already fitted in the event calibration section (3.7.1), so ^{169}Pt and ^{165}Ir were fitted individually. The results of the fits used to determine the event peak centroids can be seen in Figure 3.18. A linear fit was performed, and an equation was obtained that would convert event data into trace drop heights with associated errors. This calibration makes the assumption that the energy responses of the detector and electronics are linear, and that the multiple preamplifiers of the same make and model used all have the same energy response.

As event data could now be used to cross-calibrate trace data, data sets A and B were searched for proton emitters not present in traces to calibrate the low energy region. Selection was possible by requiring subsequent decays to match known α-decay energies and for all decays occur within triple their reported half-lives. Proton decays from ground states of $^{170,171}Au$ and the isomeric states of ^{159}Re, $^{164,165}Ir$ and $^{170,171}Au$ were identified in statistically significant quantities. Chains containing at least

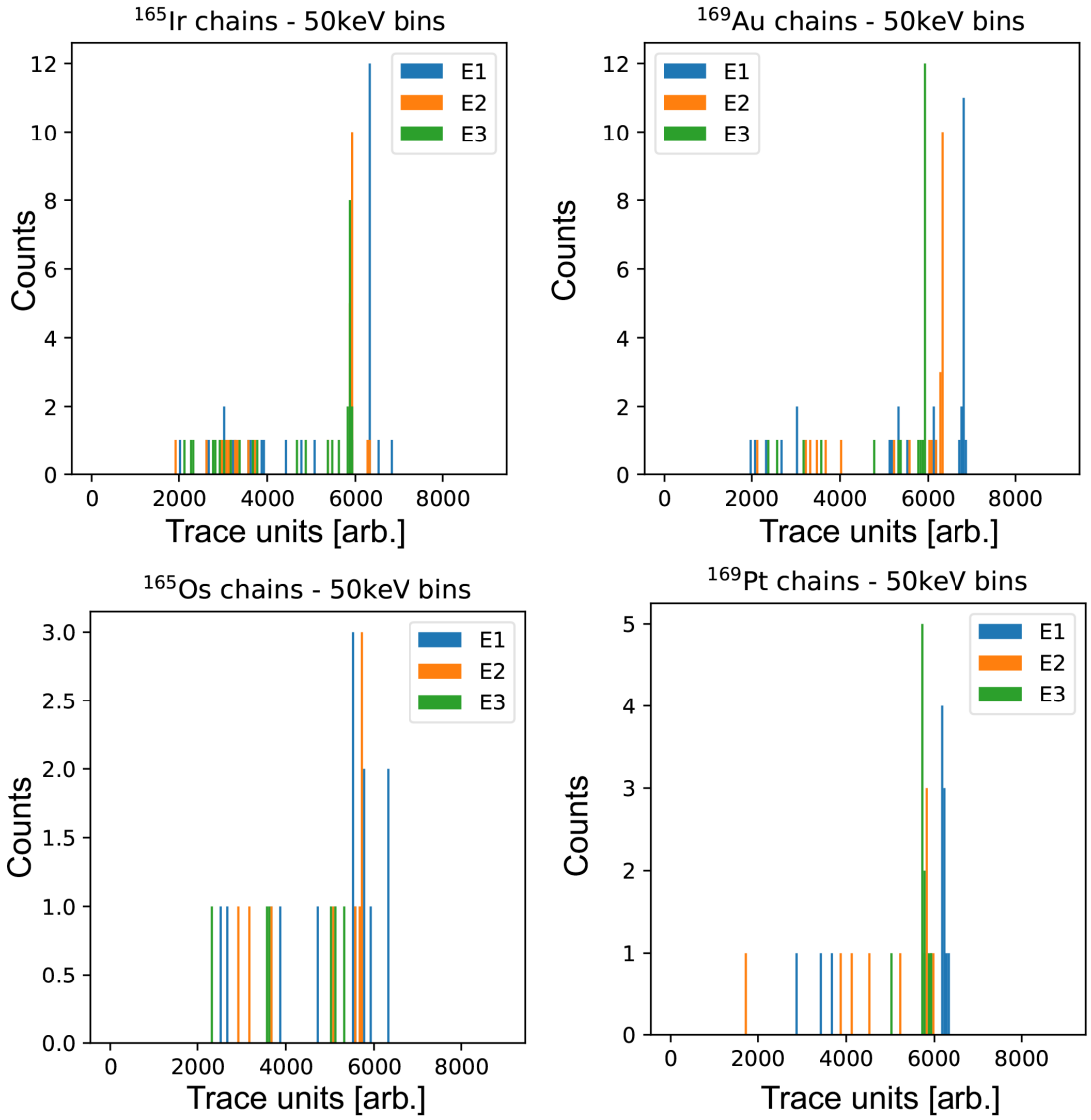

Figure 3.17: The daughter (E1), granddaughter (E2) and great-granddaughter (E3) α-decay energies following traces. Each set is assigned to an assumed parent based on the decay chain seen in the histogram.

Table 3.5: Corrected pulse height values used for trace calibration. In each case, the error on the corrected value was taken as the error on the original literature value.

Nuclide	Ground State (keV)		Isomeric State (keV)	
	Literature Values	Corrected Values	Literature Values	Corrected Values
^{170}Au	1463(12) [11]	1465.90	1743(6) [11]	1743.50
^{171}Au	—	—	1694(6) [11]	1695.56
^{165}Ir	—	—	1707(7) [5]	1710.70
^{164}Ir	—	—	1814(6) [8]	1818.47
^{169}Ir	—	—	6126(5) [44]	6238.45
^{169}Pt	6678(15) [46]	6798.74	—	—
^{155}Lu	—	—	7390(5) [6]	7525.69
^{156}Hf	—	—	7782(4) [6]	7925.09

2 full energy α-decay daughters were printed out from GRAIN, transformed into cross-calibrated trace data, loaded into the Python code alongside the experimental data and used as calibration points. This did exclude ^{159}Re from use as a calibration point as its decay chain does not contain 2 α-decays to correlate with. Additionally, only one chain from the ground state of ^{171}Au contained two full energy α-decay daughters, so this single count was not used for calibration. Uncertainties were determined from the width and population of the peaks in the event data combined with the uncertainty associated with the cross-calibration using equation 3.17.

The addition of the cross-calibrated data meant enough trace drop height data was available to perform a calibration that would be accurate in the proton energy region. The known α- and proton-decay energies from literature were corrected for the contribution to the energy signal from the daughter nuclei recoiling within the DSSD [47, 48]. Corrections were made for the pulse height defects and for the non-linear response of silicon detectors to low-Z ions [49]. The literature values and corrected values used can be seen in Table 3.5. It is noted that the corrections can be much larger for α-particles than protons due to their much larger mass and energy.

For the final calibration, only counts which were correlated with at least two full-energy α-decay daughters were used. This meant that decays from ^{169}Ir and the isomeric states ^{155}Lu^m and ^{156}Hf^m were not used as they could not be verified on a countwise basis. The trace drop centroids were plotted against the corrected decay energies and both a linear and quadratic fit were performed. The fitting algorithm used was the SciPy ODR method. The resulting fit was linear and can be seen in Figure 3.19.

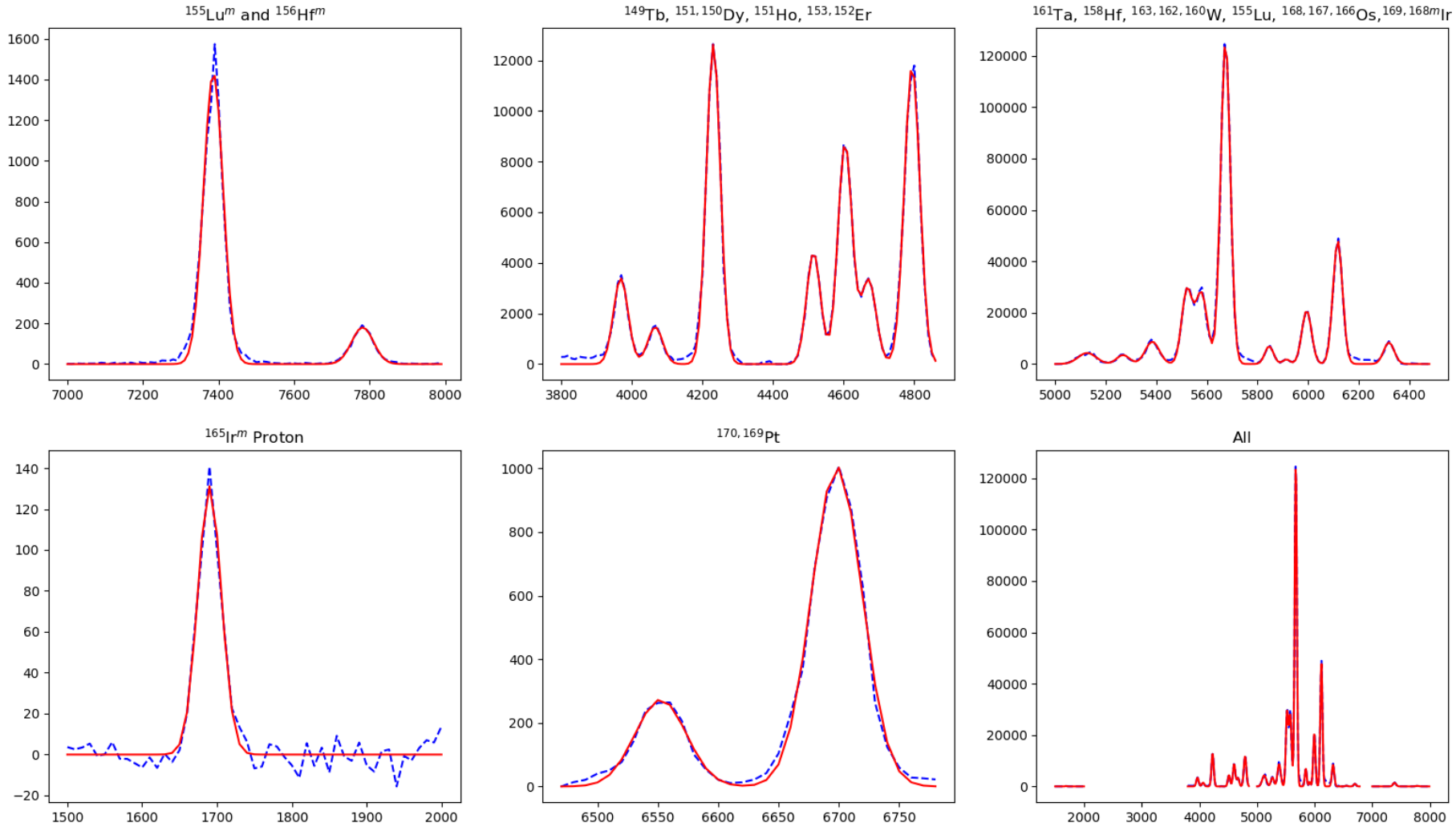

Figure 3.18: The results of fitting known α- and proton-energy centroids in event data to determine their centroids for calibration. All x-axes show Energy in keV and all y-axes show number of counts per bin.

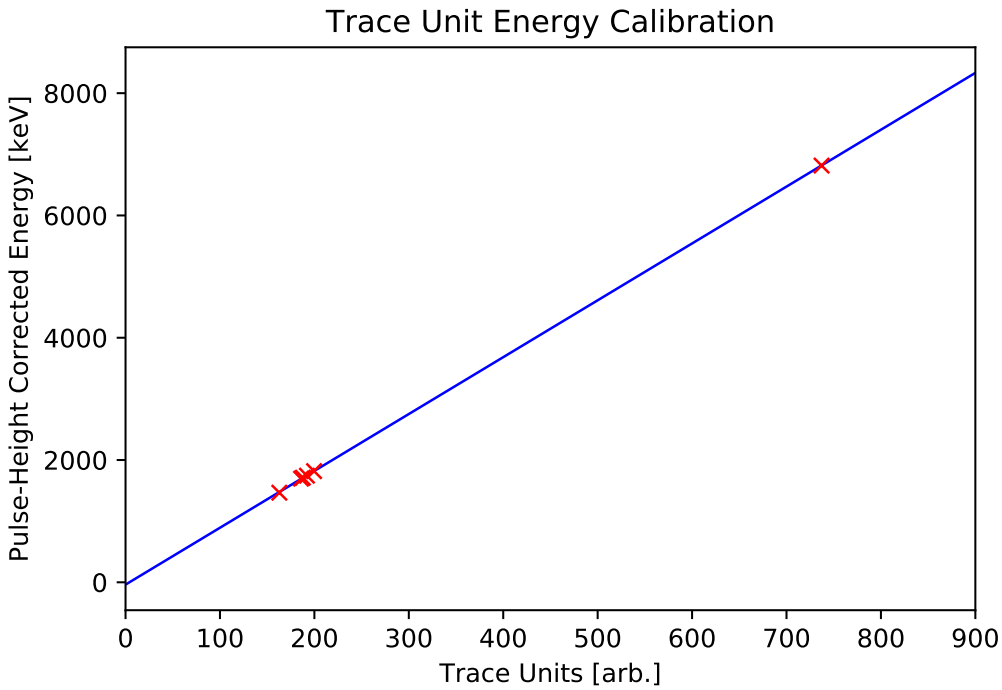

Figure 3.19: The calibration line used to convert trace units into keV energy values. This plot has the trace drop centroids of $^{164}\mathrm{Ir}^{m}$, $^{165}\mathrm{Ir}^{m}$, $^{170}\mathrm{Au}^{g,m}$ and $^{171}\mathrm{Au}^{g,m}$ and $^{169}\mathrm{Pt}$ plotted against their respective pulse height corrected known literature energy values, which are listed in Table 3.5. The vertical error bars are too small to see in most cases, and the horizontal bars are not capped, just horizontal bars.

3.8 Value Determination and Error Handling

When defining any value in this work, wherever possible and relevant, an associated uncertainty has also been quoted alongside it. This section will detail all the main formulae and methodologies used to determine both the values themselves and their uncertainty.

3.8.1 Energy Values and Errors

When detecting multiple instances of a radioactive decay, the spread of energies seen is a Poisson distribution if the detector is functioning properly. This occurs because the charge collected from a detector is rarely perfectly proportional to what was generated in the material. While the Gaussian shape can be wider in some detectors than others, for a given detector the error on any individual event is the same. The final energy value of a set of measured energies is the arithmetic mean of all the energies, and the base uncertainty is $\sqrt{N}$, the square root of the number of events in the set.

When dealing with low numbers of observed events, it is important to make sure that the error quoted reflects both the uncertainty from a lack of statistics as well as the error that comes from the equipment used and its technical limitations. The uncertainty on any given α-decay energy with more than 10 counts was given by

$$\delta E_\alpha = \sqrt{\left(\frac{FWHM}{2\sqrt{2\ln 2}\cdot\sqrt{N}}\right)^2 + (\delta E_{Calib})^2}, \tag{3.17}$$

where the FWHM is the full-width of the peak at half of its maximum height, and is related to the standard deviation of the set σ by $FWHM = 2\sqrt{2\ln 2}\cdot\sigma$ and δE_{Calib} is the energy error associated with the calibration. In some cases throughout this work, fewer than 10 events were observed for a given nuclide. Equation 3.17 was still used to calculate the decay energy uncertainty but rather than determine the FWHM from the observed energies, a FWHM value that would be typical in that energy region was used. It was assumed, based on the α energy calibration covered in section 3.7, that FWHM increased linearly with increasing α energy. This avoids artificially narrowing or widening the peak of any observed events. It is equally likely, on the scale of fewer than 10 events, that the observed counts could come from opposite ends of a Gaussian peak, or that they could be close in energy despite not representing the real centroid. There is no way to determine any meaningful information about the peak from so few events, so the typical FWHM values used better estimate the width of the real peak.

When a particle is detected, the energy observed is sometimes not the true energy the particle had upon emission. The largest loss of energy occurs when a particle does not deposit all of its energy in the detector. This is referred to as an 'escape', and happens when the particle physically leaves the sensitive area of detector. Any implanted nucleus has a probability of emitting radiation that escapes. The probability varies as a function of implantation depth Z and average emitted particle range in

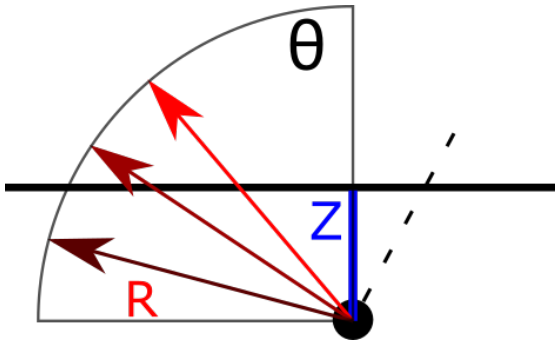

Figure 3.20: A diagram showing the relationship between implantation depth Z, average path length R and angle of emission θ. The solid black horizontal line represents the detector surface and the dashed black line the recoil implanting in the detector.

material R (see Figure 3.20). The solid angle cone where an escape is possible can be easily defined. Spherical emission means that the full solid angle is 4π, but assuming the detector is sufficiently thick that escape from the back is unlikely then the solid angle of the hemisphere facing the surface of the detector is 2π. Emitted particles would be absorbed at extreme emission angles approaching parallel to the surface, so the formula is dependent on the angle of emission relative to the plane of the detector. The angle where an escape is possible will be

$$2\pi(1-\cos\theta) = 2\pi\left(1-\frac{Z}{R}\right).$$

This makes the full capture efficiency, i.e. the efficiency of an event not being emitted at an angle where it could escape

$$\epsilon = \frac{4\pi - 2\pi(1-\frac{Z}{R})}{4\pi} = \frac{1}{2}\left(1+\frac{Z}{R}\right).$$

A full-energy signal may not be observed if the energy of a particle is deposited in > 1 pixel. If a recoil implants into the detector close to the edge of a pixel, particles with an emission angle approximately in the plane of the detector can escape to the next pixel. Therefore, there is a region around the edge of a pixel where such escapes are possible, which for smaller pixel sizes represent a larger percentage of the pixel area. This pixel escape efficiency is non-trivial to model because of the non-uniformity of the electric field at the strip edges and the charge collection mechanism of electrons and holes moving through detector material.

The collection of charge in the DSSD will cause a partial energy signal to be observed. Recombination of electron-hole pairs means charge carriers are lost, the liberation of the electrons themselves requires some small amount of energy and heavy charged particles begin to capture electrons at very low energies. Additionally, when a heavy charged particle cannot liberate an electron, the nuclear scattering effect becomes more dominant and more energy is lost to scattering reactions with nuclei. These

systematic effects are usually uniform and can be accounted for with calibration, but as with any random process, some peak broadening always occurs.

The uncertainties for decay energies in the work from traces were calculated differently. The fit line seen in Figure 3.19 is weighted by α decays despite the inclusion of cross-calibrated data, and as such the errors on the gradient and y-intercept given by the fitting program will be proportionally higher in the proton energy region. The gradient was therefore assumed to be "anchored" on the $^{165}\mathrm{Ir}^{m}$ proton decay. This made the error term contributed by the fit more realistic, as the original numbers valid over the full range would have overestimated the error in the low energy region. The specific combination of errors was

$$\Delta_{Au,Ir} = \sqrt{\left(\Delta m \cdot |x^{Cen}_{^{A}X} - x^{Cen}_{^{165}Ir^{m}}|\right)^2 + \Delta y^2_{^{165}Ir^{m}} + \left(\frac{\sigma_{^{A}X}}{N_{^{A}x}} \cdot m\right)^2 + \left(\frac{\sigma_{^{165}Ir^{m}}}{N_{^{165}Ir^{m}}} \cdot m\right)^2}, \tag{3.18}$$

where x^{Cen} is the centroid of a curve fitted over the raw trace drop peak of nucleus ^{A}X pre-calibration, Δy is the error on the literature value of a decay energy, m is the gradient of the calibration line with uncertainty Δm and σ is the standard deviation of the Gaussian fit used to get x^{Cen} from a set of trace drops.

3.8.2 Half-Lives and Uncertainties

The best approximation of the lifetime τ of a nuclide, when a large set of decay times is available, is the arithmetic mean of the individual decay times s. The error is then given by $\sqrt{\tau^2/N}$ when the searching time T (the time the equipment is sensitive to decays) is much longer than the lifetime of the decaying species and N is the number of counts. In this work, however, the searching time T was often finite and short. As such, the half-lives in this work were determined by the method outlined in the work by Rudolf Peierls [50], where half-life is dependent on the searching time T in addition to the average of the decay lifetimes s. If a nuclide has a half-life of 5 µs and the equipment is only sensitive for 5 µs, then it follows that some percentage of the decays will occur when the equipment is not sensitive. The corrective factor applied to account for this is determined by

$$\tau - s = \frac{T}{e^{T/\tau} - 1}. \tag{3.19}$$

An easy way of showing this relationship is to tabulate values of T/τ, T/s and τ/s in the range where the corrective factor is the largest (when $T/s \approx$ 2-8) [50]. These values were plotted as a graph and a line was drawn from point to point so that any value of s could be corrected. The half-lives of decays with short T compared with s are given by

$$\ln(2) \cdot \frac{T}{m_{pp} \cdot \frac{T}{s} + c_{pp}} \tag{3.20}$$

where m_{pp} and c_{pp} are the gradient and y-intercept of the line joining the two tabulated points on a plot of T/s versus T/τ that the value of T/s lies between for given values of

T and s. This correction was most necessary for nuclei observed in preamplifier traces, for which $T = 5\,\mu s$. This graphical method was found to break down when calculating upper and lower bounds for values with low T/s values, so the final calculations were done using a Fortran code incorporating the maximum-likelihood methods described in reference [51]. The mathematical basis for the Meyer method is the same as that of Peierls, but the way it is handled allows for better results at extreme T/s values where T approaches s.

The uncertainty on the half-lives of non-trace data are calculated with the following asymmetric formulae for the upper and lower mean lifetimes,

$$\tau_u \approx \frac{t_{1/2}}{1 - \frac{z}{\sqrt{N}}}; \qquad \tau_l \approx \frac{t_{1/2}}{1 + \frac{z}{\sqrt{N}}}, \tag{3.21}$$

where z is the confidence level and τ_u and τ_l are the upper and lower limits of the mean lifetime τ. To calculate the quoted asymmetric errors, the following formula is used: $\tau^{+(\tau_u - \tau)}_{-(\tau - \tau_l)}$. Usually z = 1, which corresponds to a 1σ confidence level. There are 2 exceptional cases for N when there are only one or two counts. These cases see a breakdown in the formula, so the mean lifetime limits are obtained by multiplying by the values in table 3.6. The actual positive and negative uncertainties are the difference between the mean lifetime and the limits in each direction.

Table 3.6: The error limits for half-lives when n $\leq$ 2.

Number of Counts	Lower Error Limit τ_l	Upper Error Limit τ_u
1	0.543	5.79
2	0.606	2.82

The minimum resolvable decay time from a trace decay, i.e the shortest time after recoil implantation at which it is possible to reconstruct the energy of superimposed event, is 85 ticks, so when calculating half-lives from trace decays, 0.85 μs are subtracted from each value before the decay constant is calculated to give a physical value.

Maximum-Likelihood Estimates of Half-Lives

Considering many of the observations of nuclides in this work comprise very few individual events, it is pertinent to have some means to determine whether observed events belong to a single radioactive decay or to more than one. The determination method used in this work was first outlined by Schmidt [52]. The natural logarithm of the individual decay times $\ln(t) = \Theta$ is taken and they are sorted into a histogram where bin size Δt varies with $\Delta t/t = const.$ The corresponding decay distribution, an asymmetric bell shape, is the same for all nuclides and independent of the decay constant λ. The amplitude of the distribution varies with N, and the standard deviation of the ideal

curve $\sigma_{\Theta_{th}} \approx 1.28$. The ideal distribution is described by

$$\left|\frac{\mathrm{d}N}{\mathrm{d}\theta}\right| = Ne^{(\theta+\ln\lambda)}e^{(-e^{(\theta+\ln\lambda)})}. \tag{3.22}$$

The experimental standard deviation is calculated with the following equation:

$$\sigma_{\Theta_{exp}} = \sqrt{\frac{\sum_{i=1}^{N}(\theta_i - \bar{\theta}_{exp})^2}{N}} \qquad \bar{\theta}_{exp} = \frac{\sum_{i=0}^{N}\theta_i}{N} \tag{3.23}$$

The expectation value can be calculated to give the upper and lower limits of acceptable values of $\sigma_{\theta_{exp}}$ for different values of N [52]. If $\sigma_{\theta_{exp}}$ is outside these limits, it is likely that the decays in the population belong to more than one nuclear species. Broadly, the limits are $1.28 \pm {}^{2.15}/_{\sqrt{n}}$.

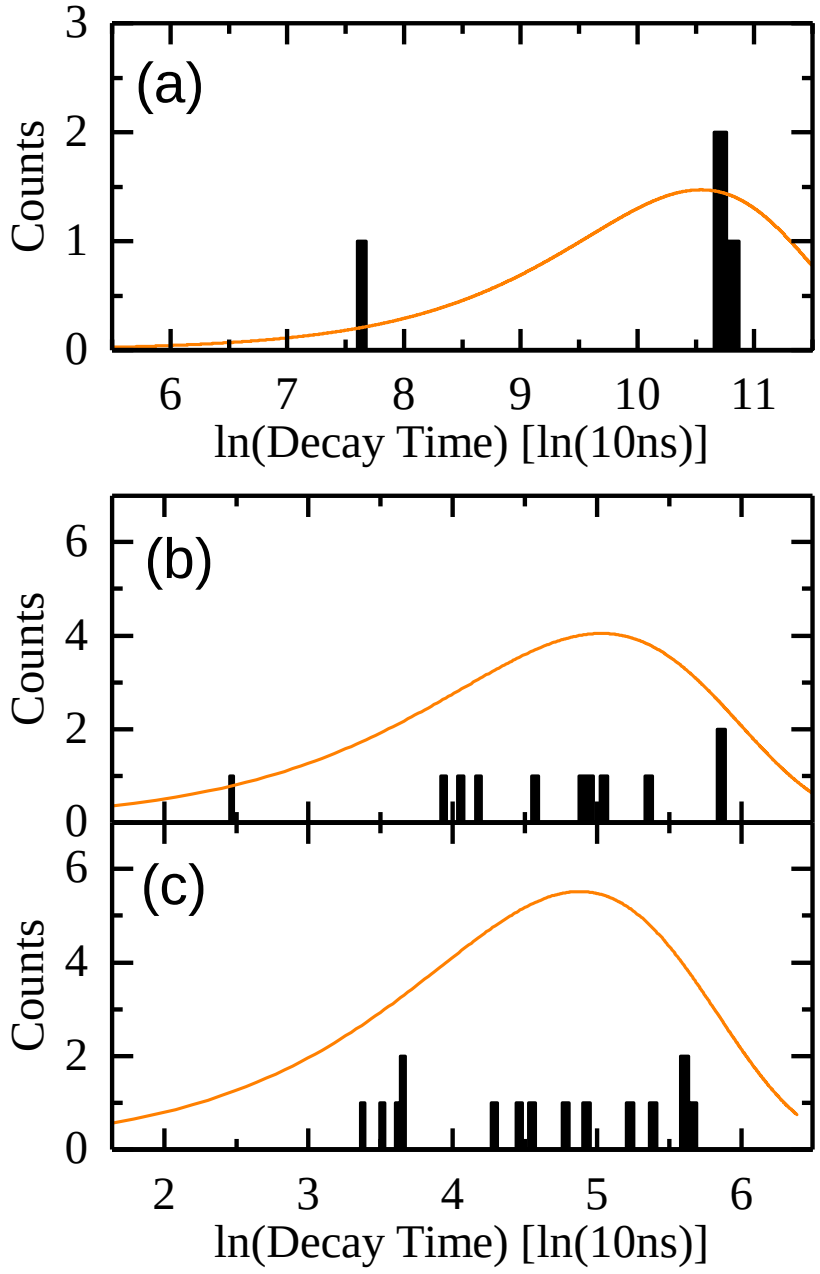

Figure 3.21: Histograms of the natural logarithm of the decay times in 10ns units (ticks), plotted on the same axis as the ideal distribution for a single source decay (drawn in orange) for (a) ^{165}Pt, (b) ^{169}Au and (c) ^{165}Ir. Their $\sigma_{\Theta_{exp}}$ values are (a) 1.35, (b) 1.09 and (c) 0.82.

Chapter 4

Proton emission from ^{169}Au and ^{165}Ir

This work presents the discovery of proton emission from the $\pi s_{1/2}$ ground state of ^{165}Ir and from the $\pi h_{11/2}$ isomer of new nuclide ^{169}Au. These results are covered already in the author's paper on the subject [2]. Heavy-ion fusion-evaporation reactions of ^{78}Kr(^{96}Ru,1p4n)^{174}Hg* and ^{78}Kr(^{92}Mo,1p4n)^{170}Pt* were used to produce ^{169}Au and ^{165}Ir, respectively and were separated using the MARA vacuum-mode mass separator. The proton emission energies and half-lives have been measured for the first time for decays from the isomeric state of ^{169}Au and the ground state of ^{165}Ir. Also measured for the first time are the energy and half-life of the α decay from the isomeric state of ^{169}Au. This marks the lightest nuclide relative to its lightest stable isotope ever discovered, with ^{169}Au being 28 neutrons lighter than ^{197}Au.

4.1 Motivation

Studies of proton radioactivity provide spectroscopic information on low-lying states at the boundaries of observable nuclei [17]. Proton emission can be viewed as a simple radioactive decay mode in which a proton tunnels through the potential barrier arising from the Coulomb and centrifugal components of the nuclear potential. For light elements, this barrier is comparatively small so that proton-unbound nuclei can decay with very short half-lives ($t_{1/2}$ $\leq$10 ns), allowing the emitted protons to be measured using detectors placed around the production target and selected through coincidences with the daughter species identified at the focal plane of an in-flight separator [53, 54]. For heavier elements, the higher Coulomb barrier can lead to longer half-lives ($t_{1/2}$ $\sim$100 ns) such that decays occur beyond the target region, but before the nuclei reach the separator's focal plane. In some cases, the reduced yields observed in focal plane spectrometers compared with those expected from the smoothly varying production cross sections have been assumed to be the result of in-flight proton emission. From these reductions, half-lives, proton-decay Q values and nuclear structure

information have been inferred [55, 56]. However, without directly observing the emitted protons, the possibility that nuclear structure effects could instead be responsible for reduced production cross sections cannot be completely excluded [57].

In contrast, over 40 cases of proton emission have been measured directly from low-lying states in nuclei with $Z > 50$. This has been possible because the potential barriers are sufficiently large compared with the proton-decay Q values that the half-lives are $\geq$1 μs. This allows the nuclei to be transported to a spectrometer situated at the focal plane of a recoil separator, where their decays can be studied. An important feature of proton emission that has been exploited in these experiments is the sensitivity of the half-lives to the orbital angular momentum quantum number l of the emitted proton, whereby increasing l by $1\hbar$ can increase the proton-decay half-life by an order of magnitude. This is a stronger effect than in α-decay, because for heavy nuclei the centrifugal barrier is approximately 4 times larger for proton emission than for α-particle emission for a given value of l. Figure 4.1 shows how half-lives for proton emission from states in odd-Z elements between $_{69}$Tm and $_{81}$Tl vary as a function of the Coulomb parameter, $\chi = 2(Z-1)e^2/(4\pi\epsilon_0\hbar v)$, where $v = \sqrt{(2Q_p/\mu)}$ is the speed of the emitted proton and μ is the reduced mass of the proton-daughter nucleus system [58]. The parameter χ reflects the relative magnitudes of the Coulomb barrier and the Q value, allowing data spanning a range of elements to be compared with each other. It can be seen that on a logarithmic scale the half-life data follow separate linear trends for proton emission from the $s_{1/2}$, $d_{3/2}$ and $h_{11/2}$ orbitals, reflecting the effect of the centrifugal barrier for the different values of l.

One consequence of this is that for several nuclides at the neutron-deficient boundary of the nuclear landscape, proton emission has only been observed from the $\pi h_{11/2}$ orbital because the half-lives for the lower-l orbitals are probably too short for the nuclei to survive the flight time through a recoil separator. The lightest known iridium isotopes, ^{164,165}Ir, are typical examples where proton and α-particle emission from their $\pi h_{11/2}$ isomeric states have been reported, but no decays of the expected lower-spin ground states were observed [5, 11, 8].

Prior to this work, the lightest known isotope of gold was ^{170}Au, both states of which were studied by Kettunen *et al.* [11]. They measured the proton energies to be $E_p = 1743(6)$ and $1463(11)$ keV and the half-lives to be $T_{1/2} = 590^{+70}_{-60}$ and 283^{+50}_{-40} μs for ^{170}Au^m and ^{170}Au^g, respectively. The lightest known isotope of iridium is ^{164}Ir, but this work will focus on the proton decay from the unobserved ground state of ^{165}Ir. The isomeric state of ^{165}Ir was studied by Davids *et al.* [5], who reported $E_p = 1707(7)$ keV and $E_\alpha = 6715(7)$ keV with mean half-life $T_{\frac{1}{2}} = 0.30(6)$ ms. The isomeric state of ^{164}Ir was studied by Drummond *et al.* [8], who reported $E_p = 1814(6)$ keV and $E_\alpha = 6880(10)$ keV with half-lives of $70(10)$ μs and 69^{+41}_{-29} μs, respectively. Drummond *et al.* also reported an improved half-life for ^{165}Ir^m of $340(40)$ μs. Their data were searched for evidence of ground state decays from both ^{165}Ir and ^{164}Ir but neither was identified. Proton emission is common among odd-Z nuclei in this region, with most nuclei having

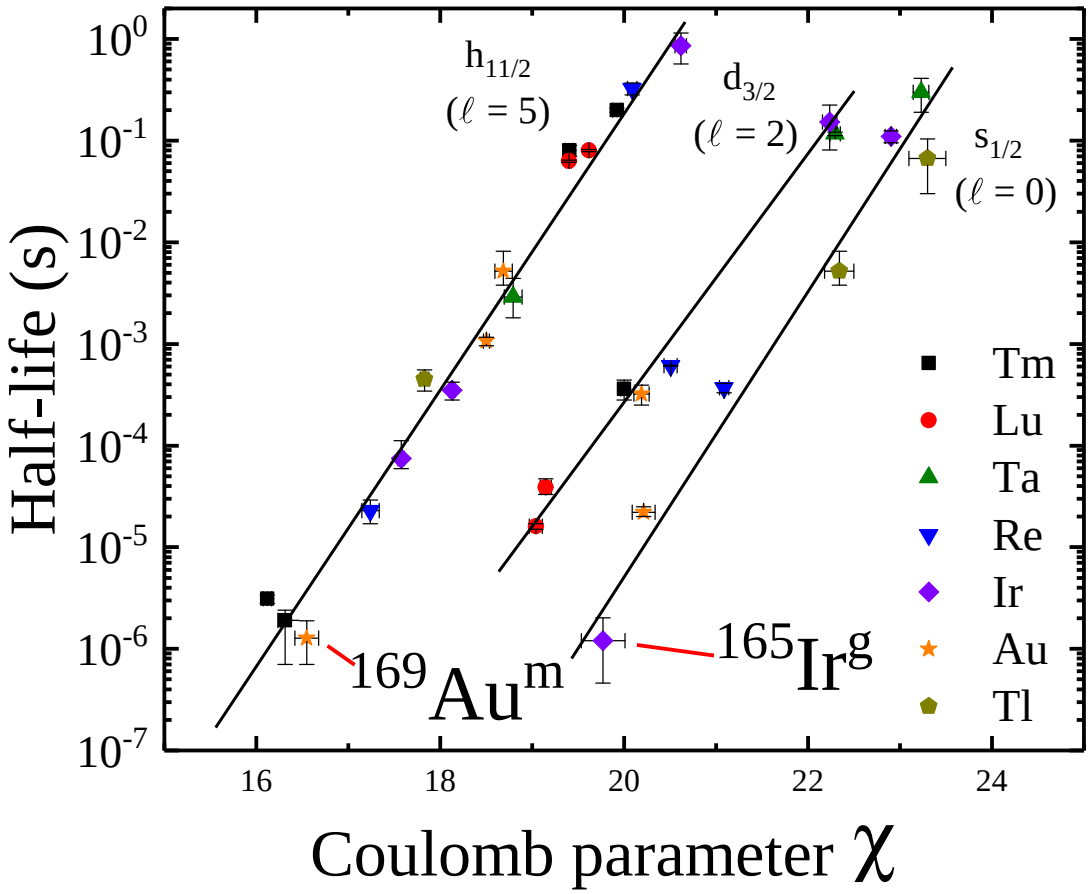

Figure 4.1: Half-lives for proton emission from states in odd-Z elements between thulium and thallium plotted as a function of the Coulomb parameter, $\chi = 2(Z-1)e^2/(4\pi\epsilon_0\hbar v)$, where v is the speed of the emitted proton. Data points for the proton decays of $^{165}\mathrm{Ir}^g$ and $^{169}\mathrm{Au}^m$ are labelled. The solid lines indicating the trends for proton emission from $\pi s_{1/2}$, $\pi d_{3/2}$ and $\pi h_{11/2}$ orbitals are drawn to guide the eye. Data are taken from references [58, 59, 60, 61, 8, 62, 11].

both a ground and isomeric state. There is strong systematic indication that the ground state of ^{165}Ir would be proton unbound. Additionally, there is systematic indication that the next lightest isotope of gold, ^{169}Au, will have a production cross section $\approx$10 nb.

Half-lives of 1.8 μs and 1.2 μs have been estimated for the ^{165}Ir and ^{169}Au decays, respectively, on the basis of a local extrapolation of proton separation energies and a simple model of proton emission [63]. The measurements are compared with fully self-consistent relativistic density functional calculations [64] and the prospects for observing even more neutron-deficient Au and Ir proton emitters or Hg and Pt α emitters are discussed.

4.2 Experimental Details

The experiments were performed at the Accelerator Laboratory of the University of Jyväskylä, Finland. The nuclei of interest were produced in fusion-evaporation reactions induced by a beam of 418 MeV ^{78}Kr^{15+} ions delivered by the K130 cyclotron. The average beam intensity was 12 particle nA. The ^{165}Ir nuclei were produced using a 500 μg/cm^2-thick self-supporting ^{92}Mo foil of $\sim$97 % isotopic enrichment that was bombarded for 67 hours. A ^{96}Ru target foil of 170 μg/cm^2 thickness and 96.5 % isotopic enrichment was bombarded for 257 hours to produce the ^{169}Au nuclei. The ^{96}Ru foil was supported by a 60 μg/cm^2 thick layer of carbon, mounted so that the carbon layer was upstream of the ^{96}Ru material. Both foils were chosen based on availability, with the ^{96}Ru foil being one of only a few in the world. The average energy of fusion-evaporation reaction products ("recoils") emerging from the target was 169 MeV and the electric and magnetic fields of MARA were chosen to optimise the transmission of ^{165}Ir and ^{169}Au for the ^{92}Mo and ^{96}Ru targets, respectively.

Recoils exiting the target were transported within $\sim$600 ns to the focal plane of MARA, where they passed through a Multi-Wire Proportional Counter (MWPC) before being implanted into a Double-sided Silicon Strip Detector (DSSD). The MWPC used in this work contained a grid of 20 μm diameter gold-coated tungsten wires with 1 mm spacing and was filled with 3.5 mbar flowing isobutane gas. It allowed spatial tracking of the recoils, which were dispersed across the MARA focal plane according to their mass number (A) to charge (Q) ratio. The DSSD had 48 horizontal strips on one face and 128 vertical strips on the other, with a nominal thickness of 300 μm. Both faces had a 1 mm strip pitch and each strip was instrumented using Mesytec MPRT-16 charge-sensitive preamplifiers [33]. The preamplifier outputs were digitised using Lyrtech VHS 105 MHz, 14-bit Analogue to Digital Converters [35]. Every DSSD signal was recorded as a 5 μs long "trace" of the digitised output. This allowed proton decays occurring on microsecond timescales to be recorded and analysed. This approach was used to study proton emission from ^{144}Tm ($t_{1/2}$=1.9 μs) [59] and ^{145}Tm ($t_{1/2}$=3.1 μs) [65], which are the shortest-lived previously known decays shown in figure 4.1. The minimum time interval between the implantation of a recoil ion and the measurement

of its subsequent radioactive decay that could be achieved with the electronics used in the present experiment was 850 ns.

Combining recoil flight times between the MWPC and the DSSD with DSSD energy measurements allowed selection of recoils from other implanted ions. Light ions that punched through the DSSD were identified by two silicon detectors mounted adjacently behind the DSSD of 500 μm thickness. Signals observed in the DSSD without a coincident signal in these silicon detectors or in the MWPC were assumed to be from radioactive decays of implanted nuclei. The energy calibration for the new radioactivities was based on the proton-decay energies of ^{170}Au^{g,m} [11], ^{171}Au^{m} [5, 11], ^{164}Ir^{m} [8], ^{165}Ir^{m} [5], and the α-decay energies of ^{169}Pt [11]. Each decay used in calibration was followed by at least 2 correlated full-energy α-decay daughters. The energies measured for these implanted nuclides were corrected for the pulse height defects and for the non-linear response of silicon detectors to low-Z ions [49], and for the contribution to the energy signal from the daughter nuclei recoiling within the DSSD [47, 48]. The escape probability for α particles not depositing their full energy in the DSSD was measured to be $\sim$30 %.

Detector signals were time stamped by a global 100 MHz clock, allowing spatial and temporal correlations between recoils and subsequent radioactive decays within the detector array [39] to be made. The data were analysed with analysis code written in the Python programming language and with the GRAIN software package [42].

Data in this chapter were calculated from the traces taken during this experiment, which were calibrated with the methods in Section 3.7.2. The resulting energy spectra are shown in Figure 4.2. These four energy histograms have no time or energy conditions applied and no veto conditions applied apart from those already presented in sections 3.6.2 and 3.7.2. The presence of clear peaks in the correlated data from data sets A and B is unsurprising considering they were present in the raw drops but the first possible assignment of energy values for the proton decays from the isomeric state of ^{169}Au and the ground state of ^{165}Ir can now be seen.

4.3 Results

4.3.1 Proton decay of the ground state of ^{165}Ir

A clear signature for proton emission from ^{165}Ir is provided by the characteristic chain of 3 short-lived α decays that follow it: $^{165}\text{Ir} \rightarrow {}^{164}\text{Os} \rightarrow {}^{160}\text{W} \rightarrow {}^{156}\text{Hf} \rightarrow {}^{152}\text{Yb}$ [5], see figure 1.1. Traces that were followed by a chain of 3 consecutive decays in the same DSSD pixel were selected from data set A (produced with the ^{92}Mo target). Many of these traces were signals from the implantation of ^{164}Os ions that were produced directly as evaporation residues and implanted into the DSSD. These traces were therefore searched for cases where a second, delayed pulse arising from proton decays of ^{165}Ir was superimposed on the tail of the recoil implantation energy pulse. The energy spectrum extracted from these delayed pulses is shown in figure 4.4(a). For each count

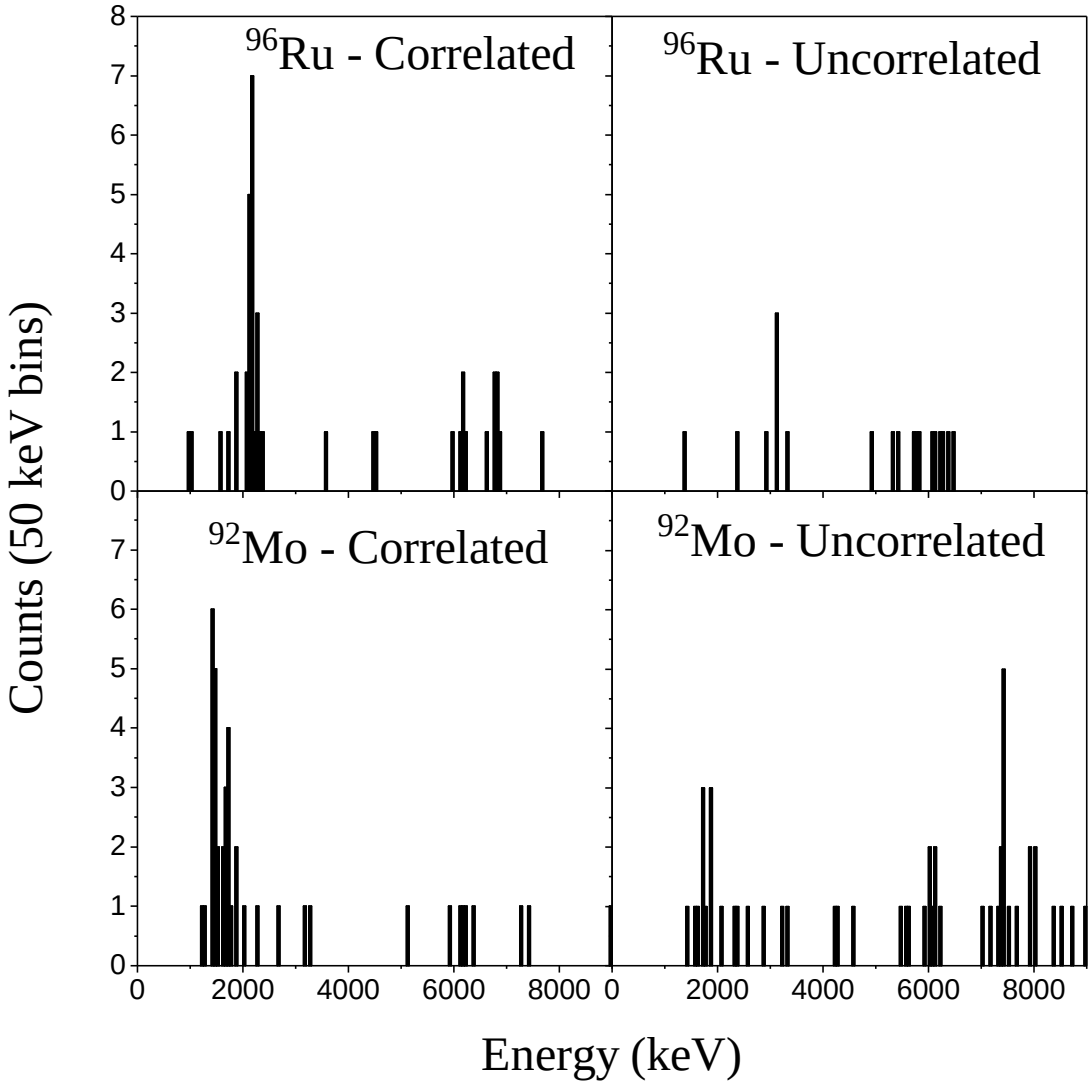

Figure 4.2: Every trace drop observed in this work from the 4 distinct sources has been filtered using the methodology in section 3.6.2 and calibrated using the methodology in section 3.7.2. The resulting energy histograms for each trace source have been plotted with 50 keV bins with no gating applied. The ^{96}Ru spectra are plotted with data set B, and the ^{92}Mo spectra are plotted with data set A. The correlated spectra show events followed by at least one α-like event, and the uncorrelated spectra show events not followed by any other signal.

in this spectrum, at least two of the energies of the α decays that followed it were required to match in sequence the literature values for ^{164}Os, ^{160}W and ^{156}Hf, and the time interval between each decay was required to be consistent with the known half-lives.

Two proton-decay lines can be seen, the higher-energy line corresponding to the 1707 keV proton decays of the $\pi h_{11/2}$ isomer in ^{165}Ir, for which half-lives of 300(60) µs [5] and 340(40) µs [8] have been reported. The lower-energy line comprising 8 counts is assigned as the proton decays of ^{165}Ir^g. The energy of this new proton-decay line was measured to be 1454(38) keV, and its half-life was determined to be $1.20^{+0.82}_{-0.74}$ µs using the method of maximum likelihood [51]. No evidence was found in the data for ^{165}Ir^g proton decays recorded as separate traces, or for a competing α-decay branch from the ground state of ^{165}Ir. The proton-decay branching ratio is therefore assumed to be ≈100 %. Figure 4.4(c) shows the distribution of events across the MARA focal from the 2 proton-decay lines. In both cases they are compatible with the distribution observed for the α decays of the isobar ^{165}Os that is also plotted, supporting their assignments as decays of ^{165}Ir. The cross sections for producing ^{165}Ir^g and ^{165}Ir^m were estimated to be 3 nb and 200 nb, respectively. The latter values compares with an estimated cross section of 200 nb using the same reaction, but at a beam energy of 384 MeV [5].

The number of escaped decays is higher for those traces from data set A compared with those from data set B, with 20(5)% of the ^{96}Ru target decays escaping compared with 35(11)% of the ^{92}Mo target decays. Both of these are within normal statistical fluctuation of the expected value of 30%.

4.3.2 Proton and α decay of ^{169}Au

A similar analysis was performed to search the correlated data set obtained using the ^{96}Ru target for ^{169}Au proton decays. The daughter nuclide in this case is ^{168}Pt, which α-decays to ^{164}Os (see figure 4.3). Figure 4.4(b) shows the energy spectrum extracted from decays of ^{169}Au nuclei that were followed by a chain of 4 consecutive decays in the same DSSD pixel. For each count in this spectrum, at least two of the energies of the α-decays that followed it were required to match in sequence the literature values for ^{168}Pt, ^{164}Os, ^{160}W and ^{156}Hf, and the time interval between each decay was required to be consistent with the known half-lives. A peak comprising 15 counts can be seen just above 2 MeV, which is assigned as the proton decays of ^{169}Au. The counts at lower energies are assumed to be from decay particles that escaped the DSSD without depositing their full energy. The energy of the proton-decay line was measured to be 2182(28) keV. The Q value for the decay would therefore be 2187(35) keV, which agrees well with the prediction of 2198(40) [63]. The time distribution for these events is shown in figure 4.4(d), which indicates that these decays all proceed from a single decay species. The half-life was determined to be $1.19^{+0.41}_{-0.24}$ µs using the method of maximum likelihood [66] and correcting for the finite trace length [50].

A single count is also evident in figure 4.4(c) above 7 MeV. It was followed by a

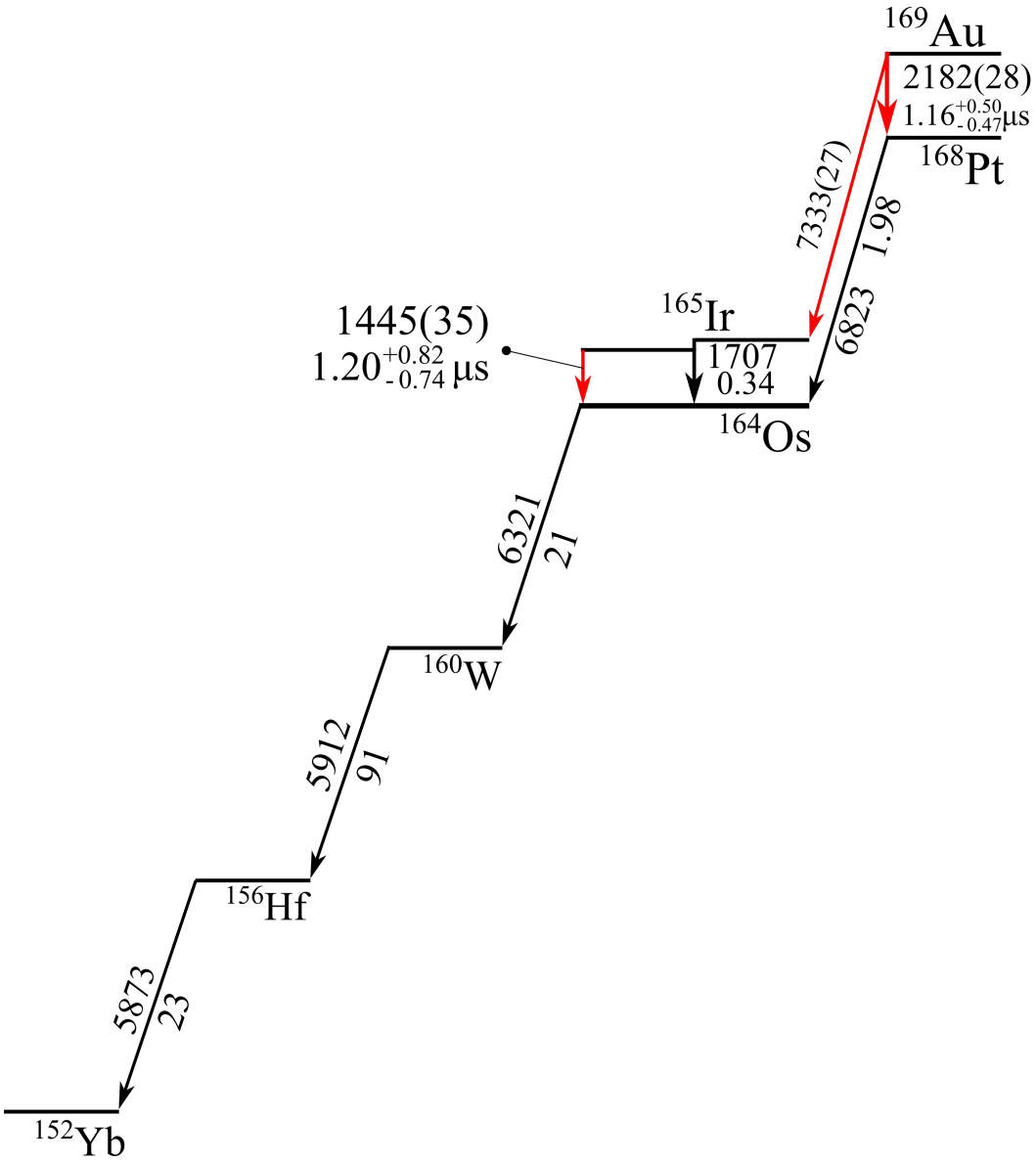

Figure 4.3: Schematic diagram showing the decays of ^{169}Au^m and ^{165}Ir^g indicated by the red arrows. Decays to the ground state of ^{164}Os are followed by the sequence of α-decays of ^{164}Os, ^{160}W, and ^{156}Hf.. The α-decay energies E_α and half-lives $t_{1/2}$ are taken from the present work and references [6, 5, 8, 9]. Energies are given in keV and half-lives of previously known decays are given in ms.

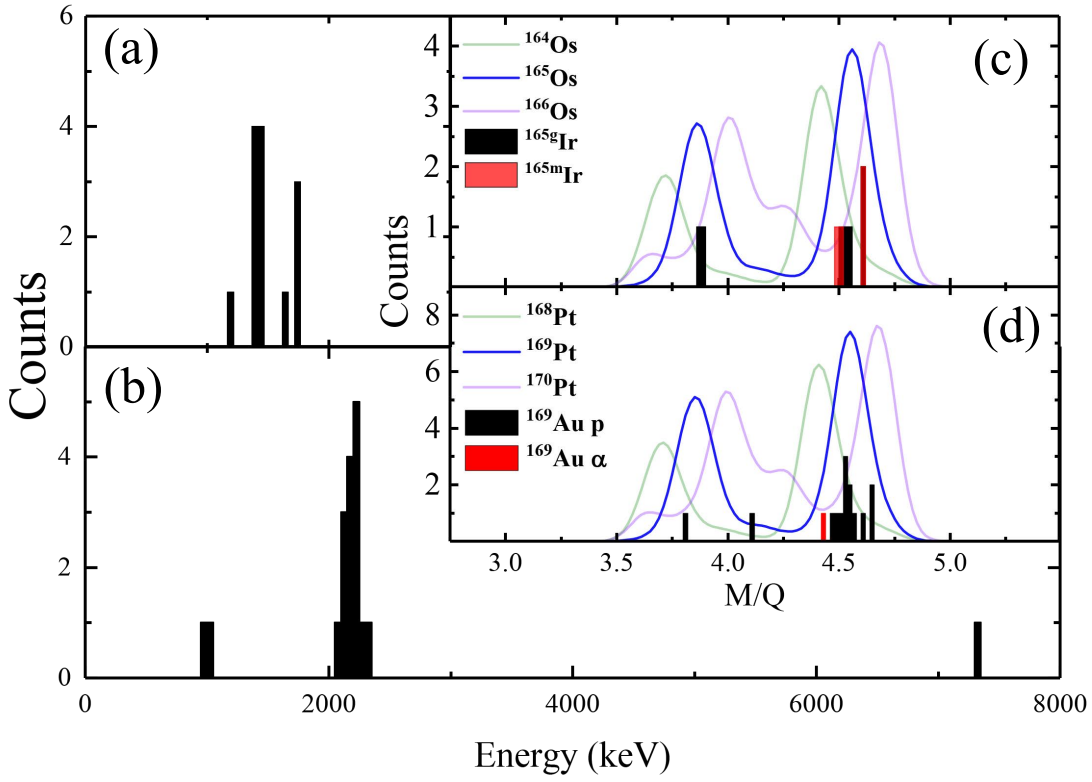

Figure 4.4: (a) Energy spectrum of decays extracted from the analysis of traces where a delayed decay signal was superimposed on the pulse from an implanted recoil. The traces were selected by requiring that 3 decays were observed in the same DSSD pixel before the next recoil was implanted and that at least 2 of these decays had energies consistent with literature values for the ^{164}Os α-decay chain. (c) The horizontal position distribution measured using the MWPC at the focal plane of MARA of recoil ions correlated with the 2 proton-decay lines of ^{165}Ir shown in (a). The corresponding distribution measured for ions correlated with ^{164,165}Os and ^{166}Ir α-decays and ^{165}Ir^m proton decays from event data is also shown for comparison on a modified vertical scale. (b) As (a), except requiring 4 subsequent decays in the same DSSD pixel, at least 2 of which had energies consistent with being from the ^{168}Pt α-decay chain. (d) As (c) for the ^{169}Au^m decays, compared with the distribution of ions correlated with ^{168,169,170}Pt α-decays. The main components in (b) and (d) correspond to ionic charge states of Q = 33$^+$ and 34$^+$.

sequence of particles with energies of 1691 keV, 6293 keV, 5908 keV and 5865 keV. This decay sequence is interpreted as an α decay of ^{169}Au, followed by a proton decay of ^{165}Ir^m, then the α decays of ^{164}Os, ^{160}W, and ^{156}Hf (see figure 4.3). The time intervals between successive decays were 0.37 ms, 6.0 ms, 64 ms and 26 ms, respectively, and are compatible with the reported half-lives of these proton and α emitters [5, 6]. An α-particle of energy 7333(27) keV was deduced for this ^{169}Au α decay, which occurred 1.3 µs after the recoil ion was implanted. This short time difference is consistent with the half-life measured for the ^{169}Au proton-decay line, while the combined Q value for this α decay and that of the proton decay of ^{165}Ir^m is consistent within uncertainties with the combined Q value for the proton decay of ^{169}Au and the α decay of ^{168}Pt. These observations are compatible with both the proton and α decays of ^{169}Au emanating from the same state. Furthermore, the horizontal position distribution shown in figure 4.4(d) confirms that these decays are consistent with their assignment to an $A = 169$ isobar. Combining the data for both decay branches yielded a half-life of $1.16^{+0.50}_{-0.47}$ µs and an estimated production cross section of 5 nb for this state in ^{169}Au.

4.4 Discussion

The proton-decay energy and half-life measured for the ground state of ^{165}Ir in the present work fit in well with the trend observed for $s_{1/2}$ proton emission plotted in figure 4.1. The values are also consistent with those estimated in reference [63] assuming proton emission from a $\pi s_{1/2}$ orbital. Comparison with Wentzel-Kramers-Brillouin (WKB) calculations using the global optical model of Becchetti and Greenlees [30] assuming proton emission from a $\pi s_{1/2}$ orbital yields a reduced proton-decay width of $0.75^{+1.05}_{-0.61}$. This is consistent with the low-seniority shell-model calculation value 0.33 [5], although the uncertainty is large. The difference in Q value between the 2 proton-decay lines of ^{165}Ir allow the excitation energy of the $\pi h_{11/2}$ isomer to be established as 221(34) keV. This is slightly higher than the value of 175.3(2.2) keV deduced for its isotope ^{167}Ir [5], but fits in well with the systematics in this region [67].

Systematic studies of α-decay branches of odd-A proton emitters in this region have established that the strongest transitions connect states with the same proton configurations [5, 68, 69, 11, 60]. This suggests that the odd proton in the α-decaying state in ^{169}Au is in a $\pi h_{11/2}$ orbital, because this is the configuration assigned to the states it populates in ^{165}Ir [5]. The calculated partial half-life for an unhindered 7333 keV α-decay from ^{169}Au using the method of Rasmussen [25] is ∼180 µs. On the basis of this and the measured half-life, an α-decay branching ratio of <1 % would be expected. The measured quantities of proton and α-decays yield a branching ratio of ∼6 %, but such a high value would imply a reduced α-decay width that is unphysically high. One possible explanation is that the α particle did not deposit its full energy, but this seems unlikely given that the Q-value sums for the 2 decay paths from ^{169}Au to ^{164}Os agree so well. It seems more likely that the observation of this α-decay event

is an upward statistical fluctuation and that the real α-decay branching ratio is rather lower than might be suggested by the present observations.

The assignment of the state observed in ^{169}Au as having its unpaired proton in a $\pi h_{11/2}$ orbital is strongly supported by its measured proton-decay properties, which fit in well with the trend observed for $h_{11/2}$ proton emission plotted in figure 4.1. The measured proton-decay energy and half-life also agree well with the predictions for this state, which is expected to lie at an excitation energy of 287 keV [63]. A WKB calculation assuming $h_{11/2}$ proton emission yields a reduced proton-decay width of $0.29^{+0.17}_{-0.14}$, which compares with the value of 0.22 expected from low-seniority shell-model calculations [5].

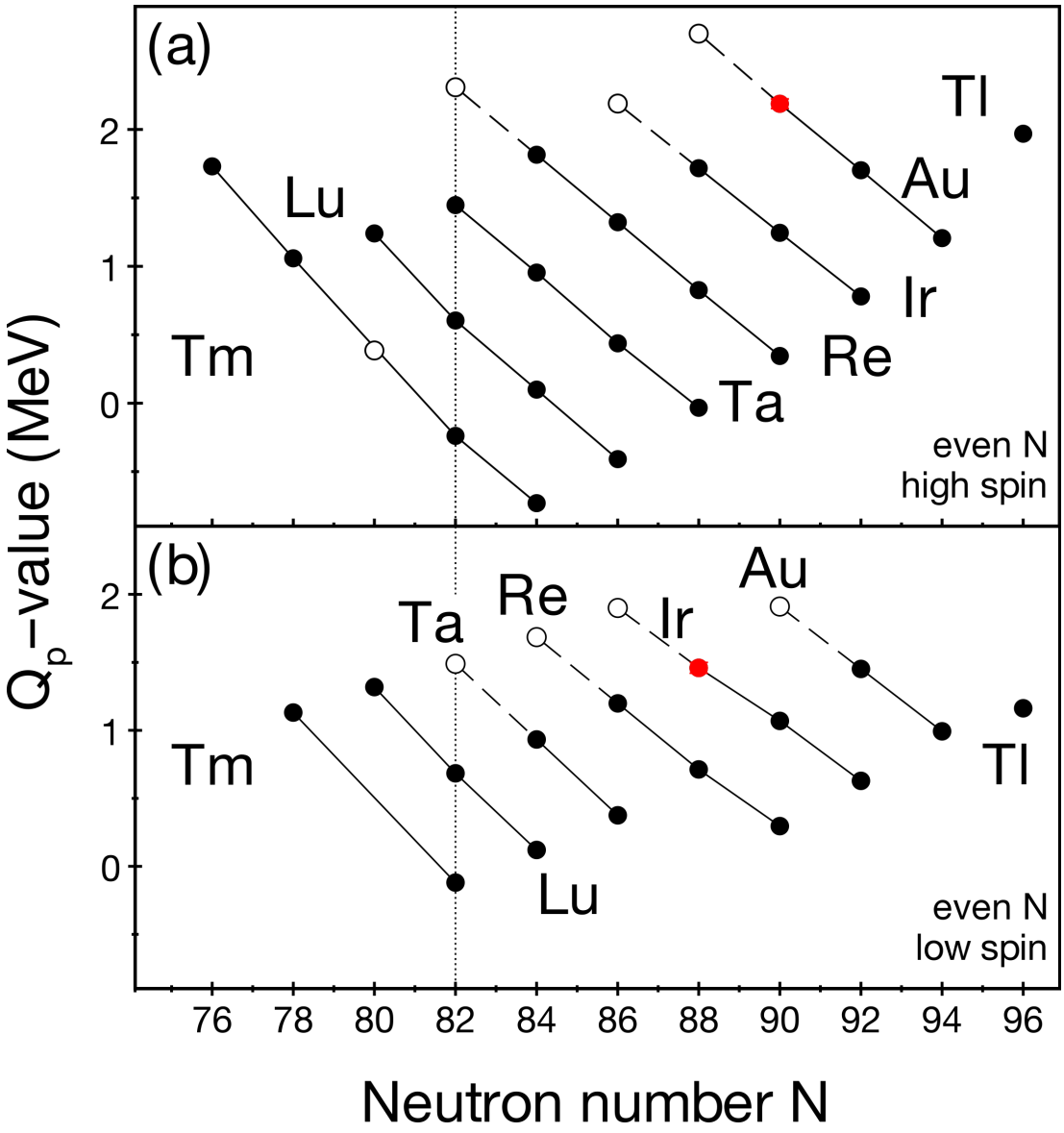

Figure 4.5: The proton decay Q-values for odd-Z, even-N nuclides in the region of Ir and Au. (a) shows the Q_p values for protons emitted from a $h_{11/2}$ isomeric state, and (b) shows those emitted from a $s_{1/2}$ ground state. The values from this work are plotted in red, and show good agreement with existing trends. Open symbols indicate the predictions from [63].

Chapter 5

α-decays of ^{165}Pt and ^{170}Hg

This work presents the discovery of new nuclides ^{165}Pt and ^{170}Hg which were identified via their α decays. These results are covered already in the author's paper on the subject [1]. Heavy-ion fusion-evaporation reactions of ^{78}Kr(^{96}Ru,4n)^{174}Hg* and ^{78}Kr(^{92}Mo,5n)^{170}Pt* were used to produce ^{170}Hg and ^{165}Pt, respectively and were separated using the MARA vacuum-mode mass separator. The α-decay energies and half-lives have been measured for the first time for decays of ^{165}Pt and ^{170}Hg, and their reduced decay widths have been calculated, allowing comparison with wider systematic data in the region.

5.1 Motivation

Half-life and α-particle energy measurements allow reduced α-decay widths to be calculated, which are useful when assigning parities and spins to involved states. Decay Q values can also assist in potential refinement and testing of theoretical mass models. Systematic analysis of these attributes can reveal new information about how shell effects such as magic numbers evolve far from β stability. For example, if an α-decay is measured to have a reduced decay width that indicates it is unhindered, and it populates a ground state with known spin and parity, this greatly assists assignment of spin and parity for the emitting state. If the α-decay Q-values are known for a chain of nuclides, and the mass anywhere along the chain is directly measured, then the masses of all the nuclides in the chain are calculable.

The lightest known platinum isotopes before this thesis were ^{166,167}Pt, with half-lives of $t_{1/2} = 0.3(1)$ ms, $0.7(2)$ ms and α-particle energies of $E_\alpha = 7110(15)$ keV, $6988(10)$ keV for ^{166}Pt and ^{167}Pt, respectively [4]. The lightest known mercury isotope known was ^{171}Hg, with values of $t_{1/2} = 59^{+36}_{-16}$ μs and $E_\alpha = 7488(12)$ keV reported [11].

This thesis improves on previous Pt results by providing higher precision energy and half-life measurements as well as reporting the α-decay energies and half-lives of new nuclides ^{165}Pt and ^{170}Hg.

The α decay particles from the new nuclides were assigned via standard correlation

analysis (discussed in section 3.6.1). Both new nuclides have sufficiently long half-lives that trace analysis was not required. The α-decay chains following target nuclei can be seen in Figure 5.1.

5.2 Experimental Details

A complete description of the experimental setup is covered in Sections 3.2 and 3.3.4. The setup is also covered in Chapter 4, so is omitted for brevity.

A full width at half maximum (FWHM) value measured for the ^{169}Pt α-decay line ($E_\alpha = 6678(15)\,\text{keV}$ [46]) in the BB17 DSSD was 40 keV. The FWHM of the $^{155}\text{Lu}^m$ α-decay ($E_\alpha = 7390(5)\,\text{keV}$ [6]) line in the BB20 DSSD was 33 keV.

Recoils were dispersed across the MARA focal plane according to their mass number (A) to charge (Q) ratio. Figure 5.2 shows a two-dimensional spectra of this ratio for the recoils versus the energy of subsequent α particles in the same DSSD pixel. Combining recoil flight times between the MWPC and the DSSD with DSSD energy measurements allowed selection of recoils from other implanted ions. Light ions that punched through the DSSD were identified by two silicon detectors mounted adjacently behind the DSSD of 500 μm thickness. Signals observed in the DSSD without a coincident signal in these silicon detectors or in the MWPC were assumed to be from radioactive decays of implanted nuclei.

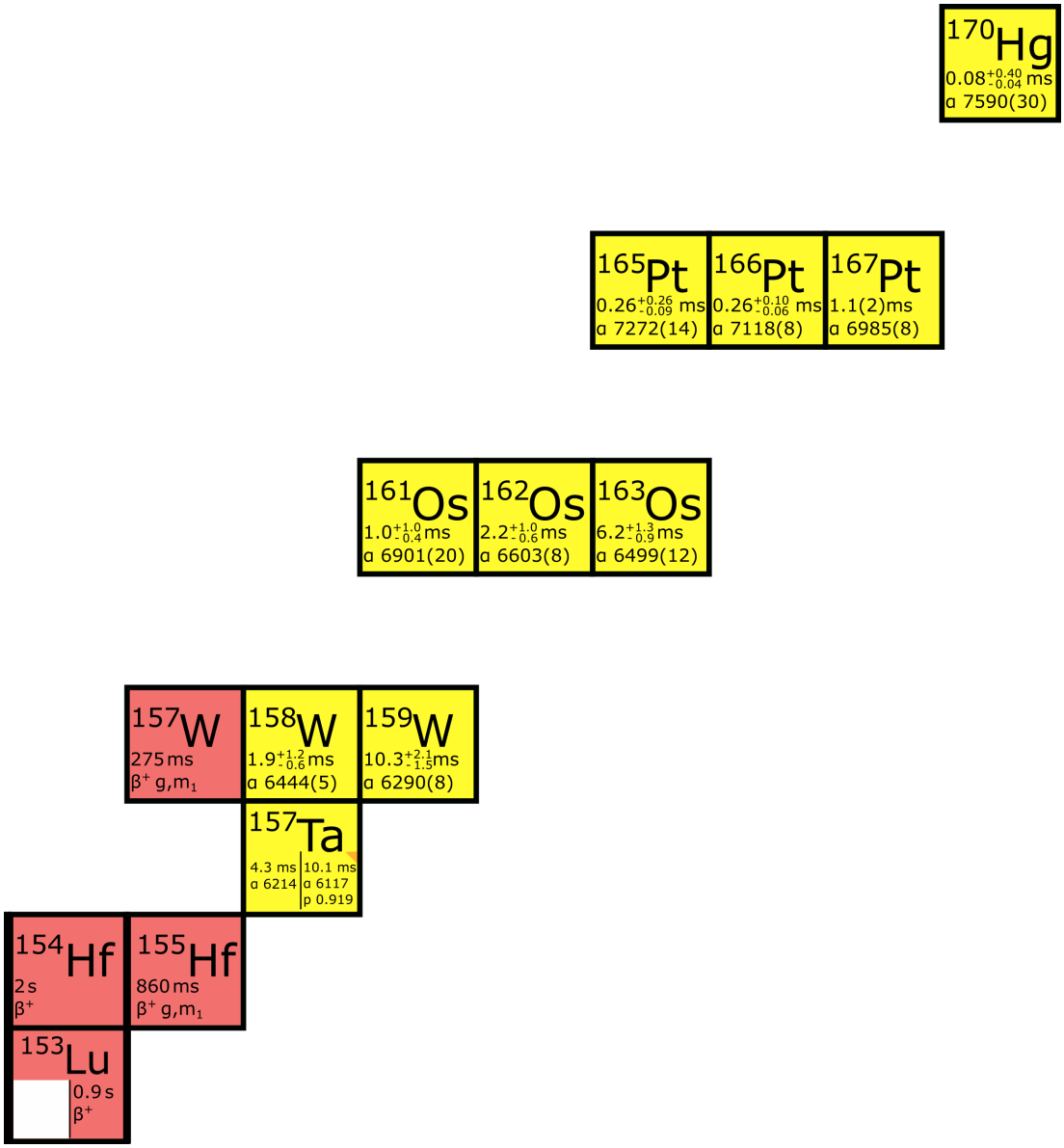

Figure 5.1: The decay chains of the nuclides of interest labelled with the α-particle energies (E_α) and half-lives ($t_{1/2}$) measured in this work. The dashed arrows denote fusion-evaporation channels, while the solid arrows indicate α-decays. The link between ^{157}W and ^{157}Ta is a β-decay. Figure taken from [1].

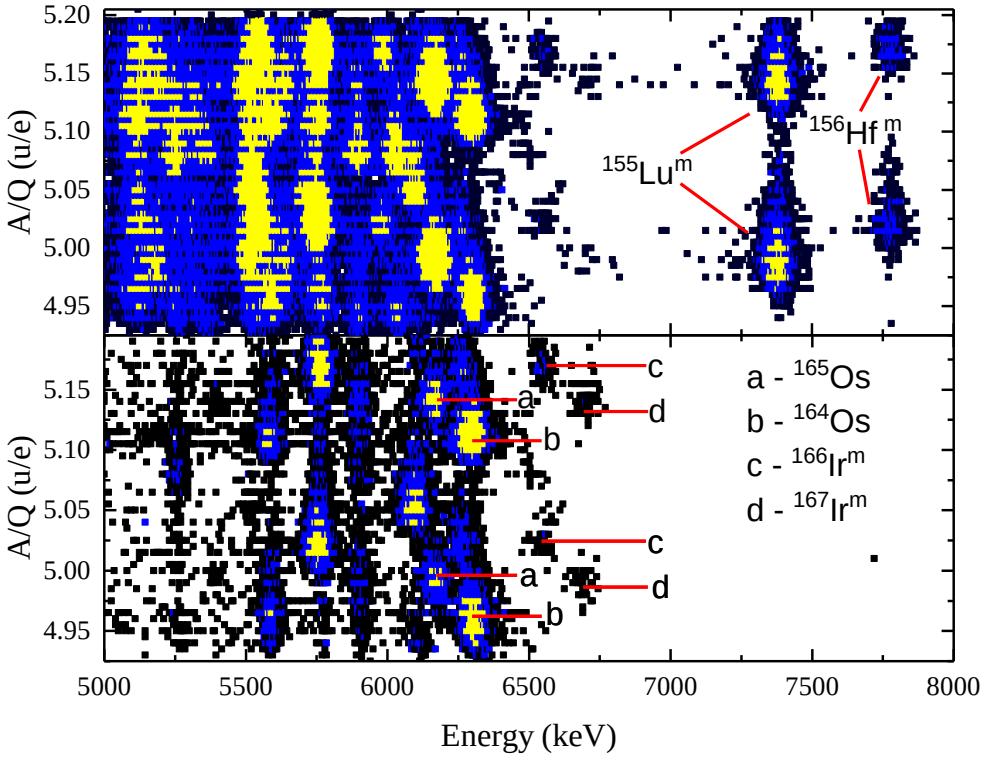

Figure 5.2: The upper panel shows the distribution of the energies of α-particles occurring within 10 ms of a recoil being implanted into the same DSSD pixel plotted against the ratio of the mass number to charge state (A/Q) of the recoil at the MWPC. The lower panel shows the α-particle energy spectrum of decays occurring within 10 ms of the recoil that are followed by another α-particle within 50 ms versus the A/Q of the recoil. The plots present the part of data set A that was used to calibrate the A/Q distribution for the experiment and show that two charge states were collected for each labelled nuclide. The colour scale in both panels is set such that black points represent 2-4 events, blue points 5-24 events and yellow points $\geq$25 events. Figure taken from [1].

5.3 Results

This section will report the α-decay energies, half-lives and reduced decay widths for all nuclides identified in event data via their α-decay chains. The majority of the numerical results are summarised in Table 5.1.

5.3.1 Decay of ^{165}Pt

The ground state of ^{165}Pt is expected to decay predominantly via α-particle emission [72]. Figure 5.1 shows the daughter of the α-decay of ^{165}Pt is ^{161}Os, first reported by Bianco *et al.* with a half-life of 0.64(6) ms and α-particle energy of 6890(12) keV [71]. The α-decay daughter of ^{161}Os, ^{157}W, undergoes β decay with a half-life of 275(40) ms. These β decays indirectly populate low-lying states in ^{157}Ta, which in turn undergo α-decay with α-particle energies of 6117(4) keV and 6213(4) keV and half-lives of 10.1(4)

Table 5.1: Comparison of α-particle energies (E_α) and half-life values ($t_{1/2}$) of isotopes obtained in the present work against earlier studies. Note that for Os and W, the values given here are based only on the events correlated with a Pt or Hg decay. The decay widths, Rasmussen half-lives and hindrance factors were calculated with the energies and half-lives from this work for the Pt and Hg isotopes and using the literature values for the Os and W isotopes. Table taken from [1].

Isotope	Present Work		Previous Work		δ^2_α (keV)	$t^{\mathrm{Ras}}_{1/2}$ (ms)	HF
	E_α (keV)	$t_{1/2}$ (ms)	E_α (keV)	$t_{1/2}$ (ms)			
^{170}Hg	7590(30)	$0.08^{+0.40}_{-0.04}$	—	—	63^{+79}_{-53}	0.07	1
^{167}Pt	6985(8)	1.1(2)	6988(10)[4]	0.7(2)[4]	57^{+15}_{-14}	0.86	1.66
^{166}Pt	7118(8)	$0.26^{+0.10}_{-0.06}$	7110(15)[4]	0.3(1)[4]	95^{+33}_{-29}	0.34	1
^{165}Pt	7272(14)	$0.26^{+0.26}_{-0.09}$	—	—	33^{+23}_{-18}	0.12	2.65
^{163}Os	6499(12)	$6.2^{+1.3}_{-0.9}$	6514(10)[4]	5.5(6)[4]	72^{+3}_{-2}	6.15	1.24
^{162}Os	6603(8)	$2.2^{+1.0}_{-0.6}$	6600(3)[70]	1.9(2)[70]	109^{+10}_{-8}	3.13	1
^{161}Os	6901(21)	$1.0^{+1.0}_{-0.4}$	6890(12)[71]	0.64(0.6)[71]	37(3)	0.37	2.41
^{159}W	6290(8)	$10.3^{+2.1}_{-1.5}$	6292(5)[6]	8.2(0.7)[6]	45(2)	5.23	2.04
^{158}W	6444(5)	$1.9^{+1.2}_{-0.6}$	6445(3)[70]	1.5(0.2)[70]	75^{+9}_{-7}	1.55	1

ms and 4.3(1) ms [6, 68].

Four ^{165}Pt α-decays were identified in data set A by searching for events followed by the decay chain characteristic to its daughter nucleus, ^{161}Os, in the same pixel. Fig 5.3(a) shows the energy of decays that occurred within 10 ms of recoil implantation versus the energy of daughter decays that occurred within an additional 50 ms. Three correlated event chains can be seen where the daughter energy is consistent with that reported for ^{161}Os. The mean lifetimes of the daughter decays are consistent with the reported half-life of ^{161}Os.

Analysis of the granddaughter decays for these chains is presented in Table 5.2. The energy of the first two decays are consistent with the α-decay energy of ^{157}Ta, while the third has a much lower energy. The escape probability for α particles not depositing their full energy in the DSSD was measured to be ∼30 %. It is therefore likely that the ^{157}Ta α particle in this decay chain is an escape. DSSD signals with energies recorded below 0.5 MeV were excluded during analysis. This meant that β particle decays of ^{157}W (which generally deposit less than this) were not considered. The daughter-granddaughter decay time intervals for all three cases are compatible with reported half-lives for ^{157}W and states in ^{157}Ta. On the basis of this evidence, these decay chains are assigned as the α-decays of the new nuclide ^{165}Pt. In the fourth decay chain presented in Table 5.2, the daughter energy is assigned as an escaping ^{161}Os α particle. The granddaughter decay energy matches that of the ground state of ^{157}Ta, so the initial decay is assigned to ^{165}Pt. The full-energy α-decays of all 4 ^{165}Pt decay chains are shown in Figure 5.4(a).

The α-particle energy for ^{165}Pt was calculated to be 7272(14) keV by taking the mean of the 4 decay chains, based on the energy calibration for data set A shown in Table 3.4. For the fourth decay chain, the time interval between the recoil implantation and the ^{165}Pt α-decay is much smaller (22 µs) than the other 3, (450 µs - 550 µs). The distribution of the 4 decay times was therefore analysed using the method of ref. [52] and found to be consistent with originating from the same state. Correcting for a maximum time interval of 10 ms and using the maximum likelihood method [66], a half-life for ^{165}Pt of $0.26^{+0.26}_{-0.09}$ ms was determined. The α-decay branching ratio is therefore assumed to be ≈100 %, as this is much shorter than the predicted β decay half-life for ^{165}Pt [72].

It is noted that the procedure used to find the ^{161}Os decay in chain 2 was not the same as for the other chains. The y-strip assigned to the decay in GRAIN was -1, and its energy collected from the y side of the detector was also -1. A value of -1 is used to indicate that there is no data stored for a property of an object in GRAIN and it is possible that the energy, strip and pile-up information for the y-strip in chain 2 was discarded by the event builder filter and not recorded. The filter was necessary to prevent the DAQ from crashing while collecting traces. It is unknown exactly what caused this effect. Nevertheless, the x-strip listed is the same as those of the recoil, ^{165}Pt and ^{157}Ta signals. There are 128 x strips in the BB17 DSSD so the likelihood

Table 5.2: Alpha-particle energies (E_α) and time intervals (τ) of all events (separated by column) observed in the ^{165}Pt decay chains, compared with literature values where available. Note that because the present experiment was not sensitive to β particles, the time interval between a given ^{161}Os α decay and its associated subsequent ^{157}Ta α-decay represents the sum of the time interval between the ^{161}Os α decay and the ^{157}W β decay, and the time interval between this ^{157}W β decay and the ^{157}Ta α-decay. α-particles assumed to have escaped from the detector are indicated by italics. Table taken from [1].

Nuclide	E_α^1	E_α^2	E_α^3	E_α^4	E_α^{ref} (keV)
^{165}Pt	7267	7267	7286	7265	—
^{161}Os	6941	6872	6891	*2612*	6890(12) [71]
^{157}Ta	6158	6187	*2963*	6110	6117(4) [68] 6213(4) [6]
Nuclide	τ^1	τ^2	τ^3	τ^4	$t_{1/2}^{\mathrm{ref}}$ (ms)
^{165}Pt	0.45	0.55	0.50	0.022	—
^{161}Os	2.2	1.35	1.0	1.4	0.64(0.06) [71]
^{157}W					275(40) [71]
^{157}Ta	288	186	490	91	10.1(4) [68] 4.3(1) [6]

of this being in the same strip randomly is $< 3\%$ assuming $\approx 30\%$ of strips are active. The energy recorded from the x side of the DSSD and the decay time match that of ^{161}Os very well, so despite the unusual method of correlation, the decay is assigned as normal. Note that to find this decay, it was necessary to trigger on the x side of the detector rather than the usual y side, and the calibration for the x-side energy was performed by comparing to other events that had recorded energies from both faces.

5.3.2 Decays of ^{166,167}Pt

Bingham *et al.* used beams of 357 MeV and 384 MeV ^{78}Kr ions to bombard a ^{92}Mo target [4] to first identify ^{166,177}Pt. Data set A in the present work used significantly higher beam energy of 418 MeV with the same beam and target combination. No decay chains of ^{166,167}Pt were identified in data set A, which is likely a consequence of lower production cross sections at this higher beam energy. However, both isotopes were produced via αxn evaporation channels using the ^{96}Ru target (see Figure 5.1) and subsequently identified in data sets B and C. In total, 35 decay chains of ^{167}Pt and 11 decay chains of ^{166}Pt were identified. Figures 5.4(b) and (c) show their triple-correlated

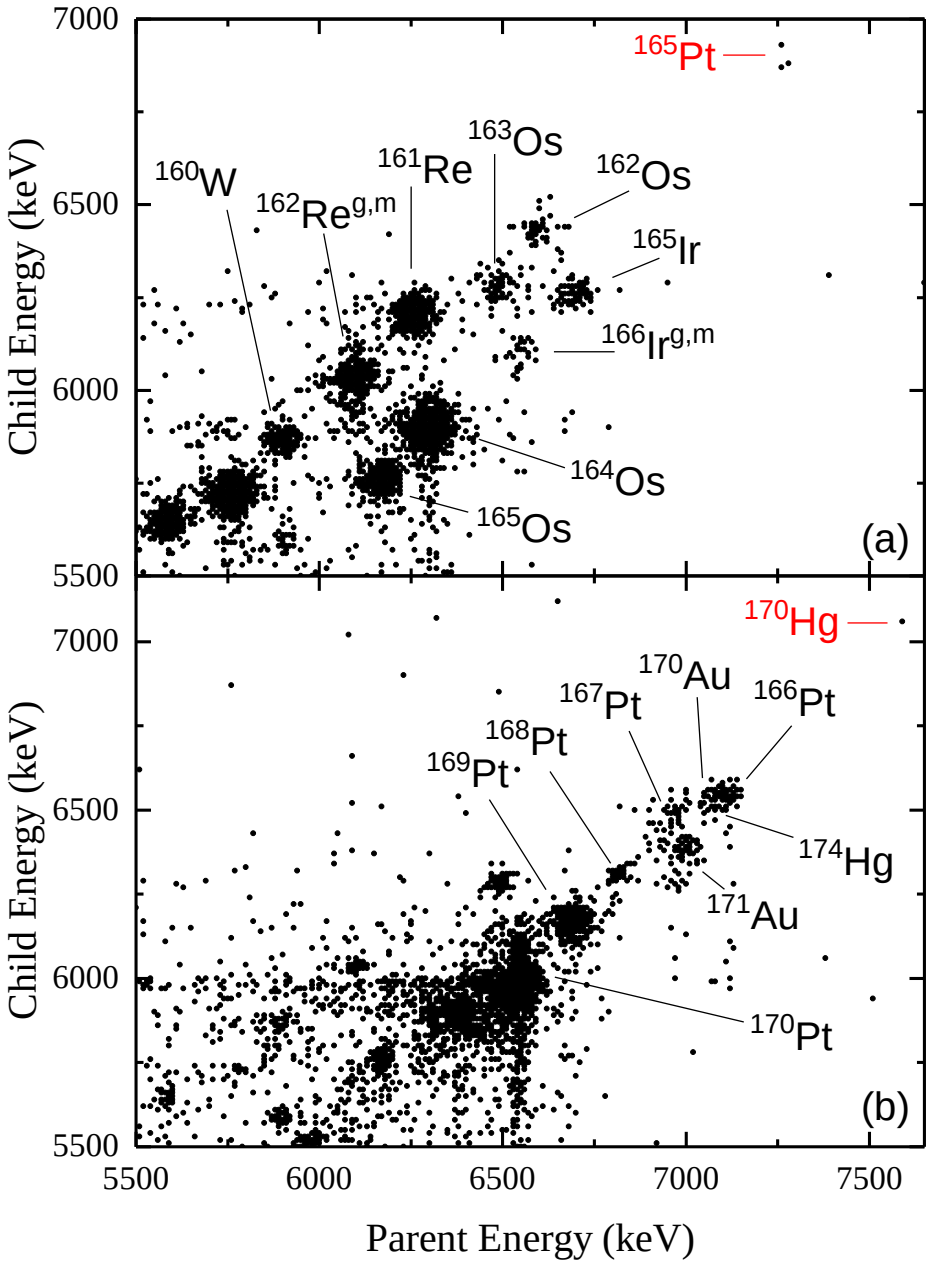

Figure 5.3: Two-dimensional spectra of α-particle energies of mother decays occurring within 10 ms of a recoil being implanted into the same DSSD pixel plotted against those of subsequent daughter α-decays occurring (a) within 50 ms from data set A, and (b) within 100 ms from data set C. Selected correlated mother α-decays are labelled, with newly identified nuclides highlighted in red. Decays in the top left of panel (b) were checked for correlation with the chain following ^{170}Hg, and none were found to be candidates for an escaped ^{170}Hg decay. Figure taken from [1].

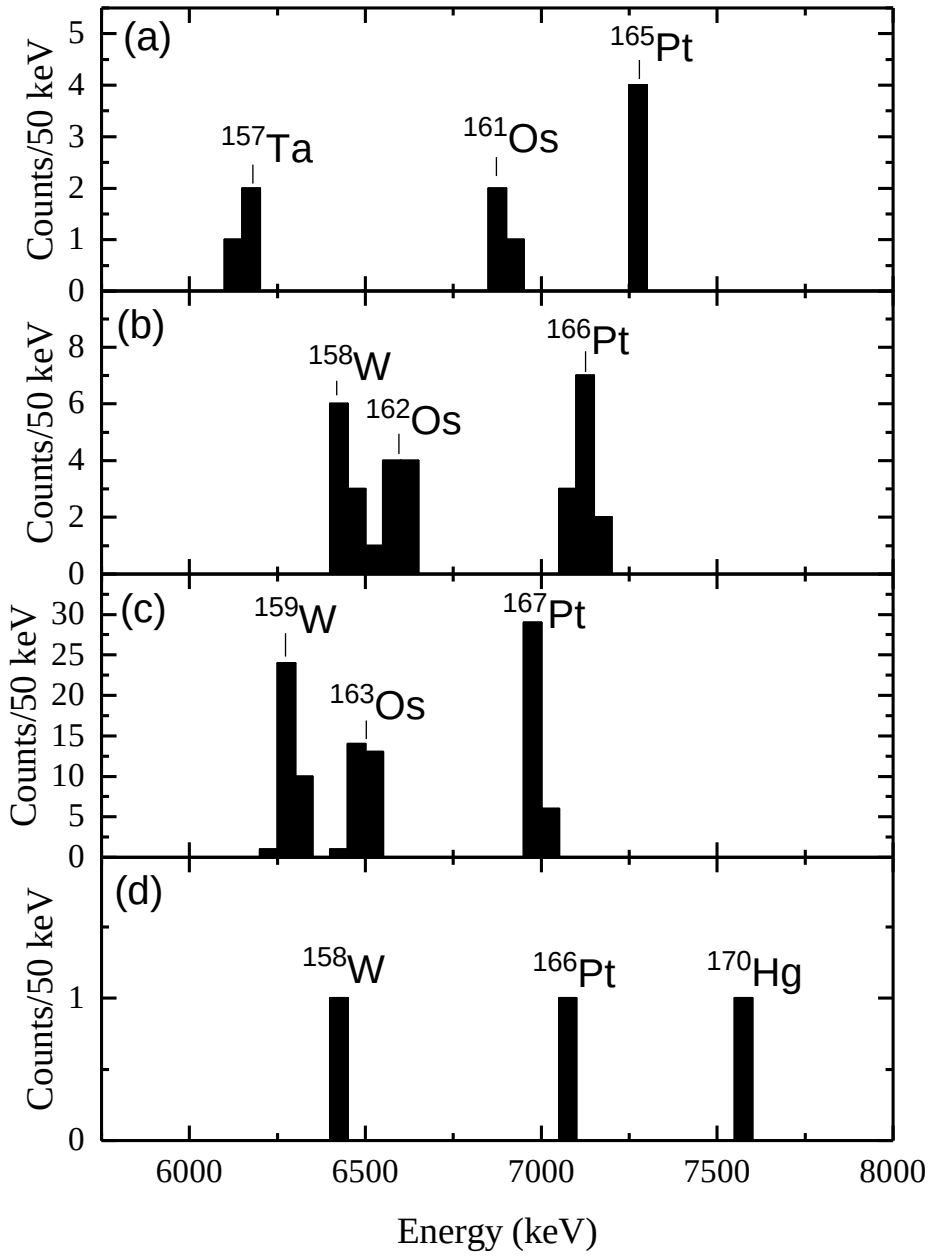

Figure 5.4: Energy spectra of multiply correlated α-decays for the decay chains of (a) ^{165}Pt, (b) ^{166}Pt, (c) ^{167}Pt, and (d) ^{170}Hg. The individual decay energies and time intervals for events in the ^{165}Pt chains are summarised in Table 5.2. The individual decay energies and time intervals for events in the ^{170}Hg chain are summarised in Table 5.3. Figure taken from [1].

α-decays. It can be seen in Figure 5.3(b) that daughter decay correlations were insufficient to separate decay chains of interest from interfering activities such as ^{170}Au and ^{174}Hg in the case of ^{166}Pt and ^{171}Au in the case of ^{167}Pt. Clean separations were made possible with granddaughter correlations, hence only double or better correlated events were accepted. A half-life of 1.1(2) ms and an α-particle energy of 6985(8) keV were deduced for ^{167}Pt, and similarly 7118(8) keV and $0.26^{+0.10}_{-0.06}$ ms were deduced for ^{166}Pt. All values show good agreement with previously reported results. The energy calibration for data sets B and C was based on the α-decays shown in Table 3.4, as described in Section 3.7.1.

5.3.3 Decay of ^{170}Hg

One decay chain for the α-decay of ^{170}Hg [72] was identified (shown in Figure 5.3(b)). The candidate ^{170}Hg α-particle with E_α=7590 keV was followed by particles with energies 7065 keV, 1840 keV and 6430 keV and occurred 0.12 ms after a recoil implantation in the same DSSD pixel. The events can be seen in full in Table 5.3. This decay chain is assigned as the α-decays of ^{166}Pt, ^{162}Os, and ^{158}W, where the ^{162}Os α particle escaped DSSD before depositing its full energy (see Figure 5.1). The successive decay time intervals are compatible with reported half-lives of these α emitters [4, 70], and were measured to be 0.23 ms, 1.50 ms, and 3.35 ms, respectively. Figure 5.4(d) shows α-particle energies of this triple-correlated decay chain. Correcting for a maximum 10 ms time interval [66] and using the maximum likelihood method, a half-life of $0.08^{+0.40}_{-0.04}$ ms was deduced for the ^{170}Hg candidate. Similar to ^{165}Pt, the α-decay branching ratio is assumed to be ≈100% as this is much shorter than the predictedβ-decay half-life for the branch [72].

Table 5.3: The energy and decay time values for each event in the chain leading to the observation of a ^{170}Hg candidate, listed with reference literature values for comparison. Table taken from [1].

Isotope	α **Energy** (keV)		**Decay time** (ms)	
	Experiment	Ref	Experiment	Ref
^{170}Hg	7590	—	0.12	—
^{166}Pt	7065	7110(15) [4]	0.23	0.3(1) [4]
^{162}Os	*1840*	6600(3) [70]	1.5	1.9(2) [70]
^{158}W	6430	6445(3) [70]	3.35	1.5(0.2) [70]

5.3.4 Cross sections

The production cross section for ^{170}Hg at a beam energy of 390 MeV was estimated to be ∼0.5 nb in data set C. The cross section reported for ^{166}Pt by Bingham *et al.* [4] was 4 nb, which was also produced via the 4n evaporation channel. The lower ^{170}Hg

value could be a due to increased competition from fission in the de-excitation of the compound nucleus ^{174}Hg compared with ^{170}Pt.

The production cross section of ∼0.7 nb was estimated for ^{165}Pt via the 5n evaporation channel. This continues the relationship between increasing number of evaporated neutrons needed to produce isotopes and decreasing cross sections for nuclei that lie further from the line of β stability. ∼0.7 nb is consistent with the upper limit of 1 nb reported by Bingham *et al.* [4]. Cross sections of 3.4 nb and 14 nb at 390, and of 0.7 nb and 1.0 nb at 418 MeV were calculated for ^{166,167}Pt, respectively. The value for ^{166}Pt for production via the 4n evaporation channel at 390 MeV is comparable with that reported by Bingham *et al.*. The cross sections for ^{167}Pt are lower than their value of 65 nb for the 3n channel [4], likely due to the different beam energies used. No evidence was found in data sets B or C for ^{165}Pt decay chains produced via the α5n evaporation channel.

5.4 Discussion

The measured ^{165}Pt α-particle energy conforms to the existing systematic trend seen in heavier Pt isotopes, as can be seen in Figure 5.5(a). The energy deduced from the single decay chain for ^{170}Hg agrees with systematic α-decay Q values for the Hg isotope ground states. The reduced α-decay width for ^{170}Hg is 63^{+79}_{-53} keV, which is compatible with those for α-decays of other even-even nuclei in this region (see Figure 5.6(a)). The value was determined using the method of Rasmussen [25] and assuming the full α-particle energy was deposited.

The reduced α-decay width for ^{165}Pt is 33^{+23}_{-18} keV, and values of 90^{+23}_{-17} keV and 73^{+15}_{-12} keV were calculated for ^{166,167}Pt, respectively (shown in Figure 5.6(b)). All values were deduced from the average α-particle energies and half-lives measured in the present work and those reported by Bingham *et al.* [81]. The ^{165}Pt value appears to follow reducing decay width trends with decreasing neutron number seen in lighter elements [83]. Similar trends have been reported above the $Z = 82$ shell closure and the $N = 126$ neutron shell closure, currently thought to be a result of reducing α-particle preformation probabilities [84, 85]. This probability reduction occurs because there are fewer valence nucleons, while nuclei further away from shell closures tend to be more deformed with faster α-decays [86, 87, 88]. A hindrance factor of 2.9 can be deduced by comparing reduced α-decay widths for ^{165}Pt and its nearest even-even neighbour, ^{166}Pt. This is consistent with the α-decay of ^{165}Pt being unhindered, suggesting its ground state shares its parity and spin ($\frac{7}{2}^-$) with the ground state of ^{161}Os [71].

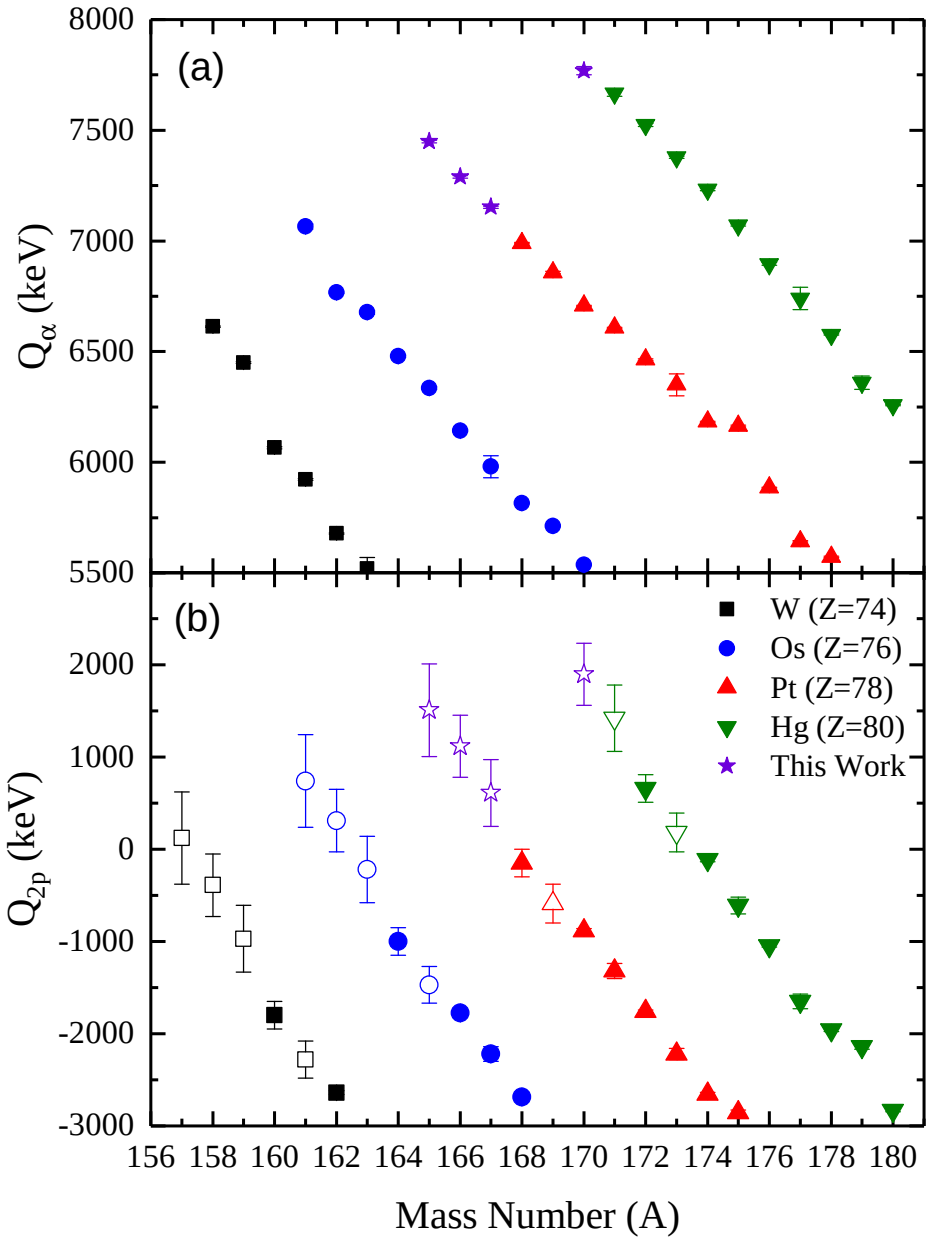

Figure 5.5: The Q values for (a) α-decay and (b) 2-proton decay plotted as a function of mass number for isotopes of W, Os, Pt, and Hg [73, 74]. Values that required a predicted mass to be used in the calculation are denoted by open symbols, whereas values that use only directly measured masses have solid markers. In (a) the error bars are smaller than the plotted symbols. Figure taken from [1].

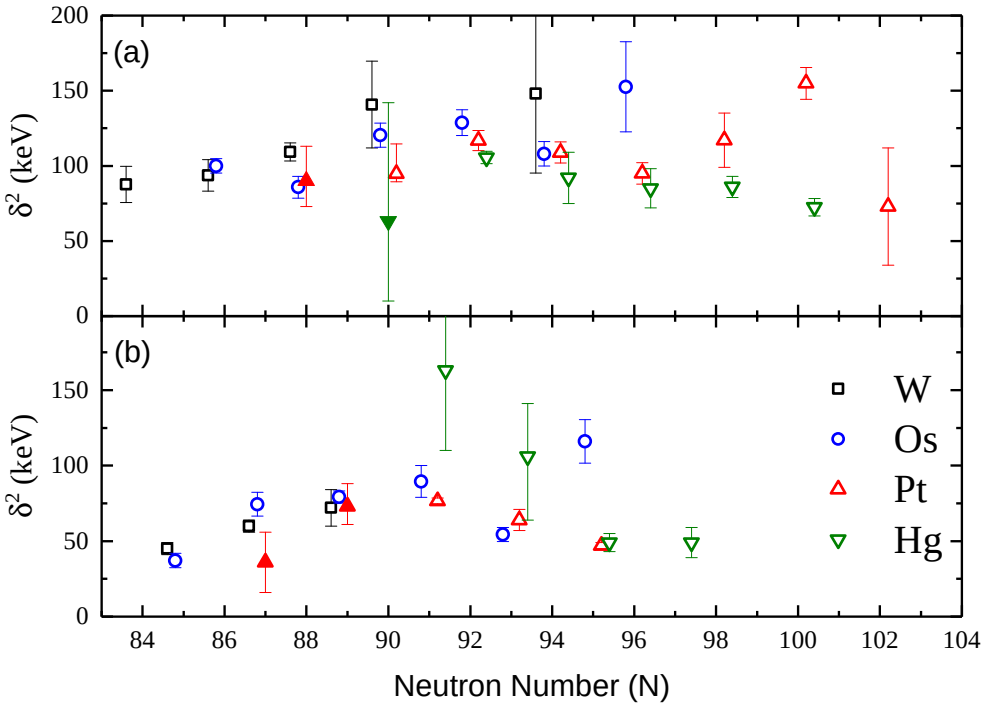

Figure 5.6: Reduced α-decay widths of W, Os, Pt, and Hg nuclei calculated using the method of Rasmussen [25]. Panel (a) shows values for even-A nuclei plotted as a function of neutron number, while panel (b) shows values for odd-A nuclei. The values for ^{170}Hg and ^{165,166,167}Pt are denoted by the solid symbols. Open symbols denote literature values, taken from [44, 45, 75, 14, 76, 77, 78, 79, 80, 81, 82]. Note that the markers on the plots are offset from one another for clarity, and not to suggest there are decimal places in neutron number. Figure taken from [1].

Chapter 6

Summary and Future Outlook

This thesis presents the key results of two experiments, each conducted using the MARA vacuum-mode recoil mass separator at the University of Jyväskylä. In the first, a 418 MeV $^{78}Kr^{15+}$ beam bombarded two targets to produce three new nuclides. Bombardment of a ^{92}Mo target produced 4 counts of new nuclide ^{165}Pt and 7 counts of new ground state $^{165}Ir^{g}$. Bombarding a ^{96}Ru target produced 16 counts of new nuclide ^{169}Au. In the second experiment, a 390 MeV $^{78}Kr^{16+}$ beam bombarded a ^{96}Ru target and produced 1 count of new nuclide ^{170}Hg. The observation of ^{169}Au marks the lightest isotope ever seen relative to its lightest stable isotope, having 28 neutrons fewer than stable ^{197}Au. The distance of known light nuclides from their lightest stable isotope is shown for elements in this region in Figure 6.1. In addition, $^{169}Au^{m}$ and $^{165}Ir^{g}$ are the shortest-lived proton emitters measured directly at a focal plane.

Measurement of ^{165}Pt and ^{170}Hg was possible by requiring subsequent same pixel decays to match known energies and half-lives of their respective characteristic decay chains, starting with ^{161}Os and ^{166}Pt, respectively. This represents the first independent confirmation of the energy and half-life of ^{161}Os. Improved measurements for the decays of ^{166,167}Pt were also presented. For ^{170}Hg an α-particle energy of E_α=7590(30) keV and half-life of $t_{1/2}=0.08^{+0.40}_{-0.04}$ ms were deduced, while for ^{165}Pt the corresponding values were 7272(14) keV and $0.24^{+0.30}_{-0.08}$ ms. Comparison of the reduced α-decay widths with systematics indicates that both α-decays are unhindered.

Both ^{170}Hg and ^{165}Pt are predicted to be unbound to the emission of 2 protons [72]. The values for their separation energies and atomic masses are not listed in the 2016 Atomic Mass Evaluation [73, 74]. It is possible to use the 2-proton separation energies of ^{161}Os and ^{166}Pt and the α-decay Q values deduced in this thesis to estimate these Q_{2p} values (shown in Figure 5.5(b)). These estimated values continue the increasing Q_{2p} value trend with decreasing mass number for given chains of isotopes. No 2-proton decay candidate events were found in the data, and it is assumed that both new nuclides still decay primarily via α-decay despite being 2-proton unbound by more than 1 MeV. Olsen *et al.* [89] predicted that, for ground state emission, 2-proton decay will compete with α-decay in ^{155}Pt and ^{159}Hg. Joss *et al.* predict that isomeric states will become proton unbound before this [90]. The proton-decay half-lives were estimated using a

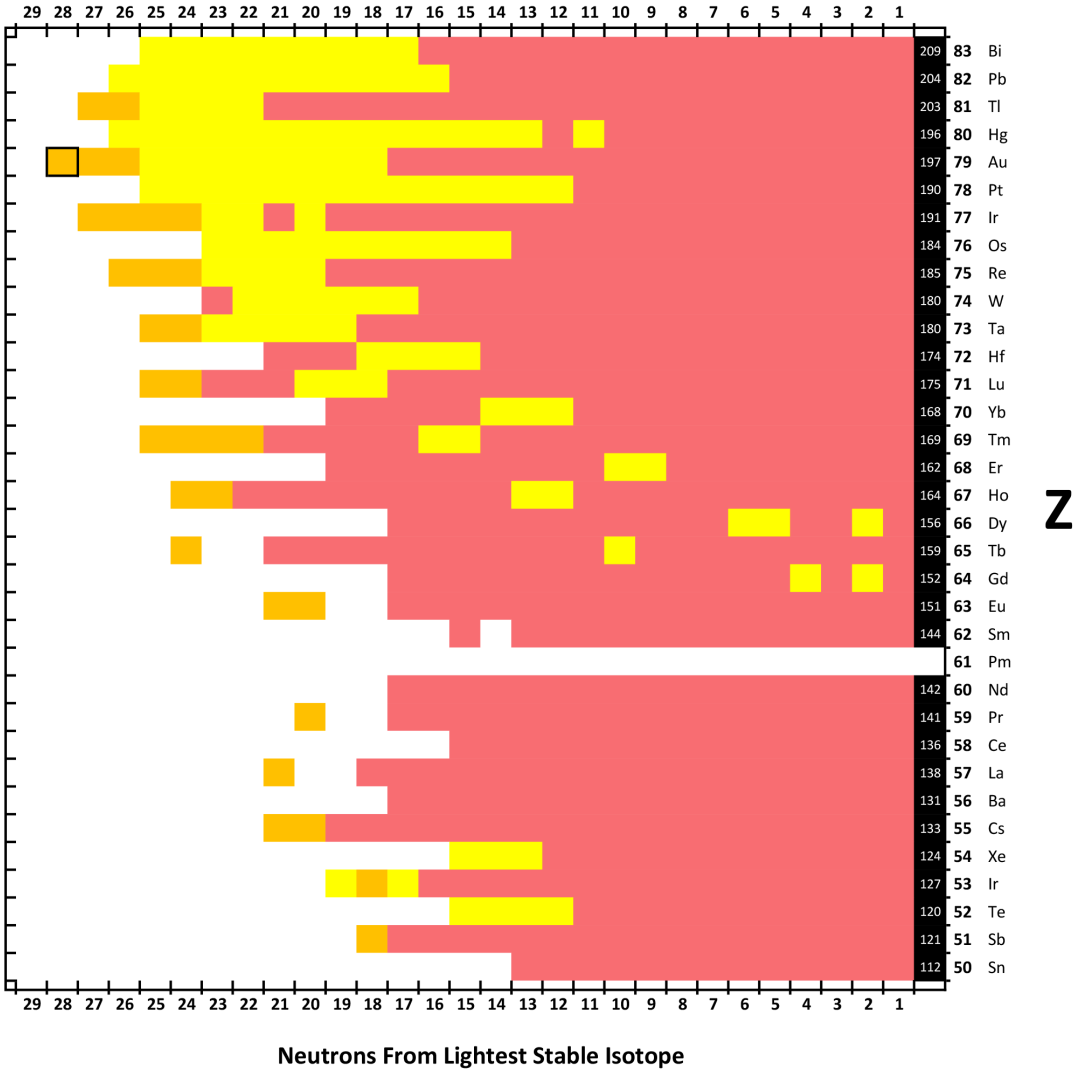

Figure 6.1: The number of neutrons a given nuclide is away from its lightest stable isotope. Colours denote primary decay mode, with burgundy indicating β^+-decay, yellow indicating α-decay and orange indicating proton decay. Black indicates α stable or naturally occurring nuclides with very long half-life.

Table 6.1: Predictions of half-lives based on extrapolated Q_α values for currently undiscovered Pt and Hg isotopes. These predictions are noted to be particularly rough, made entirely from basic linear extrapolation of the Q_α values in Figure 5.5 with no attempt made to calculate realistic hindrance factors.

Pt			Hg		
Mass (A)	Q_α (keV)	$T_{1/2}$ (μs)	Mass (A)	Q_α (keV)	$T_{1/2}$ (μs)
164	7604	47	169	7987	19
163	7748	19	168	8144	7.6
162	7893	8.2	167	8301	3.1
161	8038	3.5	166	8458	1.3
160	8183	1.6	165	8615	0.58
159	8328	0.7	164	8773	0.26

simple model which accounts for the energy and emitting spin state of the decay. The predictions are all very long. For ^{165,166,167}Pt the lower limits of the decay times are 10^{37} s, 10^{26} s and 10^{38} s. For ^{170}Hg, the lower limit is 10^{18} s. The age of the universe is 10^{17} s, so the decays are unlikely to have occurred.

Producing nuclei with observable proton emission half-lives will likely mean extremely small production cross-sections, making it unlikely these nuclei will be produced using the same experimental methods as this work. However, for the next lightest nuclides beyond ^{170}Hg and ^{165}Pt, the cross sections may not be prohibitively small. The lightest feasible isotope one could synthesise before half-lives drop below ∼1 μs, a typical recoil separator flight time, can be estimated from the smooth variation of α-decay Q values with mass number evident in Figure 5.5(a). These estimates are shown in Table 6.1, which shows predicted half-lives and Q_α values, assuming the same reduced decay width as ^{212}Po and using linear extrapolation of Q_α values (see Figure 6.2).

Based on extrapolated values from Figures 6.2 and 1.2, if the Q_α trend continues then the threshold of separator flight time compared with nuclear lifetime is likely to be crossed for the Hg isotopes somewhere around ^{166}Hg. It is noted that for ^{166}Hg, spectroscopy would have to be carried out with trace analysis similar to the proton spectroscopy in this work. ^{168}Hg is likely the fastest Hg isotope that could be studied with conventional correlation analysis.

Though no ^{164}Pt α-decay candidates were observed, $^{162-164}$Pt are likely to be sufficiently long-lived to be observed. At ^{161}Pt, the $N = 83$ nuclide, the α-decay Q value trend likely ends as its α-decay would involve breaking a closed neutron shell. It is thought that its β decay will become dominant, similar to its heaviest known isotone ^{157}W. Identifying these β decays will present additional experimental challenges.

Measurement of ^{169}Au^m and ^{165}Ir^g was possible by requiring digitised preamplifier recoil traces with decay signals superimposed on them to be followed by three or more same pixel decays. Using Python code and by requiring at least two α-decay energies to match the characteristic decay chains of each nuclide, the energies and decay times were

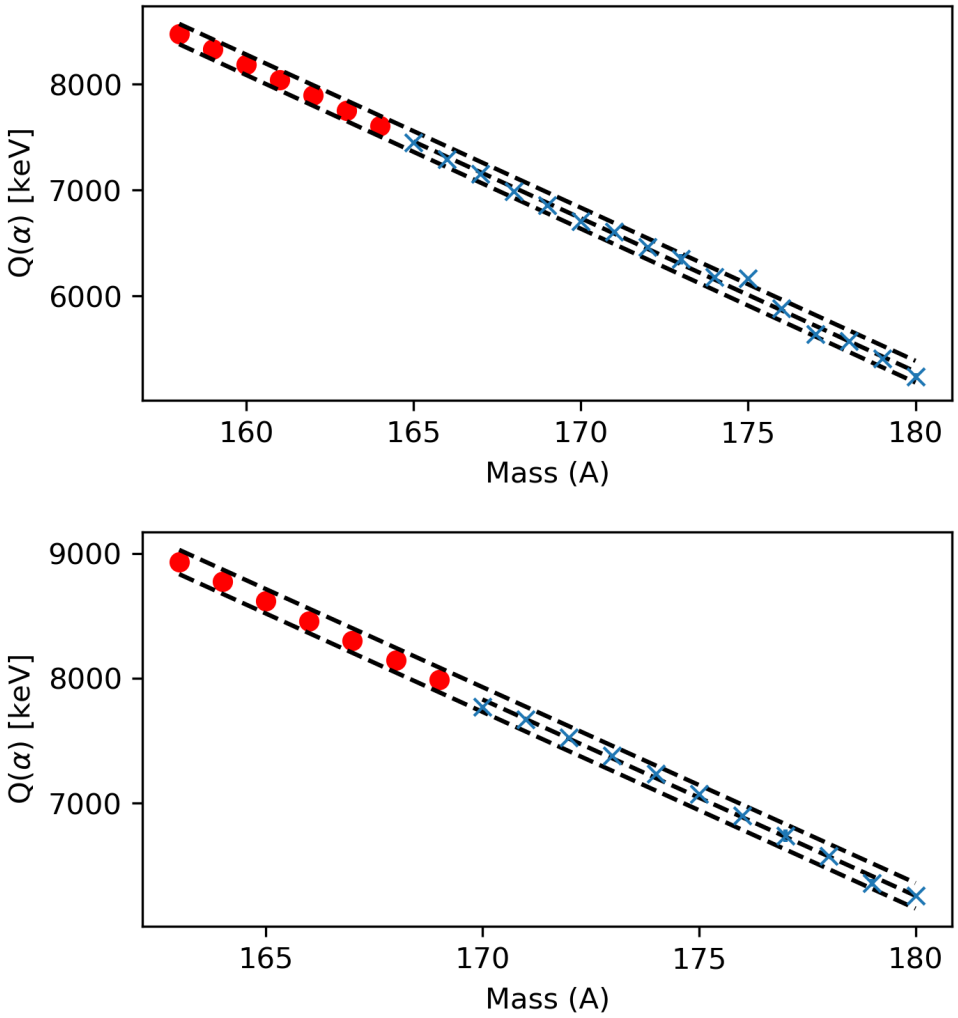

Figure 6.2: Predictions of the Q(α) values based on linear extrapolation of the current trend for (a) Pt and (b) Hg. Current data is denominated by blue crosses, predictions by red circles. The dashed lines above and below represent the uncertainty on the fit.

extracted from the traces. For ^{169}Au^{m} a proton-decay energy of E_p = 2182(28) keV and partial half-life of $t_{1/2} = 1.27^{+0.61}_{-0.57}$ µs were deduced from a total of 15 proton decays. A single α-decay was observed 1.3 µs after recoil implantation with energy E_α = 7333(27), giving a combine half-life for the state of $T_{\frac{1}{2}} = 1.16^{+0.50}_{-0.47}$ µs. For ^{165}Ir^{g} the corresponding values were E_p = 1454(38) keV and $t_{1/2} = 1.20^{+0.82}_{-0.74}$ µs from a total of 7 proton decays. These results indicate that the protons are emitted from $\pi h_{11/2}$ and $\pi s_{1/2}$ orbitals, respectively. One α-decay chain of ^{169}Au^{m} was also identified with an energy of 7333(27) keV.

Further work is needed regarding the trace collection method used in this work. The reason this work could not identify any nuclei with decay times shorter than 850 ns is the as yet unidentified artefact in every trace in this work. The small bump immediately after the full amplitude of the recoil implantation signal is reached obscures anything happening at that time. As it is not a predictable or constantly varying shape, it is challenging to find a fit that accounts for it, meaning other less precise methods were necessary. If this artefact is identified or removed, it is hoped that the minimum resolvable time can be reduced to be in line with the 150 ns minimum time see at other facilities [91, 92].

MARA performed exactly as simulated throughout both experiments, verifying its capabilities as an effective separator and proving its place on the world separator map. In order to achieve lower backgrounds, future experiments can and have employed JYUTube as a veto detector to better study Xn channels. JUROGAM III and the DPUNS charge plunger have recently been successfully commissioned at MARA, and it is also planned that SAGE (Silicon and Germanium Electron spectrometer) will be used to study electrons at the MARA target position. The addition of these detector systems enhances and expands MARAs usefulness for performing spectroscopy. There are plans to add a low energy branch to the MARA focal plane (MARA-LEB), with construction of the necessary infrastructure scheduled to start in late 2019/early 2020.

Analysis of Q-value, half-life and cross section systematics indicates that it should be possible to produce the next lightest isotope for Hg and Pt at MARA. ^{168}Hg and ^{162}Pt are likely the observable limits in any separator, as their half-lives will then likely become too short for focal plane observation. The ground states of ^{164}Ir and ^{169}Au, as well as ^{168}Au^{m}, will likely have a sub-microsecond half-lives and cross sections below 1 nb, which will make their observation challenging. Q-value systematics as well as non-observation indicate that while ^{165}Pt and ^{170}Hg are both two-proton unbound, proton decay will not compete with α-decay in these elements until a much lighter mass. Mass measurements would need to be performed for ^{152}Yb in order to connect ^{169}Au and ^{165}Ir to the mass surface via their α and proton Q-value chains. The connection of ^{165}Pt and ^{170}Hg to this mass surface will be challenging, as their decay chains contain few long-lived nuclides suitable for measurement.

The half-lives of ^{165}Ir^{g} and ^{169}Au^{m} make them the shortest-lived proton emitters measured directly at the focal plane of a recoil separator. Referring to figure 4.1 it

is clear that for each value of l there will be a different value of χ where the proton-decay half-life drops below 1 μs and experiments using the present methods become increasingly difficult. Using locally extrapolated Q values to estimate half-lives, it appears that proton emission from only $^{168}\mathrm{Au}^{m}$, $^{164}\mathrm{Ir}^{g}$ and possibly $^{163}\mathrm{Ir}^{m}$ may be observable, although these will be challenging measurements because the production cross sections are probably well below 1 nb [93, 63]. The proton decay Q-values for $h_{11/2}$ and $s_{1/2}$ states of even-N nuclei in this region are plotted in Figure 4.5. The new values from this work, plotted in red, show good agreement with existing trends, supporting the energies determined in this work.

Bibliography

[1] J. Hilton, J. Uusitalo, J. Sarén, R. D. Page, D. T. Joss, M. A. M. AlAqeel, H. Badran, A. D. Briscoe, T. Calverly, D. M. Cox et al., Phys. Rev. C **100**(1), 014305 (2019).

[2] J. Hilton, R. D. Page, J. Uusitalo, D. T. Joss, J. Sarén, M. A. M. AlAqeel, H. Badran, A. D. Briscoe, T. Calverly, D. M. Cox et al., Phys. Lett. B Submission Pending (2019).

[3] R. J. Carroll, R. D. Page, D. T. Joss, J. Uusitalo, I. G. Darby, K. Andgren, B. Cederwall, S. Eeckhaudt, T. Grahn, C. Gray-Jones et al., Phys. Rev. Lett. **112**(9), 092501 (2014).

[4] C. R. Bingham, K. S. Toth, J. C. Batchelder, D. J. Blumenthal, L. T. Brown, B. C. Busse, L. F. Conticchio, C. N. Davids, T. Davinson, D. J. Henderson et al., Phys. Rev. C **54**(1), 20–23 (1996).

[5] C. N. Davids, P. J. Woods, J. C. Batchelder, C. R. Bingham, D. J. Blumenthal, L. T. Brown, and B. C. Busse, Phys. Rev. C **55**(5), 2255–2266 (1997).

[6] R. D. Page, P. J. Woods, R. A. Cunningham, T. Davinson, N. J. Davis, A. N. James, K. Livingston, P. J. Sellin, and A. C. Shotter, Phys. Rev. C **53**(2), 660–670 (1996).

[7] M. R. Bhat, in S. M. Qaim (Editor) *Nucl. Data Sci. Technol.*, 817–821 Springer-Verlag, Berlin, Heidelberg1992.

[8] M. C. Drummond, D. O'Donnell, R. D. Page, D. T. Joss, L. Capponi, D. M. Cox, I. G. Darby, L. Donosa, F. Filmer, T. Grahn et al., Phys. Rev. C **89**(6), 64309 (2014).

[9] M. B. G. Hornillos, D. O'Donnell, J. Simpson, D. T. Joss, L. Bianco, B. Cederwall, T. Grahn, P. T. Greenlees, B. Hadinia, P. Jones et al., Phys. Rev. C **79**(6), 064314 (2009).

[10] C. Scholey, K. Andgren, L. Bianco, B. Cederwall, I. G. Darby, S. Eeckhaudt, S. Ertürk, M. B. G. Hornillos, T. Grahn, P. T. Greenlees et al., Phys. Rev. C **81**(1), 014306 (2010).

[11] H. Kettunen, T. Enqvist, T. Grahn, P. T. Greenlees, P. Jones, R. Julin, S. Juutinen, A. Keenan, P. Kuusiniemi, M. Leino et al., Phys. Rev. C **69**(5), 054323 (2004).

[12] T. Bäck, B. Cederwall, K. Lagergren, R. Wyss, A. Johnson, D. Karlgren, P. T. Greenlees, D. G. Jenkins, P. Jones, D. T. Joss et al., Eur. Phys. J. A **16**(4), 489–494 (2003).

[13] P. J. Sellin, P. J. Woods, T. Davinson, N. J. Davis, A. N. James, K. Livingston, R. D. Page, and A. C. Shotter, Zeitschrift für Phys. A **346**(4), 323–324 (1993).

[14] M. Sandzelius, E. Ganioğlu, B. Cederwall, B. Hadinia, K. Andgren, T. Bäck, T. Grahn, P. T. Greenlees, U. Jakobsson, A. Johnson et al., Phys. Rev. C **79**(6), 64315 (2009).

[15] D. Seweryniak, J. Uusitalo, M. P. Carpenter, D. Nisius, C. N. Davids, C. R. Bingham, L. T. Brown, L. F. Conticchio, D. J. Henderson, R. V. F. Janssens et al., Phys. Rev. C **60**(3), 4 (1999).

[16] D. O'Donnell, R. D. Page, C. Scholey, L. Bianco, L. Capponi, R. J. Carroll, I. G. Darby, L. Donosa, M. C. Drummond, F. Ertuğral et al., Phys. Rev. C **85**(5), 054315 (2012).

[17] B. Blank and M. J. G. Borge, Prog. Part. Nucl. Phys. **60**(2), 403–483 (2008).

[18] N. R. Sree Harsha, Eur. J. Phys. **39**(3), 035802 (2018).

[19] C. F. v. Weizsäcker, Zeitschrift für Phys. **96**(7-8), 431–458 (1935).

[20] R.-D. Herzberg, P. T. Greenlees, P. A. Butler, G. D. Jones, M. Venhart, I. G. Darby, S. Eeckhaudt, K. Eskola, T. Grahn, C. Gray-Jones et al., Nature **442**(24), 896–899 (2006).

[21] K. S. Krane and D. Halliday, *Introductory Nuclear Physics* John Wiley & Sons, Oregon State University1987.

[22] B. L. Cohen, Am. J. Phys. **36**(12), 1174 (1968).

[23] M. Goeppert-Mayer, Phys. Rev. **78**(1), 16–21 (1950).

[24] O. Haxel, J. H. D. Jensen, and H. E. Suess, Phys. Rev. **75**(11), 1766 (1949).

[25] J. O. Rasmussen, Phys. Rev. **113**(6), 1593–1598 (1959).

[26] C. Qi, F. R. Xu, R. J. Liotta, and R. Wyss, Phys. Rev. Lett. **103**(7), 072501 (2009).

[27] C. Qi, A. N. Andreyev, M. Huyse, R. J. Liotta, P. Van Duppen, and R. Wyss, Phys. Lett. B **734**, 203–206 (2014).

[28] I. Perlman and J. O. Rasmussen, in *Kernreaktionen III / Nucl. React. III*, chapter 2, 109–204 Springer, Berlin, Heidelberg, Berlin, Heidelberg1957.

[29] G. Igo, Phys. Rev. Lett. **1**(2), 72–74 (1958).

[30] F. D. Becchetti and G. W. Greenlees, Phys. Rev. **182**(4), 1190–1209 (1969).

[31] R. Bass, Nucl. Phys. A **231**(1), 45–63 (1974).

[32] J. Sarén, *The ion-optical design of the MARA recoil separator and absolute transmission measurements of the RITU gas-filled recoil separator*, Ph.d. thesis, University of Jyväskyä (2011).

[33] mesytec GmbH & Co. KG, *Mesytec MPRT-16 Technical Data* (2018).

[34] mesytec GmbH & Co. KG, *Mesytec MNV-4 Technical Data* (2018).

[35] Nutaq Scientific, *Nutaq VHS-ADC Technical Data* (2019).

[36] AMETEK Inc, *Ortec 428 Radiation Detector Bias Supply* (2015).

[37] Micron Semiconductor Ltd, *BB17 DSSD Specifications* (2019).

[38] Micron Semiconductor Ltd, *BB20 DSSD Specifications* (2019).

[39] I. H. Lazarus, D. E. Appelbe, P. A. Butler, P. J. Coleman-Smith, J. R. Cresswell, S. J. Freeman, R.-D. Herzberg, I. Hibbert, D. T. Joss, S. C. Letts et al., IEEE Trans. Nucl. Sci. **48**(3), 567–569 (2001).

[40] mesytec GmbH & Co. KG, *Mesytec MHV-4 Technical Data* (2018).

[41] Ortec Advanced Measurement Technology Inc., *Ortec Model 566 Time-to-Amplitude Converter (TAC) Operating and Service Manual* (2011).

[42] P. Rahkila, Nucl. Instruments Methods Phys. Res. A **595**(3), 637–642 (2008).

[43] P. T. Boggs and J. E. Rogers, in P. J. Brown and W. A. Fuller (Editors) *Contemp. Math.*, volume 112, 183–194 American Mathematical Society, Gaithersburg, MD 208991990.

[44] A. Rytz, At. Data Nucl. Data Tables **47**(2), 205–239 (1991).

[45] S. Hofmann, P. Armbruster, G. Berthes, T. Faestermann, A. Gillitzer, F. P. Heßberger, W. Kurcewicz, G. Münzenberg, K. Poppensieker, H. J. Schott et al., Zeitschrift für Phys. A **333**(1), 107–108 (1989).

[46] S. Hofmann, G. Münzenberg, F. P. Heßberger, W. Reisdorf, P. Armbruster, and B. Thuma, Zeitschrift für Phys. A **299**(3), 281–282 (1981).

[47] S. Hofmann, G. Münzenberg, K. Valli, F. P. Heßberger, P. Armbruster, and B. Thuma, GSI Sci. Rep. 1980 **GSI-81-2**, 204 (1980).

[48] S. Hofmann, G. Münzenberg, K. Valli, F. P. Heßberger, J. R. H. Schneider, P. Armbruster, B. Thuma, and Y. Eyal, GSI Sci. Rep. 1981 **GSI-82-1**, 241 (1981).

[49] W. N. Lennard, S. Y. Tong, G. R. Massoumi, and L. Wong, Nucl. Instruments Methods Phys. Res. B **45**(1-4), 281–284 (1990).

[50] R. Peierls, Proc. R. Soc. A **149**(868), 467–486 (1935).

[51] S. L. Meyer, in *Data Anal. Sci. Eng.* John Wiley & Sons, New York1975.

[52] K. H. Schmidt, Eur. Phys. J. A **8**(1), 141–145 (2000).

[53] A. M. Rogers, M. A. Famiano, W. G. Lynch, M. S. Wallace, F. Amorini, D. Bazin, R. J. Charity, F. Delaunay, R. T. de Souza, J. Elson et al., Phys. Rev. Lett. **106**(25), 252503 (2011).

[54] I. Mukha, L. V. Grigorenko, D. Kostyleva, L. Acosta, E. Casarejos, A. A. Ciemny, W. Dominik, J. A. Dueñas, V. Dunin, J. M. Espino et al., Phys. Rev. C **98**(6), 064308 (2018).

[55] I. Čeliković, M. Lewitowicz, R. Gernhäuser, R. Krücken, S. Nishimura, H. Sakurai, D. S. Ahn, H. Baba, B. Blank, A. Blazhev et al., Phys. Rev. Lett. **116**(16), 162501 (2016).

[56] H. Suzuki, L. Sinclair, P. A. Söderström, G. Lorusso, P. J. Davies, L. S. Ferreira, E. Maglione, R. Wadsworth, J. Wu, Z. Y. Xu et al., Phys. Rev. Lett. **119**(19), 192503 (2017).

[57] D. G. Jenkins, Phys. Rev. C **78**(1), 012801 (2008).

[58] D. S. Delion, R. J. Liotta, and R. Wyss, Phys. Rev. Lett. **96**(7), 072501 (2006).

[59] R. K. Grzywacz, M. Karny, K. P. Rykaczewski, J. C. Batchelder, C. R. Bingham, D. Fong, C. J. Gross, W. Krolas, C. Mazzocchi, A. Piechaczek et al., Eur. Phys. J. A **25**(S1), 145–147 (2005).

[60] R. D. Page, L. Bianco, I. G. Darby, J. Uusitalo, D. T. Joss, T. Grahn, R.-D. Herzberg, J. Pakarinen, J. Thomson, S. Eeckhaudt et al., Phys. Rev. C **75**(6), 061302 (2007).

[61] D. T. Joss, I. G. Darby, R. D. Page, J. Uusitalo, S. Eeckhaudt, T. Grahn, P. T. Greenlees, P. M. Jones, R. Julin, S. Juutinen et al., Phys. Lett. B **641**(1), 34–37 (2006).

[62] I. G. Darby, R. D. Page, D. T. Joss, L. Bianco, T. Grahn, D. S. Judson, J. Simpson, S. Eeckhaudt, P. T. Greenlees, P. M. Jones et al., Phys. Rev. C **83**(6), 064320 (2011).

[63] R. D. Page, Phys. Rev. C **83**(1), 014305 (2011).

[64] L. S. Ferreira, E. Maglione, and P. Ring, Phys. Lett. B **701**(4), 508–511 (2011).

[65] M. Karny, R. K. Grzywacz, J. C. Batchelder, C. R. Bingham, C. J. Gross, K. Hagino, J. H. Hamilton, Z. Janas, W. D. Kulp, J. W. McConnell et al., Phys. Rev. Lett. **90**(1), 012502 (2003).

[66] K. H. Schmidt, C.-C. Sahm, K. Pielenz, and H.-G. Clerc, Zeitschrift für Phys. A **316**(1), 19–26 (1984).

[67] I. G. Darby, R. D. Page, D. T. Joss, J. Simpson, L. Bianco, R. J. Cooper, S. Eeckhaudt, S. Ertürk, B. Gall, T. Grahn et al., Phys. Lett. B **695**(1-4), 78–81 (2011).

[68] R. J. Irvine, C. N. Davids, P. J. Woods, D. J. Blumenthal, L. T. Brown, L. F. Conticchio, T. Davinson, D. J. Henderson, J. A. Mackenzie, H. T. Penttilä et al., Phys. Rev. C **55**(4), R1621–R1624 (1997).

[69] G. L. Poli, C. N. Davids, P. J. Woods, D. Seweryniak, J. C. Batchelder, L. T. Brown, C. R. Bingham, M. P. Carpenter, L. F. Conticchio, T. Davinson et al., Phys. Rev. C **59**(6), R2979–R2983 (1999).

[70] H. Mahmud, C. N. Davids, P. J. Woods, T. Davinson, D. J. Henderson, R. J. Irvine, D. Seweryniak, and W. B. Walters, Phys. Rev. C **62**(5), 057303 (2000).

[71] L. Bianco, R. D. Page, I. G. Darby, D. T. Joss, J. Simpson, J. S. Al-Khalili, A. J. Cannon, B. Cederwall, S. Eeckhaudt, S. Ertürk et al., Phys. Lett. B **690**(1), 15–18 (2010).

[72] P. Möller, J. Nix, and K.-L. Kratz, At. Data Nucl. Data Tables **66**(2), 131–343 (1997).

[73] W. Huang, G. Audi, M. Wang, F. G. Kondev, S. Naimi, and X. Xu, Chinese Phys. C **41**(3), 030002 (2017).

[74] M. Wang, G. Audi, F. G. Kondev, W. Huang, S. Naimi, and X. Xu, Chinese Phys. C **41**(3), 030003 (2017).

[75] D. T. Joss, K. Lagergren, D. E. Appelbe, C. J. Barton, J. Simpson, B. Cederwall, B. Hadinia, R. Wyss, S. Eeckhaudt, T. Grahn et al., Phys. Rev. C **70**(1), 017302 (2004).

[76] M. Venhart, A. N. Andreyev, S. Antalic, L. Bianco, P. T. Greenlees, U. Jakobsson, P. Jones, D. T. Joss, R. Julin, S. Juutinen et al., Eur. Phys. J. A **48**(7), 101 (2012).

[77] H. Badran, C. Scholey, K. Auranen, T. Grahn, P. T. Greenlees, A. Herzan, U. Jakobsson, R. Julin, S. Juutinen, J. Konki et al., Phys. Rev. C **94**(5), 054301 (2016).

[78] K. S. Toth, C. R. Bingham, J. C. Batchelder, L. T. Brown, L. F. Conticchio, C. N. Davids, R. J. Irvine, D. Seweryniak, D. M. Moltz, W. B. Walters et al., Phys. Rev. C **60**(1), 011302 (1999).

[79] Y. Akovali, Nucl. Data Sheets **84**(1), 1–114 (1998).

[80] A. Demin, T. Fényes, I. Mahunka, V. Subbotin, and L. Trón, Nucl. Phys. A **106**(2), 337–349 (1967).

[81] C. R. Bingham, M. B. Kassim, M. Zhang, Y. A. Akovali, K. S. Toth, W. D. Hamilton, H. K. Carter, J. Kormicki, J. von Schwarzenberg, and M. M. Jarrio, Phys. Rev. C **51**(1), 125–135 (1995).

[82] A. Siivola, Nucl. Phys. **84**(2), 385–397 (1966).

[83] A. N. Andreyev, M. Huyse, P. Van Duppen, C. Qi, R. J. Liotta, S. Antalic, D. Ackermann, S. Franchoo, F. P. Heßberger, S. Hofmann et al., Phys. Rev. Lett. **110**(24), 242502 (2013).

[84] C. Xu, G. Röpke, P. Schuck, Z. Ren, Y. Funaki, H. Horiuchi, A. Tohsaki, T. Yamada, and B. Zhou, Phys. Rev. C **95**(6), 061306 (2017).

[85] C. Qi, Rev. Phys. **1**, 77–89 (2016).

[86] D. L. Hill and J. A. Wheeler, Phys. Rev. **89**(5), 1102–1145 (1983).

[87] D. S. Delion, A. Insolia, and R. J. Liotta, Phys. Rev. C **49**(6), 3024–3028 (1994).

[88] N. Severijns, A. A. Belyaev, A. L. Erzinkyan, P.-D. Eversheim, V. T. Filimonov, V. V. Golovko, G. M. Gurevich, P. Herzog, I. S. Kraev, A. A. Lukhanin et al., Phys. Rev. C **71**(4), 044324 (2005).

[89] E. Olsen, M. Pfützner, N. Birge, M. Brown, W. Nazarewicz, and A. Perhac, Phys. Rev. Lett. **110**(22), 222501 (2013).

[90] D. T. Joss, R. D. Page, A. Herzán, L. Donosa, J. Uusitalo, R. J. Carroll, I. G. Darby, K. Andgren, B. Cederwall, S. Eeckhaudt et al., Phys. Lett. B **772**, 703–707 (2017).

[91] S. N. Liddick, I. G. Darby, and R. K. Grzywacz, Nucl. Instruments Methods Phys. Res. A **669**, 70–78 (2012).

[92] S. N. Liddick, R. K. Grzywacz, C. Mazzocchi, R. D. Page, K. P. Rykaczewski, J. C. Batchelder, C. R. Bingham, I. G. Darby, G. Drafta, C. Goodin et al., Phys. Rev. Lett. **97**(8), 082501 (2006).

[93] R. D. Page, EPJ Web Conf. **123**, 01007 (2016).

Chapter 7

Appendix

7.1 Gaussian Peak Fitting Code

```
from scipy.optimize import curve_fit
from scipy.odr import Model, RealData, ODR
import csv
import numpy as np
from numpy import exp, loadtxt
import itertools
import matplotlib.pyplot as plt

#Load Data from file
PeakData = loadtxt("PeakData.csv",delimiter=',')

#Load peak guesses from file
PeakGuesses = loadtxt("PeaksGuesses.csv", delimiter=",")

#Flatten arrays for fitting
fPeakGuesses = list(itertools.chain(*PeakGuesses))


def func(x, *params):
    y = np.zeros_like(x)
    for i in range(0, len(params), 3):
        Energy = params[i]
        Counts = params[i+1]
        FWHM = params[i+2]
        sigma = FWHM/2.3548
        y = y + (Counts*exp(-(x-Energy)**2/(2*sigma**2)))
    return y

x1 = PeakData[:,0]
y1 = PeakData[:,1]

popt1, pcov1 = curve_fit(func, x1, y1, p0=fPeakGuesses)

perr1 = np.sqrt(np.diag(pcov1))
```

```
35 fit1 = func(x1, *popt1)
36
37 #Plot Fit Result
38 plt.figure(1, figsize=[10.5,7.5])
39 ax = plt.subplot(111) # Axes specified as [NUMROWS][NUMCOLS][AXISNUM]
40 ax.plot(x1, y1, 'b—')
41 ax.plot(x1, fit1 , 'r-')
42 ax.set_title("Nuclei")
43 plt.show()
44
45 gausscen = []
46 dgausscen = []
47 FWHM = []
48 k = 1
49
50 #Append LuHf fit results to calib list
51 for x in range(0,len(popt1),3):
52     gausscen.append(popt1[x])
53     dgausscen.append(perr1[x])
54     FWHM.append(popt1[x+2])
55
56 #Calib points
57 Calibcen = []
58 dCalibcen = []
59 rowcount = 0
60
61 try:
62     with open ("CalibValues.csv","r") as csvfile:
63         reader = csv.reader(csvfile, delimiter=',')
64         for row in reader:
65             Calibcen.append(int(row[0]))
66             dCalibcen.append(int(row[1]))
67         print("Calib Values loaded.")
68 except FileNotFoundError:
69     print("No Calib file found.")
70
71
72 def lin(p, x):
73     m,c = p
74     return m*x + c
75
76 def poly2(p, x):
77     a,b,c = p
78     return a*x**2 + b*x + c
79
80 linmodel = Model(lin)
81 poly2model = Model(poly2)
82
83 Calibdata = RealData(Calibcen, gausscen, sx=dCalibcen, sy=dgausscen)
84
85 odr_lin = ODR(Calibdata, linmodel, beta0=[1,0])
```

```
odr_poly2 = ODR(Calibdata, poly2model, beta0=[1,1,0])

out_lin = odr_lin.run()
out_p2 = odr_poly2.run()

x_fit = np.linspace(Calibcen[0], Calibcen[-1], 1000)
y_linfit = lin(out_lin.beta, x_fit)
y_p2fit = [out_p2.beta[0]*x**2 + out_p2.beta[1]*x + out_p2.beta[2] for x
    in x_fit]

y_chi_lin = []
y_chi_p2 = []
chi_sq_lin = []
chi_sq_p2 = []

Nuclides = loadtxt("CalibNuclides.csv",dtype=str,delimiter=',')

for x in range(0,len(Calibcen)):
    y_chi_lin.append(out_lin.beta[0]*Calibcen[x] + out_lin.beta[1])
    y_chi_p2.append(out_p2.beta[0]*Calibcen[x]**2 + out_p2.beta[1]*
    Calibcen[x] + out_p2.beta[2])

for x in range(0,len(gausscen)):
    chi_sq_lin.append(np.abs(gausscen[x]-y_chi_lin[x])/dgausscen[x])
    chi_sq_p2.append(np.abs(gausscen[x]-y_chi_p2[x])/dgausscen[x])


plt.figure(2)
plt.errorbar(Calibcen,gausscen,xerr=dCalibcen,yerr=dgausscen,fmt='rx')
plt.plot(x_fit,y_linfit,'b—')
plt.plot(x_fit,y_p2fit,'g-.')
plt.xlabel("Known Energy From Literature [keV]")
plt.ylabel("Gaussian Centroid")
plt.show()
```

7.2 Trace Drop Determining Code

```
import csv
import numpy as np
import matplotlib.pyplot as plt


filename = 'RealTraces.csv'
data = []
#######################################################################
#Open file
with open(filename, newline='') as csvfile:
    reader = csv.reader(csvfile, delimiter=',')
    for row in reader:
        data.append(row)
```

```
14
15 num_trace = len(data)
16 width = len(data[0])
17
18 data = np.zeros(((num_trace),width))
19 rownumber = 0
20 cellnumber = 0
21
22 ##########################################################################
23 #Open file
24 with open(filename, newline='') as csvfile:
25     reader = csv.reader(csvfile, delimiter=',')
26     for row in reader:
27         for element in row:
28             if element != "":
29                 try:
30                     data[rownumber][cellnumber] = float(element)
31                 except ValueError:
32                     print(element)
33             cellnumber += 1
34         rownumber += 1
35         cellnumber = 0
36     rownumber = 0
37
38 ##########################################################################
39 #Set up list for actual traces
40
41 time = [x for x in range(0,503)]
42
43 traces = data
44 for i in range(0,8):
45     traces = np.delete(traces,0,1)
46
47 ##########################################################################
48     #Reprocess traces to ln(traces)
49
50 baselines = []
51
52 for x in range(0,len(traces)):
53     baselines.append(max(traces[x]))
54
55 for x in range(0,len(traces)):
56     for y in range(0,len(traces[x])):
57         traces[x][y] = traces[x][y]-(baselines[x]+1)
58         traces[x][y] = traces[x][y]*(-1)
59
60 traces = np.log(traces)
61
62 unfittablezone = 100
63
64 #for i in range(0,(unfittablezone)):
```

```
#     traces = np.delete(traces,0,1)


realtraces = []
realnum = []
count = 0


#############################################################################
#Find where trace dips

drop_x = np.zeros((num_trace))
counter = 0

try:
    with open("DecayTimes.csv", newline='') as csvfile:
        reader = csv.reader(csvfile, delimiter=',')
        for row in reader:
            for element in row:
                drop_x[counter] = float(element)
                counter += 1
except FileNotFoundError:
    print("DecayTimes not found")
#
for x in range(0,num_trace):
    if drop_x[x] <= 0:
        for y in range(unfittablezone,490):
            if np.abs(traces[x][y] - traces[x][y+5]) >= 0.01:
                drop_x[x] = y
                break

spectratochange = []
##
#############################################################################
##Show the region of fitting

for x in range(0,num_trace):
    plt.plot(traces[x])
    plt.plot([drop_x[x]-10,drop_x[x]-10],[traces[x][int(drop_x[x])]-0.02,
    traces[x][int(drop_x[x])]+0.02],'k-', lw=2)
    plt.plot([drop_x[x]+20,drop_x[x]+20],[traces[x][int(drop_x[x])]-0.02,
    traces[x][int(drop_x[x])]+0.02],'k-', lw=2)
    plt.ylim(9,9.6)
    plt.show(block = False)
    real = input("Trace " + str(x) + ":")
    if not real:
        continue
    if real == "q":
        break
    if real == "back":
        x = x-2
```

```
114         continue
115     while True:
116         try:
117             drop_x[x] += int(real)
118             plt.plot(traces[x])
119             plt.plot([drop_x[x]-10,drop_x[x]-10],[traces[x][int(drop_x[x])
    ]-0.02,traces[x][int(drop_x[x])]+0.02],'k-', lw=2)
120             plt.plot([drop_x[x]+20,drop_x[x]+20],[traces[x][int(drop_x[x])
    ]-0.02,traces[x][int(drop_x[x])]+0.02],'k-', lw=2)
121             plt.ylim(9,9.6)
122             plt.show(block = False)
123             real = input("Trace " + str(x) + ":")
124             if not real:
125                 break
126         except ValueError:
127             print("Value not accepted")
128             break
129
130 with open("DecayTimes.csv", "w") as file:
131     for x in range(0,num_trace):
132         file.write(str(drop_x[x]))
133         if x < num_trace-1:
134            file.write(",")
135 print("DecayTimes csv Written")
136
137 ##########################################################################
138 ##Decide which should be grad fitted
139 #
140 GradOrHeight = np.zeros((num_trace))
141 counter = 0
142
143 try:
144     with open("FitChoice.csv", newline='') as csvfile:
145         reader = csv.reader(csvfile, delimiter=',')
146         for row in reader:
147             for element in row:
148                 GradOrHeight[counter] = float(element)
149                 counter += 1
150 except FileNotFoundError:
151     print("No FitChoice File found.")
152
153 subtraces = traces
154 subtime = time
155
156 for y in range(0,unfittablezone):
157     subtraces = np.delete(subtraces,0,1)
158     subtime.remove(y)
159
160
161 ##Determine trace by trace
162 for x in range(0,num_trace):
```

```
163     if GradOrHeight[x] == 0:
164         plt.plot(subtime,subtraces[x])
165         plt.plot([drop_x[x]-10,drop_x[x]-10],[subtraces[x][int(drop_x[x])-
    unfittablezone]-0.02,subtraces[x][int(drop_x[x])-unfittablezone]+0.02]
    ,'k-', lw=2)
166         plt.plot([drop_x[x]+20,drop_x[x]+20],[subtraces[x][int(drop_x[x])-
    unfittablezone]-0.02,subtraces[x][int(drop_x[x])-unfittablezone]+0.02]
    ,'k-', lw=2)
167         plt.show(block = False)
168         real = input("Trace " + str(x) + ":")
169         if not real:
170             continue
171         if real == "q":
172             break
173         if real == "g":
174             GradOrHeight[x] = 1
175         if real == "h":
176             GradOrHeight[x] = 2
177
178 #Save results of efforts
179 with open("FitChoice.csv", "w") as file:
180     for x in range(0,num_trace):
181         file.write(str(GradOrHeight[x]))
182         if x < num_trace-1:
183            file.write(",")
184 print("FitChoice csv Written")
185
186 ##########################################################################
187 ###Methods found, calculate heights
188 #
189 m1 = np.zeros((num_trace))
190 c1 = np.zeros((num_trace))
191 m2 = np.zeros((num_trace))
192 c2 = np.zeros((num_trace))
193 mf = np.zeros((num_trace))
194 cf = np.zeros(((num_trace),8))
195 xsubset1 = []
196 xsubset2 = []
197 ysubset1 = []
198 ysubset2 = []
199
200 height = np.zeros(((num_trace),8))
201
202
203 altgraddrop = np.zeros(((num_trace),8))
204
205 subdropx = drop_x
206 subdropx = subdropx - unfittablezone
207
208 for x in range(0,num_trace):
209     if GradOrHeight[x] == 1:
```

```
210         for y in range(0,int(subdropx[x]-10)):
211             xsubset1.append(subtime[y])
212             ysubset1.append(subtraces[x][y])
213         m1[x], c1[x] = np.polyfit(xsubset1,ysubset1,1)
214         for y in range(int(subdropx[x]+10),len(subtime)-1):
215             xsubset2.append(subtime[y])
216             ysubset2.append(subtraces[x][y])
217         m2[x], c2[x] = np.polyfit(xsubset2,ysubset2,1)
218 
219         #Standard method - forced gradient match
220         if len(xsubset1) > len(xsubset2):
221             mf[x] = m1[x]
222             cf[x][0] = c1[x]
223             cf[x][1] = np.mean(ysubset2) - (mf[x]*np.mean(xsubset2))
224             cf[x][3] = mf[x] * drop_x[x] + cf[x][0]
225             cf[x][4] = mf[x] * drop_x[x] + cf[x][1]
226             cf[x][2] = abs(cf[x][3] - cf[x][4])
227             cf[x][5] = ((np.exp(cf[x][3]))*-1)+(baselines[x]+1)
228             cf[x][6] = ((np.exp(cf[x][4]))*-1)+(baselines[x]+1)
229             cf[x][7] = abs(cf[x][5] - cf[x][6])
230 
231         if len(xsubset1) < len(xsubset2):
232             mf[x] = m2[x]
233             cf[x][0] = c2[x]
234             cf[x][1] = np.mean(ysubset1) - (mf[x]*np.mean(xsubset1))
235             cf[x][3] = mf[x] * drop_x[x] + cf[x][0]
236             cf[x][4] = mf[x] * drop_x[x] + cf[x][1]
237             cf[x][2] = abs(cf[x][3] - cf[x][4])
238             cf[x][5] = ((np.exp(cf[x][3]))*-1)+(baselines[x]+1)
239             cf[x][6] = ((np.exp(cf[x][4]))*-1)+(baselines[x]+1)
240             cf[x][7] = abs(cf[x][5] - cf[x][6])
241 
242 
243         #New method, free fit and check difference at drop_x
244         altgraddrop[x][0] = m1[x] * drop_x[x] + c1[x]
245         altgraddrop[x][1] = m2[x] * drop_x[x] + c2[x]
246         altgraddrop[x][2] = np.abs(altgraddrop[x][0]-altgraddrop[x][1])
247         altgraddrop[x][3] = ((np.exp(altgraddrop[x][0]))*-1)+(baselines[x
    ]+1)
248         altgraddrop[x][4] = ((np.exp(altgraddrop[x][1]))*-1)+(baselines[x
    ]+1)
249         altgraddrop[x][5] = np.abs(altgraddrop[x][3]-altgraddrop[x][4])
250 
251         xsubset1.clear()
252         xsubset2.clear()
253         ysubset1.clear()
254         ysubset2.clear()
255     if GradOrHeight[x] == 2:
256         maximum = 0
257         minimum = 14000
258         for y in range(int(drop_x[x])-5,int(drop_x[x])+20):
```

```
259             try:
260                 if traces[x][y] > maximum:
261                     maximum = traces[x][y]
262                 if traces[x][y] < minimum:
263                     minimum = traces[x][y]
264             except IndexError:
265                 continue
266         height[x][0] = maximum
267         height[x][1] = minimum
268         height[x][2] = abs(height[x][0]-height[x][1])
269         height[x][3] = ((np.exp(maximum))*-1)+(baselines[x]+1)
270         height[x][4] = ((np.exp(minimum))*-1)+(baselines[x]+1)
271         height[x][5] = abs(height[x][3]-height[x][4])
272
273 ######################################################################
274
275 y_trace = []
276 resetwidth = 50
277 width = resetwidth
278
279 original = []
280 alternative = []
281 manual = []
282
283 for a in range(0,num_trace):
284     if a not in original and a not in alternative and a not in manual:
285         if drop_x[a] + width >= 500:
286             width = 500 - int(drop_x[a])
287     #     if drop_x[a] - width < 90:
288     #         width = int(drop_x[a]) - 90
289         if GradOrHeight[a] == 1:
290             x = np.linspace(int(drop_x[a])-width,int(drop_x[a])+width,(2*
    width+1))
291     #         print(x)
292             y_alt = m1[a] * x + c1[a]
293             y = mf[a] * x + cf[a][0]
294             for i in range(int(min(x)),int(max(x))+1):
295                 y_trace.append(traces[a][i])
296             plt.figure(a, figsize=[8,5.5])
297     #         plt.plot(subtime, subtraces[a])
298             plt.plot(x, y_trace)
299             plt.plot(x,y, '-r', label='Before')
300             plt.plot(x,y_alt, '-b', label='Before')
301             y_alt = m2[a] * x + c2[a]
302             y = mf[a] * x + cf[a][1]
303             plt.plot(x,y, '-r', label='After')
304             plt.plot(x,y_alt, '-b', label='After')
305             plt.plot([int(drop_x[a]),int(drop_x[a])],[int(m1[a] * drop_x[a
    ] + c1[a]),int(m2[a] * drop_x[a] + c2[a])], '-g')
306             plt.ylim(traces[a][int(drop_x[a])]-0.05,traces[a][int(drop_x[a
    ]+10)]+0.05)
```

```
307             plt.title("Trace: " + str(a) + " Drop difference = %.3f" % np.
    abs(cf[a][2] - altgraddrop[a][2]) + " Drops: %.3f" % cf[a][2] + " %.3f
    " % altgraddrop[a][2])
308             plt.show(block = False)
309             real = input("Trace " + str(a) + ":")
310             if real == "m":
311                 manual.append(a)
312             if real == "o":
313                 original.append(a)
314             if real == "a":
315                 alternative.append(a)
316             if real == "q":
317                 break
318         if GradOrHeight[a] == 2:
319             x = np.linspace(int(drop_x[a])-width,int(drop_x[a])+width,(2*
    width+1))
320             for i in range(int(min(x)),int(max(x))+1):
321                 y_trace.append(traces[a][i])
322             plt.figure(a, figsize=[8,5.5])
323             plt.plot(x, y_trace)
324 #           plt.plot(traces[a])
325             plt.plot([int(drop_x[a])-20,int(drop_x[a])+20],[height[a][0],
    height[a][0]], '-r')
326             plt.plot([int(drop_x[a])-20,int(drop_x[a])+20],[height[a][1],
    height[a][1]], '-r')
327             plt.title("Trace: " + str(a) + " Drop: %.f" % height[a][2])
328             plt.show(block = False)
329             real = input("Trace " + str(a) + ":")
330             if real == "m":
331                 manual.append(a)
332             if real == "o":
333                 original.append(a)
334             if real == "a":
335                 alternative.append(a)
336             if real == "q":
337                 break
338         y_trace.clear()
339         width = resetwidth
340 ##
341 final = np.zeros(((num_trace),8))
342 altfinal = np.zeros(((num_trace),8))
343 filterfinal = np.zeros(((num_trace),10))
344
345 for x in range(0,num_trace):
346     for y in range(0,7):
347         final[x][y] = data[x][y]
348         altfinal[x][y] = data[x][y]
349         filterfinal[x][y] = data[x][y]
350     if GradOrHeight[x] == 1:
351         final[x][7] = cf[x][2]
352         altfinal[x][7] = altgraddrop[x][2]
```

```
353         if x in original:
354             filterfinal[x][7] = cf[x][7]
355             filterfinal[x][8] = cf[x][5]
356             filterfinal[x][9] = cf[x][6]
357         if x in alternative:
358             filterfinal[x][7] = altgraddrop[x][5]
359             filterfinal[x][8] = altgraddrop[x][3]
360             filterfinal[x][9] = altgraddrop[x][4]
361         if x in manual:
362             filterfinal[x][7] = 0
363     if GradOrHeight[x] == 2:
364         final[x][7] = height[x][2]
365         altfinal[x][7] = height[x][2]
366         if x in alternative or x in original:
367             filterfinal[x][7] = height[x][5]
368             filterfinal[x][8] = height[x][3]
369             filterfinal[x][9] = height[x][4]
370         if x in manual:
371             filterfinal[x][7] = 0
372
373 ##Save results of efforts
374 #
375 with open("TraceDrops.csv", "w") as file:
376     for x in range(0,num_trace):
377         for y in range(0,10):
378             file.write(str(filterfinal[x][y]))
379             if y < 9:
380                 file.write(",")
381         if x < num_trace - 1:
382             file.write("\n")
383 print("TraceDrops csv Written")
```